Dynamics and synchronization in biological excitable media

Jinshan Xu

THÈSE

en vue d'obtenir le grade de

Docteur de l'École Normale Supérieure de Lyon - Université de Lyon

Discipline : Physique

LABORATOIRE DE PHYSIQUE

École Doctorale de Physique et Astrophysique de Lyon

présentée et soutenue publiquement le 03/12/2012

par Monsieur **Jinshan XU**

Dynamics and synchronization in biological excitable media

Directeur de thèse:	Monsieur Alain Pumir
Co-directeur de thèse:	Monsieur Nicolas GARNIER
	Monsieur Zonghua LIU
Après l'avis de:	Monsieur Cyril RAUCH
	Monsieur Sasha PANFILOV

Devant la commission d'examen formée de :

Madame Martine BENAMAR, Membre
Monsieur Nicolas GARNIER, Membre
Monsieur Zonghua LIU, Membre
Monsieur Sasha PANFILOV, Rapporteur
Monsieur Alain PUMIR, Membre
Monsieur Cyril RAUCH, Rapporteur
Monsieur Sitabhra SINHA, Membre

Abstract

This thesis investigates the origin of spontaneous activity in the uterus. This organ does not show any activity until shortly before delivery, where very fast and efficient contractions are generated. The aim of this work is to provide insight into the origin of spontaneous oscillations and also on the transition from asynchronous to synchronized activity in the pregnant uterus.

One intriguing aspect in the uterus is the absence of any pacemaker cell. The organ is composed of muscular cells, which are excitable, and connective tissue with cells whose behavior is purely passive. None of these cells, taken in isolation, spontaneously oscillates. We develop an hypothesis based on the observed strong increase in the electrical coupling between cells in the last days of pregnancy. The study is based on a mathematical model of (muscular) excitable cells, coupled to each other on a regular lattice, and to a fluctuating number of passive cells, consistent with the known structure of the uterus. The two parameters of the model, the coupling between excitable cells, and between excitable and passive cells, grow during pregnancy.

Using both a model based on measured electrophysiological properties, and a generic model of excitable cells, we demonstrate that oscillations can appear spontaneously when increasing the coupling coefficients, ultimately leading to coherent oscillations over the entire tissue. We study the transition towards a coherent regime, both numerically and semi-analytically, using the simple model of excitable cells. Last, we demonstrate that, the realistic model reproduces irregular action propagation patterns as well as the bursting behavior observed in the *in-vitro* experiments.

Keywords: uterine myocyte model, excitable media, gap junction coupling, synchronization, uterine contraction

Résumé

Cette thèse étudie l'origine de l'activité spontanée dans l'utérus. Cet organe n'a aucune activité jusquà la délivrance, où les contractions rapides et efficaces sont générés. Le but de ce travail est de fournir un aperçu de l'origine des oscillations spontanés et de la transition de l'activité asynchrone à synchronisé dans l'utérus gravide.

Un aspect intéressant de l'utérus est l'absence de pacemaker. L'organe est composé de cellules musculaires, qui sont excitables, et conjonctives, dont le comportement est purement passif, aucune de ces cellules, pris isolément, oscillent spontanément. Nous développons une hypothèse basée sur l'augmentation grande du couplage électrique entre les cellules observée pendant la grossesse. L'étude est basée sur deux modèles des cellules excitables, couplé à l'autre sur un réseau régulier, et un nombre variable de cellules passives, en accord avec la structure connue de l'utérus. Les deux paramétres du modèle, le couplage entre les cellules excitables, et entre les cellules excitables et passive, croissent pendant la grossesse.

En utilisant les deux modèles, nous démontrons que les oscillations peuvent apparaitre spontanément lorsque l'on augmente les coefficients de couplage, conduisant finalement à des oscillations cohérentes sur l'ensemble du tissu. Nous étudions la transition vers un régime cohérent, à la fois numériquement et semi-analytique, en utilisant le modàle simple des cellules excitables. Enfin, nous montrons que le modèle réaliste reproduit irréguliers modes de la propagation d'action potentiels ainsi que le comportement de bursting, observé dans les expériences in vitro.

Mots-clefs: modèle myocyte utérin, milieux excitable, couplage du jonction gap, synchronisation, contraction utérine

Acknowledgements

After having completed this work, I look back to my life three years ago. I feel that I'm the luckiest man in the world. Around me, there are so many people helping me. At this moment, I feel it is appropriate to express how I appreciate the help you gave during these years. Without you, no single achievement could be made.

First and foremost, I would like to express my gratitude to one of my thesis advisor, Monsieur Nicolas GARNIER. It is him who helped me to achieve my dream of having a doctor degree; It is him who gave me the chance to come to France; It is also him who with great patience answered my numerous, 'stupid' questions. He is strict specially to students not bright like me. But this doesn't stop him taking care of me, especially when I first arrived in Lyon.

I am very grateful to Monsieur Alain PUMIR, my research director, for his guidance, support and help at ENS–Lyon. His excellent and enthusiastic supervision together with his patience and encouragement is indispensable in accomplishing this thesis. I could not have imagined of having a better supervisor.

I feel lucky also because I have a third very nice supervisor, Professor Zonghua Liu, at East China Normal University. I have valued working with him and his group in Shanghai. The discussions with them helped a lot in writing the thesis.

I would like to thanks Professor Sasha Panfilov from Gent University and Cyril Rauch from University of Nottingham for their careful reading. Their suggestions and remarks have largely improved this manuscript.

My thanks also go to the Laboratoire de Physique (UM 5672), who provides wonderful learning and working environment, and whose members are so nice not

only providing scientific suggestions but also helping me exploring the wonderful life in France. Special thanks to Ludovic Bellon, Robert Zimmermann, Delphine Chareyron, Michel Vosskuhle, Lionel Fiabane and other friends in the lab.

Financial support is gratefully acknowledged from the China Scholarship Council, Coopérations et mobilités internationales Rhone-Alpes and Laboratoire de Physique.

Finally, I would like to thank my parents for their understanding and love. I would like also to thank my wife for her understanding and support.

Table of Contents

Chapter 1

Introduction

1.1 Rhythmic activities in biology

Oscillations are ubiquitous in biology [1]. Many biological processes in living systems are performed in the form of oscillations with periods spanning more than ten orders of magnitude, ranging from a fraction of a second in neurons up to tens of years in ecology [1, 2, 3]. Rhythmic activities are of special importance to living animals. Lacking of normal rhythmic activities or disruption of the rhythmic processes beyond the normal bounds is usually related to diseases. The jet lag, a loss of normal circadian rhythm caused by jet travel across multiple time zones, usually causes daytime sleepiness, decreased alertness, loss of concentration, impaired performance, fatigue, irritability, disorientation, depressed mood and gastrointestinal disturbance [4]. Disruptions of cardiac rhythmic contractions lead to a sharp decrease of the pressure that pumps blood throughout the body. This is the leading cause of death, at least in the industrialized world.

Because of potential clinical applications, the investigation of the origin and dynamics of the rhythmic activities has attracted research efforts not only from physicians and experimental physiologists, but also from mathematicians and physicists. Experimentalists have revealed that most of the spontaneous oscillations in living animals are initiated by special agencies, capable of generating spontaneous oscillations. For example, the rhythmic contractions of our heart is triggered by the sinoatrial node [5]; the animal locomotion is controlled by a central pattern generator, which is an intraspinal network of neurons capable of generating a rhythmic output [6]; the circadian rhythm is controlled by suprachiasmatic nucleus (SCN neurons) [7], etc. Mathematical results show that nonlinear equations are capable of describing the physiological systems. After the milestone work of Hodgkin and Huxley [8], models that capture qualitatively and even in some cases very quantitatively complex physiological processes have been proposed. In the case of cardiac electrophysiology, models capture with an ever increasing accuracy the electric phenomena occurring in the heart [9, 10, 11, 12, 13]. These computational descriptions have considerably improved our understanding of the mechanisms of cardiac arrhythmias, and may even

lead to progress in developing treatments [14].

Rhythms in many organs is in fact imposed by a group of specialized cells, also known as pacemakers, which generate action potentials spontaneously. In the heart, the main pacemaker is the Sino-Atrial node, which consists of spontaneously oscillating cells. In smooth muscles, the Interstitial cell of Cajal have been shown to play the role of pacemakers. Example include the ureter [15, 16] or the bladder [17].

Among the tissues that spontaneously oscillate, due to the presence of specialized pacemaker regions, the uterus seem to have a different status: so far, the cells that constitute the uterus have not been found to oscillate spontaneously, when taken in isolation. Yet, the organ does produce very strong contractions during the late stage of pregnancy, leading to the expulsion of the new-born !

1.2 Towards understanding uterine contractions

The uterus is a unique organ. Although it stays quiescent most of the time, it generates forceful contractions necessary for the expulsion of the mature fetus at term. Like in the heart and other smooth muscle assembles, the contractions are triggered by electrical activity in the form of action potentials [20, 21, 22]. As illustrated in Fig.1.1, the duration and the frequency of action potentials determine the amplitude and the strength of the contractile force in smooth muscle cells [23]. However, the precise mechanism responsible for the transition from a quiescent uterus during most of the

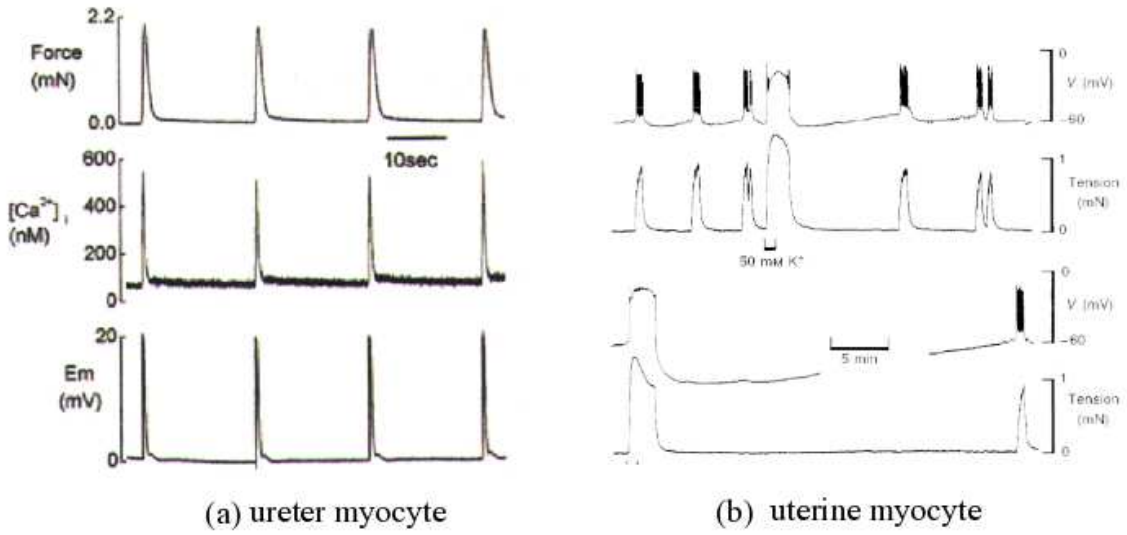

Figure 1.1: The relationship between force and membrane potential in ureter smooth muscle. (a) Simultaneous recording of force (top), $[Ca^{2+}]_i$ (middle) and membrane potentials Em (bottom) in strips (5mm in length) of guinea-pig ureter [18]. (b) Simultaneous recording of force and membrane potentials in a human uterine myocyte [19].

pregnancy, to a rhythmically contracting muscle at the onset of labour remains to be fully understood. A good understanding of this issue has potentially a very significant clinical impact. In fact, as shown in Fig. 1.2, preterm contractions occur in about 10% of all pregnancies [24] and had a tendency to increase during the last two decades. This in turn is the cause of approximately a third of all infant deaths in the USA [25]. And the surviving premature infants are more likely to suffer from neurological disabilities, whose cost has been estimated in the US to $26 billions each year [26]. In this context, the lack of a precise understanding of the mechanism of contractions of the uterine tissue is a serious impediment to the development of appropriate treatments.

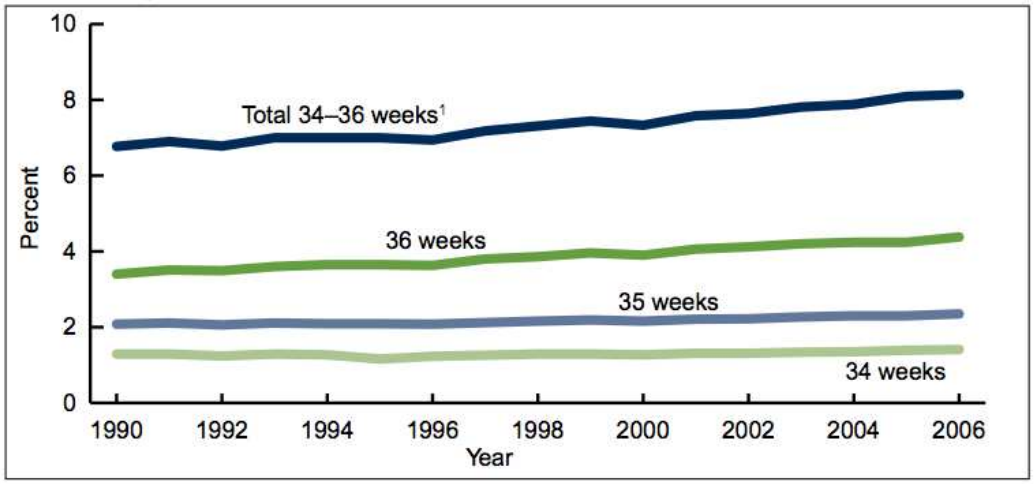

Figure 1.2: Birth rates at 34, 35, 36, and total 34 to 36 weeks of gestation: United States, 1990–2006. Figure replotted from Ref. [24]

1.2.1 Absence of pacemaker cells in uterus

So far, the efforts aimed at understanding the origin of uterine contractions have remained inconclusive. Despite several attempts, cells with an unambiguous pacemaker role have not been found in the uterus [27, 28]. The Interstitial Cajal like cells (ICLCs) closely related to the Interstitial Cajal cells acting as pacemaker in other smooth muscle, such as the rabbit urethra [29, 16], have been thought to play the role of pacemaker cells in uterine tissue. However, in the uterine tissue, ICLCs have been proven to be electrically passive, and has even been argued to actually inhibit electrical activity [30, 16]. It has therefore been suggested that the spontaneous electrical behavior exhibited in the uterus is an inherent property of the smooth-muscle cells within the myometrium [23]. Young *et al.* however pointed out that the myocyte alone can not be responsible for generation of contraction forces and passage of action potential [31], suggesting that some other aspects should been examined.

The observation that uterine contractions propagate generally from the fundus toward the cervix during active labor [32], which facilitate the expulsion of the fetus,

suggests that although there may not be a specific type of individual pacemaker cell, there may be general pacemaker regions later in gestation [23]. This prompts the detailed investigation of the eletrophysiological changes occurring throughout pregnancy.

1.2.2 Uterine electrophysiological changes during pregnancy

Important hint concerning the cause of the spontaneous oscillations have been provided by the thorough investigations of the physiological changes occurring in uterine tissue throughout pregnancy, resulting in modification of the electric activity [20], in particular shortly before delivery. In fact, several important physiological changes have been reported. The first obvious set of changes occurring during pregnancy concern merely the morphological aspects of the uterus. The tissue has to enlarge to accommodate the growing fetus, resulting in an enlargement from $70g$ to $1750g$ in humans [31]. This is accompanied by the growth of single cell surface area by a factor approximately 4 [33]. Consistent with the observed hypertrophy of the uterus, the cell capacitance increases as the pregnancy progresses. In rat uterus, the membrane capacitance C_m has been observed to increase by a factor 4 during the course of the pregnancy [33].

Electrophysiological recordings have shown changes, both for the outward (potassium) and for the inward (Sodium, Calcium) transmembrane currents [33, 34]. *In-vitro* experiments on rat uterus show that the maximum value of the current through sodium channels increases by a factor slightly less than 2: the recorded peak sodium current for non-pregnant uterine myocytes is about $2.8\mu\text{A/cm}^2$ and grows to about $5.1\mu\text{A/cm}^2$ for late-pregnant myocytes [33]. Similarly, important changes are also observed for Calcium channel: the peak Calcium current decreases from approximately $5.7\mu\text{A/cm}^2$ for non-pregnant to about $3.4\mu\text{A/cm}^2$ for late-pregnant myocytes [33]. Significant changes in the myocyte resting potential have also been observed, which increases from a value close to -70 mV at the beginning of pregnancy, to -55 mV at middterm [35].

However, none of the above mentioned changes in the electrophysiological properties of the myocytes is sufficient to lead to a spontaneous electrical activity. For this reason, it has been suggested that the primary control of the electrical activity of the uterus may not be due to the myocytes themselves [31].

In comparison to the electrophysiological changes reported during pregnancy, the increase in the expression of gap junctions during late pregnancy turns out to be even more dramatic. The fractional area of gap junctions, defined as the ratio of the membrane area occupied by gap junctions and the total membrane area, has been observed to increase by a large factor, up to 20-fold, from 0.01 to 0.23 in the rat uterus [36]. Further, increase of gap junctional conductance from 4.7nS at normal preterm to 32 nS during delivery has been observed [37].

It is believed that the dramatic formation of gap junction is closely related to the secretion of hormones [38]. The **progesterone**, secreted from the corpus luteum in

the ovary, inhibits the uterine contractions at early pregnancy. Toward the end of pregnancy, the sharp increase of secretion of **estrogen** from the placenta overcomes the effect of **progesterone**, and causes uterine muscle fibers to form gap junctions with one another. This process is now thought to be related to the secretion of **corticotropin-releasing hormone (CRH)**, a clock that establishes to timing of birth. Women who have higher levels of CRH earlier in pregnancy are more likely to deliver prematurely [38].

1.2.3 Modeling uterine activities

Modeling approach has shown its power in improving our understanding of neural science and the mechanism of cardiac diseases. In trying to understand how the uterus is functioning, it has been proposed that detailed mathematical models, aimed at predicting the experimentally observed phenomena, need to developed [39]. In the absence of enough experimental information at the cellular level, several attempts have been made to model uterine contractions using a more global point of view. This approach had proven to be very fruitful in the heart [40]. In 1995, Andersen *et al.* modeled the uterine contraction waveforms, by assuming each uterine cell is a contractile element and there are pacemaker cells initiating the rhythmic activities [41]. Two years later, Young *et al.* improved this model by considering a double-signaling mechanism, the action potential propagation and the intercellular calcium waves [32]. These early contributions postulated the presence of pacemaker cells, as well as contractile elements in the uterus. These assumptions have never been verified experimentally, which has been a very serious impediment in efforts to model the uterus contractions in the 1990s.

In the spirit of the description of Hodgkin-Huxley giant axon model, it is customary to develop models, based on the properties of single cells, which can be inferred by integrating biophysical information from experimental facts. Important results concerning the electrophysiology of uterine myocyte were obtained in the 1990s; the results of references [33, 34, 42] still provide important information to build a model of uterine myocytes. In 2009, a realistic model that incorporates the main ion currents based on experimental findings was proposed by Rihana *et al.* [43]. In 2011, with the help of more accurate experimental data, Tong *et al.* developed a model which reproduces very well the recorded uterine electrical activity [44]. The applications of electromyography (EMG) [45] and magnetomyography (MMG) [46] enable the spontaneous recording of the electrical and mechanical activities, and has revealed the relations between action potentials and the contractile force [23]. Based on this information, a model describing the relation between action potential and the mechanical force has been proposed [47]. This very significant progress has not provided an answer to the question concerning the origin of the electrical activity in the uterus observed before delivery.

1.3 Anatomical description of uterus

The human uterus is a single, hollow, pear-shaped organ with a thick muscular wall; it lies in the pelvic cavity between the bladder and rectum. The nonpregnant uterus varies in size depending on the individual but generally is about 7 cm in length, 3 to 5 cm at its widest (upper) part, and 2.5 to 3.0 cm thick, but it enlarges by a factor of four or five during pregnancy [48]. This enables the uterus to receive the fertilized ovum and to provide accommodation for its development until birth.

The uterine wall is composed of three distinct layers in most species: an inner layer, the endometrium, that lines the lumen of the organ, an intermediate layer, the myometrium, and an external layer, the perimetrium. The perimetrium is the serosal or peritoneal layer that covers the body of the uterus and supravaginal part of the cervix posteriorly and the body of the uterus anteriorly. The myometrium is the contractile elements of the uterus. It is believed the expulsive efforts of the term-pregnant human uterus are the result of coordinated contractions of the 100

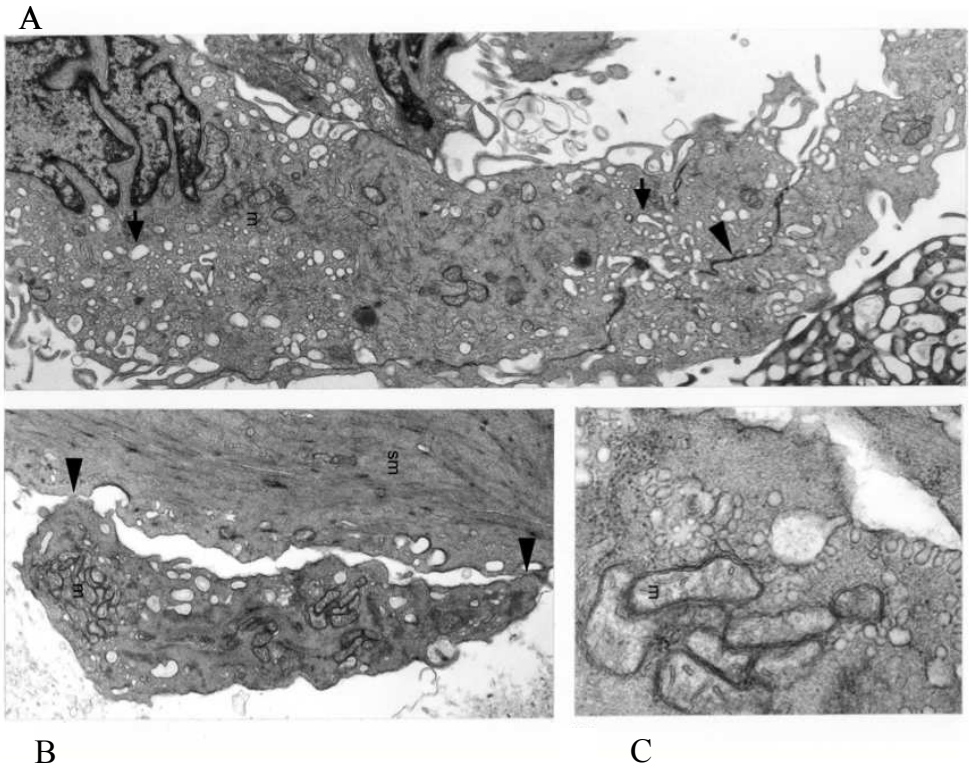

Figure 1.3: Electronmicrographs of human myometrium. Smooth muscle cells are lebaled as *sm*. Long slender ICLC contains numerous mitochondria (*m* in A) and makes close contact with a smooth-muscle cell (arrow heads in B). Original magnification A: × 11200; B: ×12 000; and C: × 48000 . Extracted from [27]

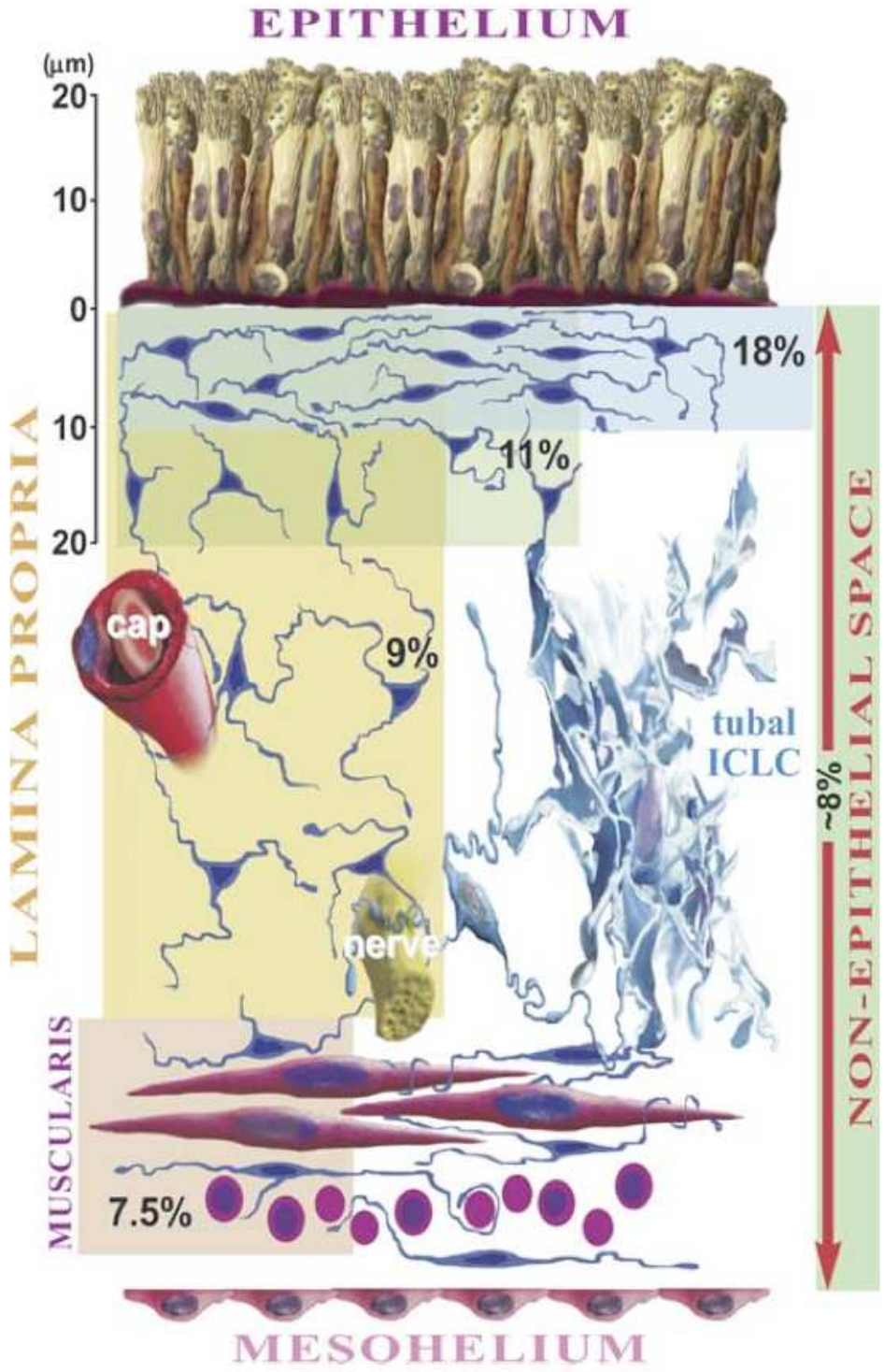

Figure 1.4: Schematic drawing of the Distribution of ICLCs in the human uterus wall. Relative ICLCs density: $\sim 18\%$ immediately under the epithelium, $\sim 9\%$ in the lamina propria thickness, and $\sim 7.5\%$ in the musculaires. Replotted from Ref. [30].

billion smooth muscle cells (myocyte) in the myometrium [49]. Microanatomical investigation reveals four distinct structural elements: cylindric, sheet-like, fiber, and communicating bundles [49]. These structures merge with each other and potentially form an interlacing network, connecting the vast majority of the myocytes of the uterus in a contiguous pathway.

The myometrium is inhomogeneous, consisting of bundles of smooth muscle cells separated by thin strands of connective tissue that contain fibroblasts, Interstitial Cajal-Like Cells (ICLCs) etc., as illustrated in Fig.1.3. The muscle cells (uterine myocytes) compose the majority of the uterus wall. These cells are generally long, spindle shaped, with a length of 30 to 50 μm in a non-pregnant uterus, but during pregnancy, they hypertrophy to reach lengths of 500 to 600 μm or greater [33]. The increase in size goes together with an increase of membrane capacitance from 25pF to 120 pF. Among the connective cells, the ICLCs have the largest population. They have been identified both in the uterus of rats and human [27], with a population of $\sim$10% (ratio between the number of ICLCs to that of the total cell number in a uterus) [33, 27, 30]. In human uterus, the ICLCs density is about $100 - 150$ cells/mm^2. These cells scatter in the entire organ (see Fig.1.4), contributing $\sim$18% of the cell population immediately underneath the mucosal epithelium, and $\sim$ 7.5% in muscularis [30]. In shape, ICLCs are irregular, having multiple projections and/or a spider-like appearance. These spider-like appearance forms close connection with the surrounding myocytes [27, 30], as shown in Fig.1.3B.

1.4 Coupling induced oscillations

The increase in gap junctional coupling (due to increase in number of junctions as well as the conductance of the junction) is one of the most spectacular electrophysiological changes observed close to delivery. This increase suggests a prominent role of the coupling in the spontaneous appearance of electrical activity. In addition it has been shown that a reduced expression of connexin 43 (the components of gap junction proteins) in transgenic mice leads to a significantly delayed partutrition [50]. More spectacularly, it has been observed that disruption of the gap junctions by chemical means immediately inhibit the oscillatory uterine contractions [51, 52, 53]. The two former observations provide strong evidence that the gap junctional coupling plays a very significant role in the appearance of a coordinated electrophysiological activity in the uterus.

The recent numerical observation that coupling an excitable cell, whose behavior is similar to a myocyte, with a passive cell can lead to oscillations [54, 55], even though none of the two cells are oscillating, is particularly important in the context of our study. In cardiac tissue, physiological studies have revealed that gap junctions do couple myocytes to fibroblasts, which behave passively [56]. As shown in Fig.1.5, the smooth muscle cells, marked by red dye, are in direct contact to one or more fibroblasts *in-situ*.

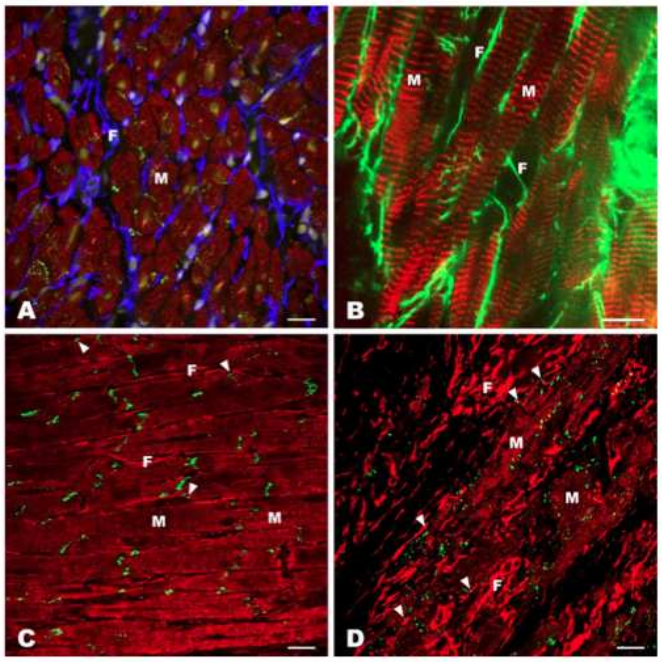

Figure 1.5: Fibroblast—myocyte interrealtion in the heart. Scale bars are 20μm in A, C, and D, and 10μm in B. M indicates myocyte; F, fibroblast. Replotted from Ref. [56].

In the uterus, would the coupling between myocytes and connective tissues be responsible for the initiation of the uterine spontaneous oscillations? Numerical work [54, 55] suggesting that the coupling between myocytes and passive cells can lead to oscillations was based on the study of very simplified ("generic") model of myocytes. It suggests that the qualitative results should also apply to a precise description of the uterine cells. Still, it remains to check quantitatively whether, and how, the qualitative conclusions of simplified models apply. As explained in Section 1.2.3, the newly available electrophysiological models [44, 43] provide a new opportunity to investigate the question.

1.5 Synchronizations

A biological tissue usually contains numerous functional elements. Its proper functioning requires a coordination of events of all its components, *i.e.,* all the elements need to be synchronized. In the case of the heart, a coordinated contraction is necessary to pump blood throughout the body. This is achieved by a synchronized contraction of the muscle cells. Lack of synchronization can lead to ventricular fibrillation [57, 58], which is the origin cardiac arrhythmias, a major cause of mortality. In human uterus, the mere existence of oscillating cells in the uterus is not enough to give rise to strong oscillations. To successfully expel the fetus, a coherent contraction of 100 billion

smooth muscle cells is required [49].

In fact, synchronization phenomena are ubiquitous nature. Studies in the attempt to understand how synchronization is achieved, have been carried out in the fields of physical, chemical and biological systems [59, 60, 61]. Usually, the systems mostly studied are only with one single type of elements: oscillatory [62] or excitable [63, 64].

In practice, in natural circumstances, the nonlinear oscillators constituting the system are not all strictly identical. As an example, the heart contains oscillatory (pacemaker) cells, excitable cells (myocytes), and passive cells (connective tissue, such as fibroblasts). The interactions of these elements generate different forms of coherent behavior: synchronous regime [59] and spiral waves [65, 66] have been observed experimentally. Much work has been devoted to heterogeneous system. Numerical studies have been carried out in ensembles of oscillatory and excitable elements [67] and ensembles of oscillatory and passive elements [68]. However, little has been done to reveal the mechanisms of synchronization in ensembles of excitable and passive elements. In these systems, no pacemaker cell exists. The mechanisms of synchronization in systems without pacemakers are of general interest, in the uterine context, as in possibly many others.

1.6 Main work of the thesis

The main objects of the thesis are to investigate, using a modelling approach, the hypothesis that the coupling between myocytes and passive cells can generate oscillatory behavior and to understand the mechanisms of transition from asynchrony to synchronized state by means of local interaction in a media without any coordinators, which are reminiscent to the appearance of forceful contractions in the uterus during pregnancy.

The thesis contains three parts. The first part focuses on the role the gap junction coupling in inducing uterine contractions using a more realistic model. To complete this analysis, a detailed investigation of different ionic channels and the construction of an uterine myocyte model are needed, which is the main focus of Chapter 2. In Chapter 3, the role of coupling is investigated using both FHN and the uterine myocyte model.

In the second part, we extend our discussion to tissue level (2D-uterine model) and focus on the mechanisms of transition from asynchrony to coherent state observed in uterus during pregnancy [69]. To make our discussion more general, we use the FitzHugh-Nagumo model and verify it with the realistic model in this part. Chapter 4 is devoted to an exploration of the different dynamical regimes observed by the increase of coupling strength, and to verifying the results using the realistic uterine model. Chapter 5 discusses the large fluctuations of the observed regimes and gives a qualitative explanation of the system size dependence of the observed dynamical regimes. The last part presents our conclusions, and discusses several potential new research directions.

Chapter 2

Description of smooth muscle cells

2.1 Overview of Hodgkin-Huxley model

Our understanding of neurons is based on the seminal work of Hodgkin and Huxley, which laid the ground for the modeling of the ionic channels and of the propagation of action potentials along nervous fibers [70, 71, 72, 8, 73]. For this outstanding work, Hodgkin and Huxley were awarded in 1963 the Nobel Prize for Physiology and Medicine.

The essential idea of the model is that the electrical properties of the cell's membrane can be modeled by an equivalent circuit of the form shown in Fig.2.1. The membrane potential, V_m, is defined as the difference between the internal and external potential across the cell membrane. The changes of the membrane potentials are the direct consequences of fluxes of ions through ion channels, represented by the active elements in Fig.2.1, which in turn lead to the charge of the membrane capacitance (denoted by C_m).

The giant squid axon, initially studied by Hodgkin and Huxley, has two main ionic channels, carrying sodium and potassium, in addition to a "leakage" channel. Using Ohm's law, it is straightforward to write the equations describing the evolution of the membrane potential:

$$C_m \frac{\mathrm{d}V_m}{\mathrm{d}t} + I_{\mathrm{ion}} = I_{\mathrm{ext}} \tag{2.1}$$

In Eq.(2.1), the convention is that a positive inward current flowing through ionic channels are counted as negative. Thus, a negative current tends to depolarize the cell, *i.e.*, to increase the value of the membrane potential. Note that in contrast, external current I_{ext} injected in the cell is counted as positive.

The total ionic current I_{ion} is the sum of currents due to the various ionic channels:

$$\begin{aligned} I_{\mathrm{ion}} &= I_{\mathrm{Na}} + I_{\mathrm{K}} + I_{\mathrm{L}} \\ &= G_{\mathrm{Na}}(V_m - E_{\mathrm{Na}}) + G_{\mathrm{K}}(V_m - E_{\mathrm{K}}) + G_{\mathrm{L}}(V_{\mathrm{m}} - E_{\mathrm{L}}) \end{aligned} \tag{2.2}$$

where G_i represents the conductance and E_i the equilibrium potential of each chan-

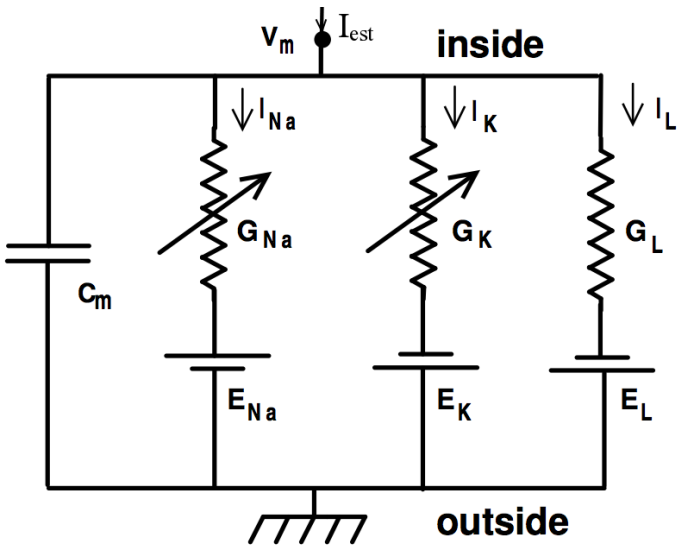

Figure 2.1: Equivalent electrical circuit of squid giant axon membrane proposed by Hodgkin and Huxley. C_m represents the membrane capacitance, G_i and E_i represent the voltage-dependent conductance and the equilibrium potential of different ionic channels (Hodgkin and Huxley [73]).

nel, and i =Na, K and L. The conductance G_i has been demonstrated to be voltage dependent, except the leakage channel, which is set to be a constant, describing the effect of chloride ions. Each individual channel contains a small number of physiological gates, which allows ions enter to and exit from the cell. An individual gate has two states called active and inactive, *i.e.*, open and close, regulated by the membrane voltage. At a particular potential, one active gate will contribute to a fraction the total conductance, while the inactive will not. Thus the conductance can be seen as being proportional to the product of the probability of each gate to be open.

Hodgkin and Huxley described the currents with the help of three variables: m and h, which describe, respectively, the states of active and inactive gate of the sodium channel: $G_{\mathrm{Na}} = \bar{g}_{\mathrm{Na}} m^3 h$, and n, which describes the state of active gate of potassium channel: $G_{\mathrm{K}} = \bar{g}_{\mathrm{K}} n^4$. The different powers of the gating variables count the number of activating and inactivating gates in the channel. The values of the number of gates depend on channel types as well as on animals. In the giant squid axon, it has been demonstrated that there were three activating and one inactivating gates in the sodium channel, and four activating gates and no inactivating gate in the potassium channel.

In the previous expressions, g_i represents the maximum conductance when the gate is open. The gating variables, m, h and n, describe the probability of opening of the gates. Their dynamics are described by:

$$\frac{\mathrm{d}x_i}{\mathrm{d}t} = \frac{x_{i\infty}(V_m) - x_i}{\tau_{x_i}(V_m)}, \qquad x \in \{m, h, n\} \tag{2.3}$$

Here $x_{i\infty}$ is the steady state of x at the potential V_m, and τ_{x_i} is the time constant of the gate at potential V_m. These two variables can be measured using voltage clamping technique [74]: applying a holding potential, the membrane potential is maintained at a constant value, which eliminates the capacitance current. The injected stimulating current is equal and opposite to the total current [75]. By selectively blocking the various channels, direct informations ($x_{i\infty}$,τ_{x_i}) can be obtained on each channel.

After the model has been developed to describe the squid giant axon [73], the Hodgkin-Huxley modeling approach has been applied to many other cells. In 1977, Beeler and Reuter applied it to reconstruct the action potential of mammalian ventricular myocaidial fibers [10]. With the later improving work by Lou and Rudy [12], this model has been applied to cardiac tissue [67], and largely improved our understanding the mechanism of heart diseases [76]. In 1983, Chay *et al.* first introduced the Hodgkin-Huxley model to the describption the pancreatic β-cell [77]. Combining the changes of the intracellular calcium concentration, this model unveiled the mechanism of bursting oscillations of the membrane potential observed in the pancreatic β-cell.

The success of Hodgkin-Huxley model encourages biophysicists to construct models on different cell types, in the hope of gaining a better understanding of life. During the last decade, several uterine myocyte models have been proposed, all of them are based on the original Hodgkin-Huxley model [47, 78, 43, 44]. In the following, we propose such a model to describe uterine myocytes' electrical activities using the most developed works recently published [43, 44].

2.2 Model of a uterine myocyte: approach of Rihana *et al.*

We began our study of uterine myocyte models with the work of Rihana *et al.* [43]. This model incorporates six main ionic channels in the description: the sodium (Na), calcium (Ca), the potassium (K), the calcium activated potassium (K(Ca)) and the leakage channel (L), as shown in Fig 2.2. As before, g_i indicates the conductance of each channel, and E_i its reversal potential. The total current through the membrane ionic channels reads as:

$$\begin{aligned} I_{\text{ion}} =& g_{\text{Ca}}(V_m - E_{\text{Ca}}) + g_{\text{Na}}(V_m - E_{\text{Na}}) \\ &+ g_{\text{K}}(V_m - E_{\text{K}}) + g_{\text{K(Ca)}}(V_m - E_{\text{K}}) + g_L(V_m - E_L) \end{aligned} \tag{2.4}$$

The dynamics of the membrane with an external stimulus current can be expressed by the Eq. (2.1).

The description of the ionic channels is based on voltage clamp experiments, as described in the previous section. Rihana *et al.* [43] incorporated the available experimental measurements reported in the literature, to build their models. However, some information could not be found in the literature. To address this problem, Ri-

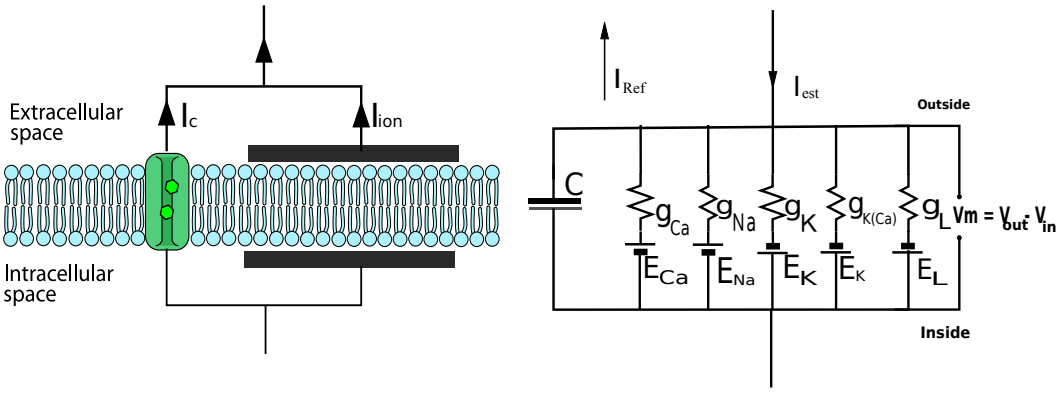

(a) Electrical circuit model (b) Electrical circuit model

Figure 2.2: (a) Uterine cell transmembrane current is divided into capacitive current (I_C) and ionic current (I_{ion}). (b) Electrical activity is modeled by a simple electrical circuit. g_i and E_i indicate the conductance and the reversal potential of each channel.

hana *et al.* had to specify a number of (otherwise unknown) parameters. While the results presented in Ref. [43] are reasonable, we never had access to all parameters in their model. For this reason, we determined ourselves these parameters, using the procedure described below, which is essentially based on the available experimental results, as explained in the following sections. In the following, we will give a detailed description of the sodium, calcium, potassium channels and the other channels.

2.2.1 Sodium Channel

The sodium current, $I_{\mathrm{N}a}$ flows inside the cell (inward current). In the spirit of the Hodgkin-Huxley equation, we express this current as:

$$I_{\mathrm{Na}} = G_{\mathrm{Na}} h_{\mathrm{Na}} m_{\mathrm{Na}}^4 (V_m - E_{\mathrm{Na}}) \tag{2.5}$$

The fourth power of the gating variable m_{Na} is chosen because of the presence of four activating gates in the sodium channel. E_{Na} is the sodium reversal potential, we take $E_{\mathrm{Na}} = 83mV$, for reasons explicated later (see page 17). The other parameters need to be extracted from literature.

- Sodium gating variables

The variation of each variable (m and h) can be expressed by a first order differential equation same as Eq. (2.3):

$$\frac{\mathrm{d}m_{\mathrm{Na}}}{\mathrm{d}t} = \frac{m_{\mathrm{Na}\infty}(V_m) - m_{\mathrm{Na}}}{\tau_{m\mathrm{Na}}(V_m)} \tag{2.6a}$$

$$\frac{\mathrm{d}h_{\mathrm{Na}}}{\mathrm{d}t} = \frac{h_{\mathrm{Na}\infty}(V_m) - h_{\mathrm{Na}}}{\tau_{h\mathrm{Na}}(V_m)} \tag{2.6b}$$

Here $\tau_{m\mathrm{Na}}$ and $\tau_{h\mathrm{Na}}$ are the relaxation time constants, which are voltage dependent. Yoshino *et al.* [33] measured the time constants at different potentials for both activation and inactivation (see table 2.1 and 2.2).

Table 2.1: Activation time constant of Na channel

$Vm(mV)$	-20	-10	0	10	20
$\tau_m(ms)$	0.39	0.32	0.26	0.2	0.18

Table 2.2: Inactivation time constant of Na channel

$Vm(mV)$	-10	0	10	20	30
$\tau_h(ms)$	0.77	0.59	0.49	0.42	0.41

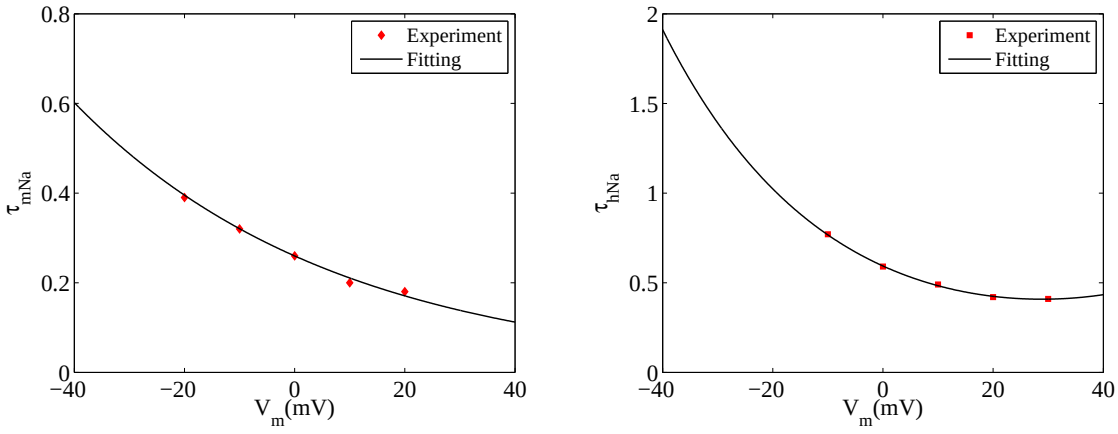

(a) ativation time constant

(b) inativation time constant

Figure 2.3: Time constants of sodium channel as function of the transmembrane potential. ◇ and □ denote data extracted from the literature. Solid curves show the fitting to the experimental data.

By fitting this data with an exponential function, we obtain a simple expression for the time constant of both activation and inactivation gating variables:

$$\tau_{m\mathrm{Na}} = 0.2598e^{-0.021V_m} \tag{2.7a}$$

$$\tau_{h\mathrm{Na}} = 0.5034e^{-0.033V_m} + 0.09e^{0.03V_m} \tag{2.7b}$$

as shown in Figure 2.3.

In Equation 2.6, $m_{\mathrm{Na}\infty}$ and $h_{\mathrm{Na}\infty}$ denote the activation and inactivation steady states, both of which follow a Boltzman distribution.

$$m_{\mathrm{Na}\infty} = \frac{1}{1+\exp\frac{V_m - V_{h\mathrm{Na}_m}}{k_{\mathrm{Na}_m}}} \tag{2.8}$$

$$h_{\mathrm{Na}\infty} = \frac{1}{1+\exp\frac{V_m - V_{h\mathrm{Na}_h}}{k_{\mathrm{Na}_h}}} \tag{2.9}$$

where the half activating ($V_{h\mathrm{Na}_m}$) and inactivating potentials ($V_{h\mathrm{Na}_h}$) and their slopes (k_{Na_m}, k_{Na_h}) are given by Ref. [33], i.e., $V_{h\mathrm{Na}_m}$ = -21mV, $k_{\mathrm{Na}_m} = -5$mV, $V_{h\mathrm{Na}_h}$ = -58.9mV, $k_{\mathrm{Na}_h} = 8.7$mV, respectively.

- Sodium Conductance

To fully determine the current due to the sodium ions, we also need to know the value of the maximum conductance G_{Na}. It is not given explicitly in any reference, but we can extract this value by doing a set of *in-silico* voltage-clamp experiments (see Fig.2.4) on Na-channel using different trial value of G_{Na}.

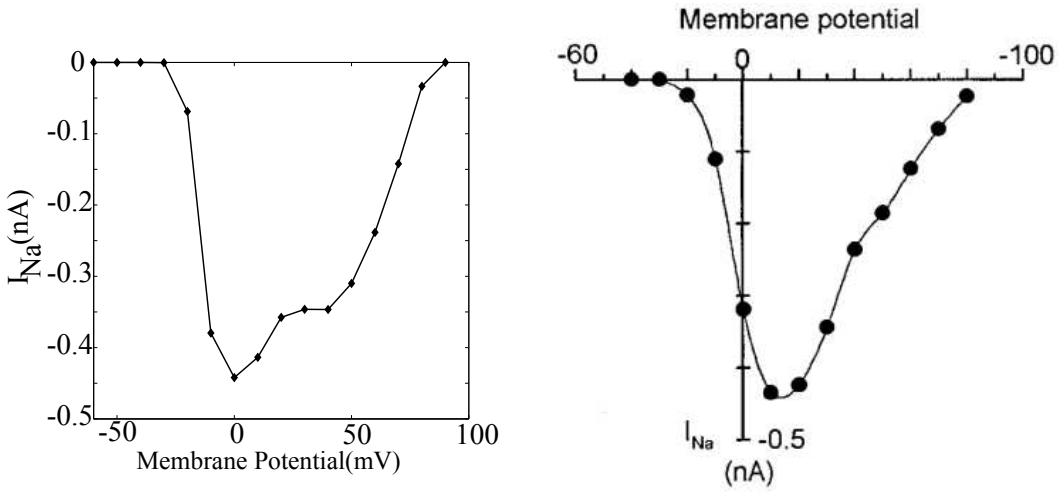

Figure 2.4: Comparison of voltage-clamp experiment on mathematical model and a real cell. A, I-V relationship measured from the model, here we use the surface area of the cell is 9000μm^2 [33]. B, Experimental data in [33] fig.3(D).

For comparison, we took the same voltages protocol as [33] and found that if we set $G_{\mathrm{Na}} = 0.31\mathrm{mS/cm}^2$, the result of numerical experiment reproduces the four main features described in [33], namely:

1. I_{Na} first appears at ∼-40mV;
2. I_{Na} reaches a maximum at 0-10mV;
3. taking into account the morphometric surface areas, the peak current density is $I_{\mathrm{Na}} = 5.1\mu A/cm^2$;
4. I_{Na} reverses at 80-84mV, as shown in Fig.2.4.

Using the fourth feature, we derive $E_{\mathrm{Na}} = 83\mathrm{mV}$. This model is further validated by simulating a voltage-clamp experiment using the following voltage protocol: the current is recorded by holding the membrane potential at $-80mV$ for 10 ms, and step increasing to (depolarizing to) $10mV$. When we take into account the morphometric surface area S (=$9000\mu m^2$) of the cell [33] (we used this value of S throughout this work), its response is very close to a real cell, shown in Fig.2.5

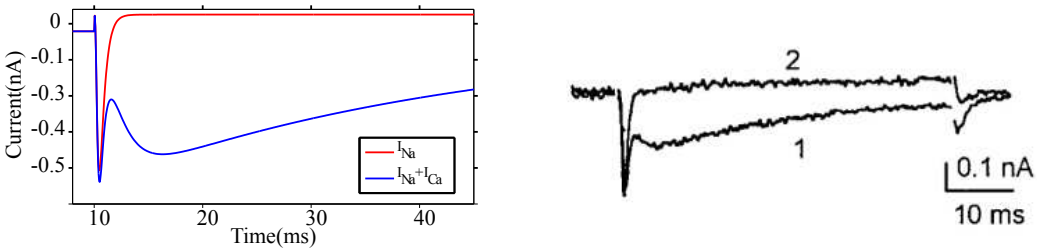

(a) (b)

Figure 2.5: Validation of the theoretical model of Na channel. (a) Response of the Na channel (red curve) when a voltage-clamp experiment is applied using the same voltage protocol: holding potential at -80 mV and depolarizing to 10mV. (b) Real experimental data(curve 2) from [33] .

2.2.2 Calcium Channel

I_{Ca} is the main component of the inward currents in uterine myocytes. It has a slow dynamics, and is present in all stages of pregnancy [33]. As it is the case for the Na channel, I_{Ca} is expressed by the following equation:

$$I_{\mathrm{Ca}} = G_{\mathrm{Ca}} m_{\mathrm{Ca}}^2 h_{\mathrm{Ca}} (V_m - E_{\mathrm{Ca}}) \tag{2.10}$$

Here m_{Ca} is Ca channel activating probability, h_{Ca} the inactivating probability, and we assume that there are two activating gates for the Ca channel [43].

- Calcium gating variables

Calcium channel is a little complicated. There are two types of Ca channel: the $L-type$ and $T-type$ [79, 80]. Experimental studies demonstrate that the *L-type* is the prominent component of I_{Ca} found in rat uterus [33, 81]. In the model, we keep only $L-type$ channel, and neglect the $T-type$ current. As it was the case for the Na channel, a first order differential equation describes the evolution of the gating variables m_{Ca} and h_{Ca}:

$$\frac{\mathrm{d}m_{\mathrm{Ca}}}{\mathrm{d}t} = \frac{m_{\mathrm{Ca}\infty}(V_m) - m_{\mathrm{Ca}}}{\tau_{m\mathrm{Ca}}(V_m)} \tag{2.11a}$$

$$\frac{\mathrm{d}h_{\mathrm{Ca}}}{\mathrm{d}t} = \frac{h_{\mathrm{Ca}\infty}(V_m) - h_{\mathrm{Ca}}}{\tau_{h\mathrm{Ca}}(V_m)} \tag{2.11b}$$

To give a better description of the Ca channel, Yoshino [33] pointed out that the inactivation in a myocyte should be fitted by two exponential terms. Following this suggestion, we split Eq. 2.11b into two parts: fast inactivation $h_{\mathrm{Ca}f}$ and slow inactivation $h_{\mathrm{Ca}s}$, each of which follows Eq 2.11b. These two components of inactivation have very different time constants, hence the denomination *fast* and *slow*. As we have not been able to find any article stating that their steady states are different, we assume $h_{\mathrm{Ca}f\infty} = h_{\mathrm{Ca}s\infty} = h_{\mathrm{Ca}\infty}$. Taking into account the different weight of each components in the total inactivation, h_{Ca} is expressed as [33]:

$$h_{\mathrm{Ca}} = 0.38h_{\mathrm{Ca}s} + 0.22h_{\mathrm{Ca}f} + 0.06 \tag{2.12}$$

where 0.06 is added to describe the small non-inactivating or very slowly inactivating component.

– Calcium time constants

The time constants can be obtained by fitting the data found in [33]. For the activation time constant, the data found are listed in Tab. 2.3. which we fitted with:

Table 2.3: Activation time constant of Ca channel

V_m(mV)	-10	0	10	20	30
$\tau_{m\mathrm{Ca}}$(ms)	2.16	1.82	1.62	1.47	1.37

$$\tau_{m\mathrm{Ca}} = 0.64e^{-0.04*Vm} + 1.188 \tag{2.13}$$

Eq.2.13 describes well the relationship between membrane potential and the time constants. Similar method applied to Ca inactivating channel works out the fast inactivation time constants:

$$\tau_{h\mathrm{Ca}f} = -0.00061V_m^3 + 0.074V_m^2 - 1.5V_m + 41 \tag{2.14}$$

Table 2.4: Fast inactivation time constant of Ca channel

V_m(mV)	-10	0	10	20	30	40
$\tau_{m\mathrm{Ca}f}$(ms)	64	42	32	34	46	58

The measurements concerning the slow inactivation time constant,$\tau_{h\mathrm{Cas}}$, are scarce. It is found that $\tau_{h\mathrm{Cas}}$ is voltage dependent (175 ms at -10 mV, 81 ms at $+20$ mV, 289 ms at $+40$ mV) [33]. We cannot define an exact equation only from this data. Considering the fact that $\tau_{h\mathrm{Cas}}$ is small, we assume that it is a constant, and take the same value as Rihana *et al.*, $\tau_{h\mathrm{Cas}} = 160$ ms.

– Calcium steady states

Calcium steady states $m_{\mathrm{Ca}\infty}, h_{\mathrm{Ca}\infty}$ also follow the Boltzman distribution:

$$\begin{aligned} m_{\mathrm{Ca}\infty} &= \frac{1}{1+\exp(\frac{V_m - V_{h\mathrm{Cam}}}{k_{\mathrm{Cam}}})} \\ h_{\mathrm{Ca}\infty} &= \frac{1}{1+\exp(\frac{V_m - V_{h\mathrm{Cah}}}{k_{\mathrm{Cah}}})} \end{aligned} \tag{2.15}$$

et al. studied the calcium channel of rat uterine myocyte and gave a half inactivation potential $V_{h\mathrm{Cah}} = -34$mV with a slope $k_{\mathrm{Cah}} = 5.4$mV and a half activation potential of $V_{h\mathrm{Cam}} = -7.4$mV with the slope of $k_{\mathrm{Cah}} = -6.6$mV. One year later, Shmigol *et al.* [42] published results on the same cell, giving $V_{h\mathrm{Cah}} = -53$mV,$k_{\mathrm{Cah}} = 9.9$mV and $V_{h\mathrm{Cam}} = -27.0$mV, $k_{\mathrm{Cam}} = -11$mV. This deviation suggests a possible range of these characteristic variables.

In the study here, we take: $V_{h\mathrm{Cah}} = -34$mV, $k_{\mathrm{Cah}} = 5.4$mV for inactivation and $V_{h\mathrm{Cam}} = -25.4$mV, $k_{\mathrm{Cah}} = -7.6$mV for activation, values in the range of the two studies.

- $[\mathrm{Ca}^{2+}]_i$ Dynamics

Experiments have demonstrated the relation between the intra-cellular calcium concentration, noted as $[\mathrm{Ca}^{2+}]_i$, and the electrical activity [82]. The rises in intracellular concentration are essential for contraction in human myometrial smooth muscle cells [19]. However, to achieve normal functionality, the concentration needs to be maintained at a certain level in the form of oscillation [83, 84]. Several mechanisms permitting the regulation of the calcium concentration have been identified [85, 86]. The sarcoplasmic reticulum(SR) absorb Ca^{2+} and store it for later use, thus functioning as a buffer to adjust (limit) the cytosolic Calcium concentration [85]. Taking into account that calcium flux from calcium channels, the governing equation can be

written as [77]:

$$\frac{\mathrm{d}[\mathrm{Ca}^{2+}]_i}{\mathrm{d}t} = f_c(-\alpha I_{\mathrm{Ca}} - k_{\mathrm{Ca}}[\mathrm{Ca}^{2+}]_i) \tag{2.16}$$

where f_c is the fraction of free $[\mathrm{Ca}]^{2+}$ inside the cell which has values between 0.01and 0.001 [77], and α is a constant describing contribution of I_{Ca} to the intracellular concentration. In view of the standard convention that ionic current is counted as positive *outwards*, so the minus sign before α expresses the fact that a positive (outward) Calcium current reduces the cytosolic Calcium concentration. According to [77], this value is defined as $\alpha = \frac{S}{vF}$, where S and v are the area and volume of the cell, and F is the Faraday Constant. With the morphological data of uterine myocyte found in [33], we get $\alpha = 4 \times 10^{-5}\mathrm{mol}\cdot\ \mathrm{cm}^{-1}\mathrm{C}^{-1}$. k_c is the rate constant for the removal of Ca^{2+}, which is in the rang of $0.01 \sim 0.06\ \mathrm{ms}^{-1}$.

The change in the Ca^{2+} will cause changes in the equilibrium potential of calcium channel E_{Ca}, which can be described by the Nernst equation [87]

$$E_{\mathrm{Ca}} = \frac{RT}{zF} \ln \frac{[\mathrm{Ca}^{2+}]_o}{[\mathrm{Ca}^{2+}]_i} = \frac{25.8}{2} \ln \frac{[\mathrm{Ca}^{2+}]_o}{[\mathrm{Ca}^{2+}]_i} \tag{2.17}$$

where $[\mathrm{Ca}^{2+}]_o$ is the extracellular calcium concentration. Both $[\mathrm{Ca}^{2+}]_o$ and $[\mathrm{Ca}^{2+}]_i$ are both expressed in mM, and E_{Ca} is expressed in mV. In all the work done here, we assume the calcium extracellular concentration is constant(the value of $[\mathrm{Ca}^{2+}]_o$ changes relatively little compared to the intercellular Calcium concentration), We take the value of $[\mathrm{Ca}^{2+}]_o = 3$ mM, as specified *in vitro* experiment [33] .

- Calcium Conductance

The Calcium conductance, G_{Ca} has not been documented in the literature. To determine this value from the available experiments, we took $f_c = 0.005$ and $k_{Ca} = 0.06\ \mathrm{ms}^{-1}$, according to the reported values by Chay *et al* [77] and simulate a set of voltage clamp experiments with the Ca^{2+} channel by applying the same voltage protocols as Yoshino *et al.*, *i.e.,* holding the membrane potential at $V_h = -60mV$, and step depolarizing to different potential. The recorded peak calcium current is plotted in Fig: 2.6 as open circles. For comparison, we also plotted the *in–vitro* experimental data reported by Yoshino *et al.* [33]. We found that when we set $G_{\mathrm{Ca}} = 0.135\ \mathrm{mS/cm}^2$, the current voltage relationship of the model reproduces the three main features of the channel published by Yoshino and collaborators [33]; see in particular the open circles in Fig: 2.6. Namely, we find that

1. first current is detected at ≈ - 30 mV;
2. maximum current is obtained at ≈10mV;
3. maximum current is $5.67\mu\mathrm{A/cm}^2$

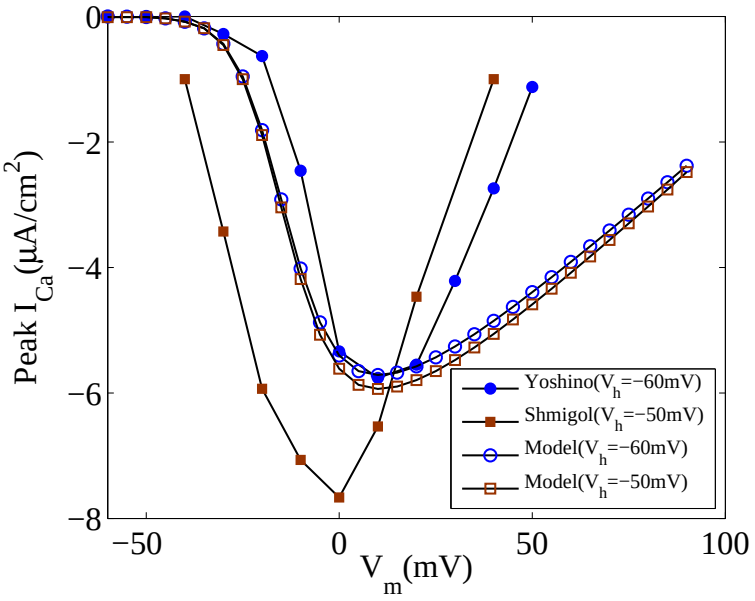

Figure 2.6: Relation between the measured peak calcium current I_{Ca} and membrane potential in the model V_m in vitro experiments (filled symbols) and in the model (open symbols). Circles, voltage clamping experiments using protocols same as Yoshino *et al* [33]: Holding potential V_h =-60mV, step depolarizing to different high potentials. Squares, voltage clamping experiments using protocols same as Shmigol *et al* [42]: Holding potential V_h=-50mV, step depolarizing to different high potentials. Parameters: $G_{\mathrm{Ca}} = 0.135$ mS/cm^2, $f_c = 0.005$, $k_{Ca} = 0.06$ ms^{-1}

After the determination of the maximum calcium conductance G_{Ca}, the model can be further tested by carrying out a set of simulations mimicking the *in–vitro* voltage clamping experiments.

- Validation of Ca^{2+} channel description

Validation of the mathematical description of Ca^{2+} channel is carried out by comparing the response of the model under voltage clamping conditions to that of a real cell as described in [42] and [33]. We simulated the dynamics of the Calcium channels in order to compare the relationship between $[Ca^{2+}]_i$ and I_{Ca}. The membrane potential was held at a value of -50 mV during 1s, then changed to values ranging from -60mV to 90mV for a duration of 200ms. We measured the variation of $[Ca^{2+}]_i$ and the peak of the current I_{Ca}; the values found are shown in Fig.2.7a. This procedure is identical to the one used experimentally in [42], with rat uterine myocytes; the corresponding figure is shown in Fig.2.7b. We find that the values of the currents are very similar when the membrane potential is less than $\approx$ 10mV.

Note that in order to compare qualitatively with the experimental results of [42] and [33], we converted the values of the currents in nA to μA/cm^2, by assuming the

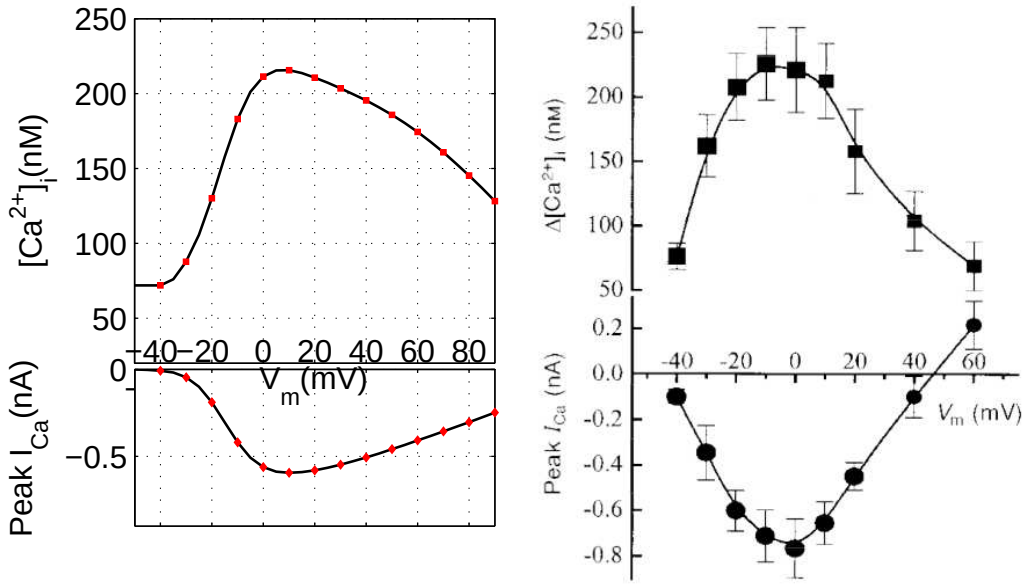

(a) Model (b) Experimental data

Figure 2.7: Effects of varying the magnitudes of the depolarization on $[Ca_i^{2+}]$ and I_{Ca}. (a) simulation of depolarization steps to the voltages from $-60mV$ to 90mV of duration of 200ms from a holding potential of −50mV. Variation of $[Ca^{2+}]_i$(top) and I_{Ca}(bottom) are plotted. (b) Real experiments carried by Shmigol *et al* [42].

area of the cell surface is $9000\mu m^2$, and plotted the *peak* I_{Ca} as a function of V_m, see Fig 2.6.

The model give values of the peak of I_{Ca} intermediate with the values reported in Yoshino [33] or Shmigol [42] when $V_m < 10$ mV. Significant deviations are seen when the membrane potential is larger than 20 mV. In a real cell, the inward current is quickly inactivated, and is completely blocked at a potential ≈ 60 mV. However, the model suggests that the Calcium current still exists, up to a membrane potential of ≈ 100 mV. In effect, the deviations at high holding potentials have little effect, since no membrane potential high than ~ 20mV are observed.

2.2.3 Potassium Channel

The description of the potassium channel is more complicated than the description of the sodium or calcium channels. Both Wang *et al.* [34] and Knock *et al.* [88] pointed out that fitting the relationship between current and membrane potential requires three components, which suggests the existence of three different potassium channels. In the model, we therefore split the potassium currents into three elements, K_1, K_2 and K_3, with n_1, n_2, h_1 and h_2 denoting the activating and activating variables of K_1 and K_2, respectively. The K_2 inactivation h_2, which is very slow (see below), is assumed

to be constant, and therefore, remains constant during the processes studied here. For the third element, K_3, no inactivation has been found [34], and the activation is very fast. For this reason, the variable n_3 is replaced by the asymptotic value $n_{K_3,\infty}$. Taking all these factors into account, the potassium current is expressed by the equation:

$$I_K = (G_{K_1} n_{K_1} h_{K_1} + G_{K_2} n_{K_2} + G_{K_3} n_{K_3\infty})(V_m - E_K) \tag{2.18}$$

Here G_i $(i = 1, 2, 3)$ is the maximum conductance of the K_i component. The parameters G_{K1}, G_{K2} and G_{K1} are set to 0.254, 0.064 and 0.033 mS/cm^2 according to [34]. The equilibrium potential E_K is in the range of $-70 \sim -80$mV [89, 77], in the model we set this value to -70mV.

- Potassium gating variables

As usual, the dynamics of potassium channel is modeled by the following first order differential equations.

$$\frac{dn_{K_1}}{dt} = \frac{n_{K_1\infty} - n_{K_1}}{\tau_{n_{K_1}}} \tag{2.19a}$$

$$\frac{dh_{K_1}}{dt} = \frac{h_{K_1\infty} - h_{K_1}}{\tau_{h_{K_1}}} \tag{2.19b}$$

$$\frac{dn_{K_2}}{dt} = \frac{n_{K_2\infty} - n_{K_2}}{\tau_{n_{K_2}}} \tag{2.19c}$$

$$n_{K_3} = n_{K_3\infty} \tag{2.19d}$$

Here $n_{x\infty}$,$h_{x\infty}$ and τ_x $(x = K_1, K_2, K_3)$ are voltage dependent and time independent.

– Steady states

As mentioned above, the steady states of each channels follow a Boltzmann distribution, which is determined by its half potential ($V_{0.5x}$) and the slope (s_x). Available data can be obtained from Wang *et al.* [34] and Knock *et al.* [88]. The values used in this model are obtained from [34], which is based on rat uterine myocyte (see Table 2.5).

Table 2.5: Properties of each potassium channel

Item	rat uterine myocyte		
	K_1	K_2	K_3
$V_{0.5n}(mV)$	7.7	4.2	63.4
s_n (mV)	-23.7	22.1	-16.7
$V_{0.5h}(mV)$	-62.7	-21.2	-
s_h (mV)	6.3	5.7	-

$$n_{K1\infty} = \frac{1}{1+\exp(\frac{V_m-7.7}{-23.7})} \tag{2.20a}$$

$$h_{K1\infty} = \frac{1}{1+\exp(\frac{V_m+62.7}{6.3})} \tag{2.20b}$$

$$n_{K2\infty} = \frac{1}{1+\exp(\frac{V_m-4.2}{-22.1})} \tag{2.20c}$$

$$n_{K3\infty} = \frac{1}{1+\exp(\frac{V_m-63.4}{-16.7})} \tag{2.20d}$$

– Time constants

Ref. [34] is not sufficient to accurately obtain the time constants of each components. For example, for K_1 activation, $\tau_{n\mathrm{K}_1} = 10$ms at 20mV, $\tau_{n\mathrm{K}_1} = 4$ms at 70mV; for K_2 activation, $\tau_{n\mathrm{K}_2} = 18$ms at 20mV, $\tau_{n\mathrm{K}_2} = 9$ms at 70mV. Knock *et al.* [88] gave more detailed activation time constants on K_1 and K_2 components based on experiments on human uterine myocytes, reported in Table 2.6. We fit the data with an exponential expression (see Fig 2.8), and found that for K_1 the time constants of these two species are consistent, they can be fitted by the same expression. This is not the same for τ_{K_2}. In the model we take the equations from rat myocyte.

Table 2.6: Activation time constants of human and rat uterine myocyte

cell type	Human						rat	
V_m(mV)	-40	-30	-20	-10	0	10	20	70
$\tau_{n\mathrm{K}_1}$(ms)	186.3	110	58	40	28.1	22.5	10	4
$\tau_{n\mathrm{K}_2}$(ms)	\	33	20.5	17.5	13	9.5	18	9.0

The expressions for the inactivation time constants are not completely obvious. The inactivation time constant of K_1 is best fitted by two exponential terms: the fast and the slow ones [34, 88]. The recorded decay rate of K_1 current in rates showed that the fast term is voltage dependent and stabilized at 200ms, the slow term is voltage independent at $\sim$ 2.5s. For humans, the fast term is stabilized at $\sim$ 1016ms, the second at 5213ms. With these information, we are not able to fit the time constants. We merely notice that the reported time constants are very long compared to the duration of action potentials ($\sim$ 100ms). Larger time constant of K_1 inactivation will prolong the action potential duration (larger than 100ms), and the time that potassium current takes to reach the maximum value in voltage clamping experiments should be larger than the experimentally measured value: 32.5ms [34]. In the model, we set $\tau_{K_1} = 50$ms. K_2 component has a very slow inactivation (time constants $\sim$ 2100ms at 10mV in rat and 2552ms in human). Comparing with the duration of an action potential ($\sim$ 100ms), it is reasonable to assume that K_2 does not inactivate. This is why we fixed h_{K_2} to 1, which explains why h_{K_2} does not appear

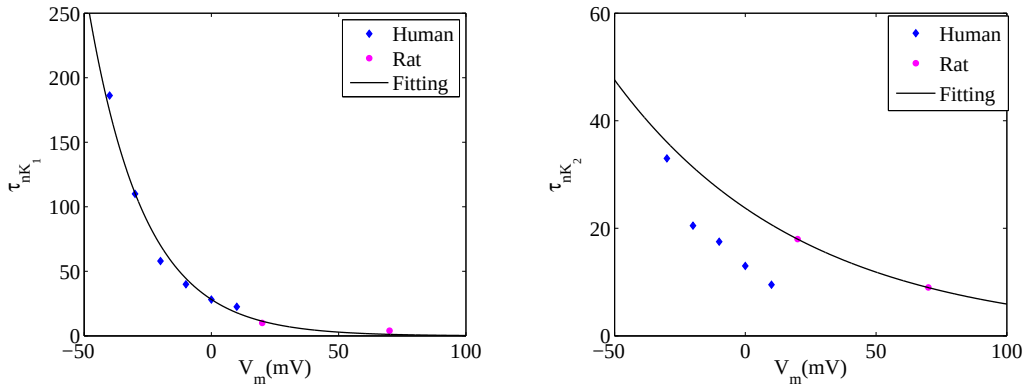

(a) $\tau_{n_{K_1}}$ (b) $\tau_{n_{K_2}}$

Figure 2.8: Time constant of each channel.(a) For K_1 channel, activation time constants of two species can be fitted by single curve: $\tau_{nK_1} = 28.23\exp(-\frac{V_m}{-21.8})$. (b) K_2 activation time constants of human and rat can't be fitted by a single curve. For rats, the fitted curve is: $\tau_{nK2} = 23.75\exp(-\frac{V_m}{-71.94})$.

in Eq. 2.18. In summary, the time constant expressions used in the model are the following:

$$\tau_{nK_1} = 28.23\exp(-\frac{V_m}{-21.8}) \tag{2.21a}$$

$$\tau_{nK_2} = 23.75\exp(-\frac{V_m}{-71.94}) \tag{2.21b}$$

$$\tau_{hK_1} = 50 \tag{2.21c}$$

- Validation of potassium channel description

In order to validate the description of potassium channel, and to check its accuracy, we performed numerically a set of voltage clamp experiments at a holding potential $-40mV$ and by steps depolarizing for 300 ms with 10mV increments to 70mV. The recorded membrane potential variations are plotted in Fig.2.9(a). For comparison, the *in–vitro* experimental results [34] is shown on the right side. One sees that the model confidently reproduces the experimental results: 1) no decay are observed within 300ms, 2) peak currents are detected at $\sim$ 32.5ms. A i–V_m relation of the currents at maximum is shown in Fig.2.10.

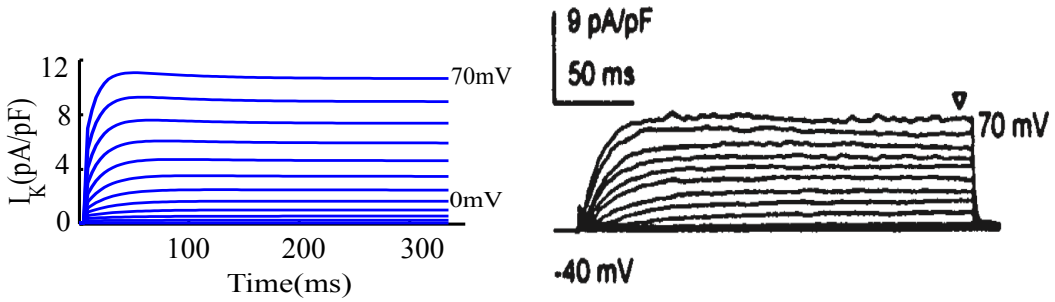

(a) model (b) experiment

Figure 2.9: A, Voltage clamp experiment on the K channel of the mathematical model with holding potential of -40mV, and step depolarized into 70mV with an increase of depolarizing potential of 10mV. B. Same experiments done on the real rat uterus cell by Wang *et al* [34].

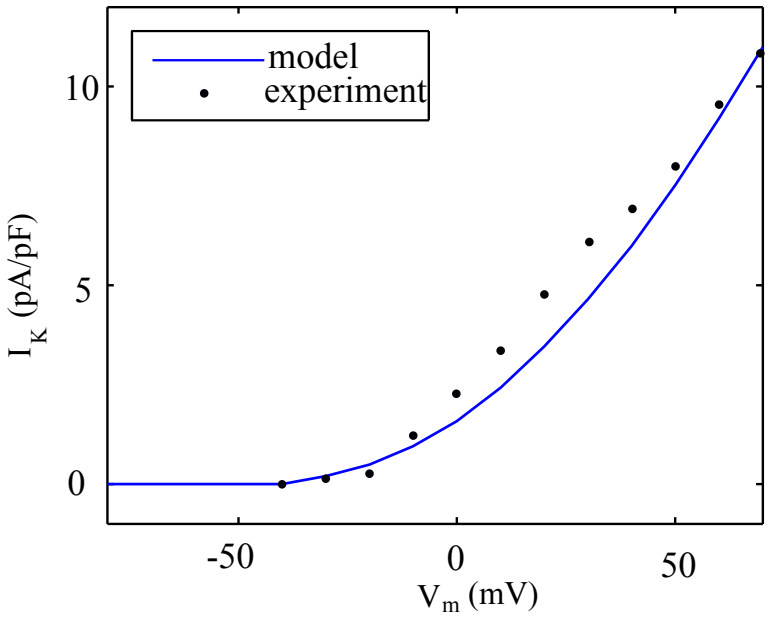

Figure 2.10: Maximum current of I_K using the voltage protocols in Figure 2.9. Blue solid line is obtained from the model. Black dots are data extracted from Wang *et al.* [34].

2.2.4 Calcium potassium dependent current

Besides the voltage-modulated potassium channels discussed above, there exists another potassium channel, whose activation by membrane potential is not fixed, but rather depends on the intracellular calcium concentration $[Ca^{2+}]_i$ [90]. The depen-

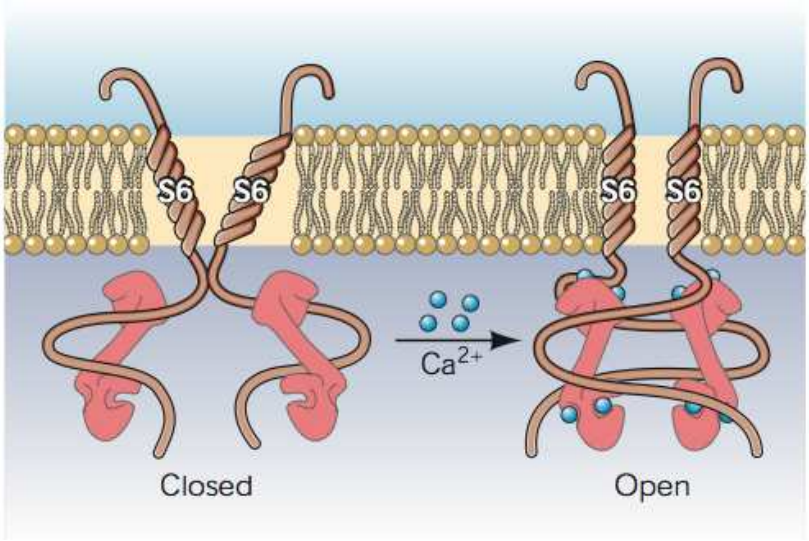

Figure 2.11: Schematic illustration of gating mechanism of the calcium activated potassium channel. Left, the gating is closed in the absence of calcium binding to the active protein. Right, by absorbing Ca^{2+} to the binding, K^+ can go through freely.

dence can be understood as following: The proteins forming the channel align tightly in the absence of Ca^{2+} bound to it, blocking the flux of potassium ions. While there are Ca^{2+} bound to the active sites of the proteins, these proteins separate, forming a pore, allowing K^+ to move freely, as illustrated in Fig.2.11. Thus the status of the channel can be described in terms of the fraction of sites bounded to Ca^{2+}.

The binding process of Ca^{2+} to the active sites of the proteins can be well modeled by the Langmuir equation, which describes the relation of adsorption of molecules on a solid surface to the molecule concentration above the solid surface at a fixed temperature. A statistical derivation of this model is given in [91]. When all the active sites are bound with Ca^{2+}, potassium ions pass this channel under electrochemical gradient with a conductance G_{KCa}. In a intracellular environment with a calcium concentration$[Ca^{2+}]_i$, the current pass through this channel can be described as:

$$I_{\mathrm{K(Ca)}} = G_{\mathrm{KCa}} \frac{[\mathrm{Ca}^{2+}]_i{}^N}{K_{1/2}^N + [\mathrm{Ca}^{2+}]_i{}^N} (V_m - E_{\mathrm{K}}), \tag{2.22}$$

with G_{KCa}=0.08 mS/cm^2,$K_{1/2}$=0.015mM, $N = 2$ given in [43].

Calcium-activated potassium current ($I_{\mathrm{K(Ca)}}$) has been suggested to play important roles in regulating the excitability of the uterus [92]. Three subclasses of calcium-activated potassium channels that are activated when intracellular Ca^{2+} levels rise have been identified [93].

2.2.5 Leakage Current

We have incorporated the most of the main ionic currents. Other currents, such as the chloride current [94] and sodium–potassium pump current [95] may also contribute to the electrical behavior. To these effect, a linear leakage current, described as [77]:

$$I_L = G_L(V_m - E_L) \tag{2.23}$$

is added, where the conductance $G_L = 0.0058$ mS/cm^2 and the equilibrium potential $E_L = -40$ mV are taken as in Ref. [77].

2.2.6 Limitations and Discussion

The model incorporates five ionic channels, with the help of experimental data coming mostly from references Yoshino [33] and Wang [34], as well as reference Chay [77] concerning the dynamics of the intracellular calcium concentration. The model therefore reproduces quantitatively records concerning specific ionic channels.

The description of the Calcium channels however does not come directly from experimental records, which are not available. As shown above, all measured values of the half activation voltage V_{hCam} and its slope k_{Cam} and half inactivation voltage $V_{h_{Cah}}$ and its slope k_{Cah} show large discrepancies in litterature. We took here some intermediate values. This choice provides a consistent description of the experimental records at low membrane potentials. As illustrated in Fig.2.6, the recorded calcium peak currents of the model under voltage clamping conditions with V_h<20mV are consistent with the experimentally measured values. As we are interested in the spontaneous action potentials which can not reach very high potentials, thus the model can be faithfuly used in the future studies.

However, there are limitations, as it is the case for *any* model of physiological process. First, the smooth muscle cell is a complex system: 5 ionic currents are an underestimate of the number of ion channels contributors to the myocyte membrane electrical behavior. Scientific efforts devoted to identify different ion channels presented in cells' membrane reveal other ion currents contributing to the generation of action potentials. Hyperpolarization activated current [96], non-selective cation current [97], sodium potassium pump current [98] and many others have been reported in pregnant rats. Second, there are more mechanisms regulating the intracellular calcium concentration. Shmigol et al pointed out that the Na-Ca exchanger is the main way to remove [Ca^{2+}] out of the cell; about 60-70% of the cytoplasmic [Ca^{2+}] removal was estimated to be via this exchanger [42]. However the current model doesn't take this into account. All these limitations prompt the construction of a more detailed model.

2.3 Model of a uterine myocyte: approach of Tong *et al.*

In 2011, Tong and collaborators [44] published a uterine model , which takes into account fourteen experimentally identified ionic currents as well as different mechanisms for regulating the intracellular calcium concentrations, as illustrated in Fig. 2.12.

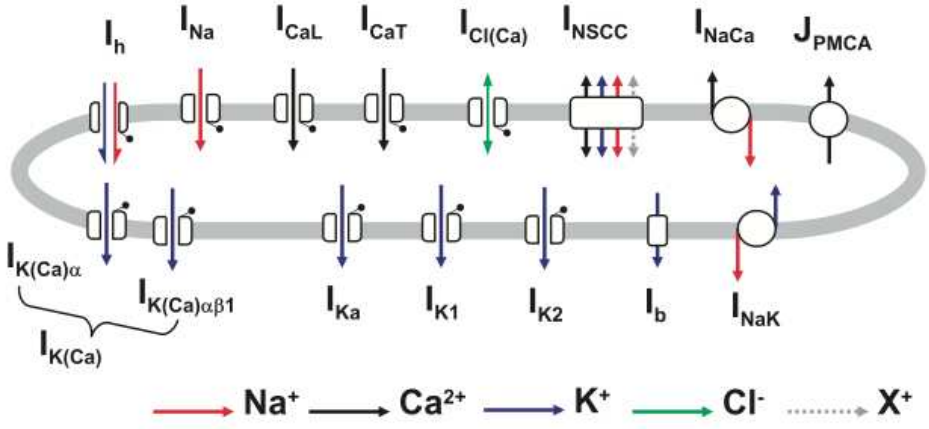

Figure 2.12: Schematic illustration of the uterine myocyte electrogenic components (replotted from [44])

2.3.1 Description of ion channels

Compared to the previous model, several new currents, namely $I_h, I_{\mathrm{Ca}_T}, I_{\mathrm{Cl(Ca)}}, I_{\mathrm{NSCC}}$, I_{NaCa} and I_{NaK}, are taken into account, while others remain the same but named differently. For example, the three fitted components of the potassium channels are called $\mathrm{K}_1, \mathrm{K}_2$ and A-type transient potassium current I_{K_a}. We here merely focus on the new ones for the reason of concision. As I_{NaCa} is directly related to the mechanisms of calcium removal, we discuss this current in Section 2.3.2.

- Hyperpolarization-activated current—I_h

The hyperpolarization-activated current I_h is common in smooth muscle cells. Its presence has been confirmed both in cardiac [99] and in rat uterine myometrial cells [96, 100]. Its role is not well understood. It may contribute to depolarize the membrane to the threshold potential and serve as a trigger for the generation of action potentials and/or as a quick depolarizing mechanism following strong after-hyperpolarization [96, 100].

Whole patch clamp experiments reveal that I_h is activated by hyperpolarization in a time- and voltage-dependent manner. This activation also follows a Boltzmann equation with a half-maximum activation potential of -84.3 mV and a slop factor of

9.6 mV. And the time constant can be well fitted by $\tau = 1/(\alpha + \beta)$ [100]. Differently, this current does not inactivate. Thus the same equation can be written down to describe the current with an activation gating variable y as:

$$I_h = G_h y(V_m - E_h) \tag{2.24}$$

Tong *et al.* [44] fitted the available data [100] and gave a detailed mathematical description.

- T-type Calcium current—I_{Ca_T}

Compared to L-type calcium current I_{Ca_L}, I_{Ca_T} is small, hence been ignored in Rihana's model. While experiments have confirmed its presence in both human and rat myometrial cells [101, 102]. Despite their tiny amount, it has been suggested to play a key role for the regulation of the frequency of spontaneous phasic contractions [102]. For this reason, Tong et al developed a model describing the electrophysiological characteristics of I_{Ca_T}. Detailed expressions are given in [44].

- Calcium-activated chloride current—$I_{\mathrm{Cl(Ca)}}$

Channels permeable to chloride ions were first reported by Coleman and Parkington [103]. Single cell voltage clamp experiments showed a linear relation between the chloride current and the membrane potential (see Fig.2 in [103]), suggesting a constant conductance to be used in describing the leakage current which is mainly due to I_{Cl} [73, 77]. However, the subsequent experiments revealed that there was also other type chloride current, the calcium-activated chloride current [104, 94]. The detailed single cell electrophysiological assessment of $I_{\mathrm{Cl(Ca)}}$ in rat myometrial cells done by Jones *et al.* [94] allowed Tong *et al.* to model this current precisely. Detailed expressions are given in [44].

- Non-selective cation current—I_{NSCC}

The non-selective cation current in late pregnant rat myometrial cells was first reported by Miyoshi *et al.* [97]. This current is time-independent and permeable to K^+, Na^+, Cs^+ and Ca^{2+}, with relative permeability ratios of $P_K : P_{Cs} : P_{Na} : P_{Ca} = 1 : 3 : 1 : 0.9 : 0.89$ [97]. To determine the current, Tong *et al.* modeled I_{NSCC} with data from late pregnant rat myometrial cells recorded at room temperature. Detailed model expressions are given in [44].

- Sodium potassium pump current—I_{NaK}

The presence of this current has been confirmed both in pregnant rat [98] and human myometrail cells [19]. It is suggested this current plays a role in regulating myometrial activity, but there is little information available about the biophysical properties of I_{NaK} in myometrial cells. Thus, Tong s *et al.* took the formulation of an electrogenic I_{NaK} from rodent myocardial cells [105], by assuming the same $[Na^+]_o$ dependency with I_{NaK} in smooth muscle cells as in the myocardial cells. Detailed model expressions are given in [44].

2.3.2 Intracellular calcium dynamics

The change of intracellular calcium concentration $[Ca^{2+}]_i$ is of crucial importance for the proper functioning of the uterus: it is a ubiquitous signaling mechanism that organizes the coordinated contractions [32, 82]; the spontaneous phasic contraction of uterine smooth muscle - myometrium, is related to an increase in the concentration of intracellular free Ca^{2+} [106]. Mechanisms regulating the intracellular calcium concentration include (i) the Na^+-Ca^{2+} exchanger [86]; (ii) the plasma-membrane Ca^{2+} ATPase pump [107]; and (iii) membrane calcium channels. Thus the net concentration of $[Ca^{2+}]_i$ is controlled by:

$$\frac{\mathrm{d}[Ca^{2+}]_i}{\mathrm{d}t} = -(J_{\mathrm{Ca,men}} + J_{\mathrm{NaCa}} + J_{\mathrm{PMCA}}) \tag{2.25}$$

Here $J_{\mathrm{Ca,mem}}$, J_{NaCa} and J_{PMCA} stand for the three main calcium flux in myometrial cell.

- Na^+-Ca^{2+} exchanger

The Sodium-Calcium exchanger is the main agent responsible for removing Calcium out of the cell: it carries about $60-70\%$ of the total amount extruded from the cytosol [42]. This exchanger takes *one* Calcium ion out, while bringing *three* Sodium ions into the cell, thus carrying in a net positive charge. The exchanger therefore results in a net inward current. As explained in Chapter 2, this inward current thus contributes to the depolarization of the cell, while the outward flux of Calcium would tend to hyperpolarize the cell. Thus the exchanger current I_{NaCa} reads as:

$$I_{\mathrm{NaCa}} = -\frac{1}{2} \times \frac{z_{\mathrm{Ca}} F V_c}{C_m A_c \beta} J_{\mathrm{NaCa}} \tag{2.26}$$

where C_m is the membrane capacitance, F is the Faraday constant, A_c and V_c are cell's surface area and volume respectively, β is a buffering coeffecient, and z_{Ca} is the valence of calcium ion. A pre-factor $-\frac{1}{2}$ is added for the consideration of the opposite direction of J_{NaCa} and I_{NaCa}, as well as the ratio of Na^+:Ca^{2+}=3:1.

The model simulation of Ca^{2+}-Na^+ exchanger current was first proposed by Weber *et al.* in 2001 [86]. This current is expressed as the product of an electrochemical ΔE and an allosteric factor *Allo*, i.e.,

$$\mathrm{I_{NaCa}} = (Allo)(\Delta \mathrm{E}) \tag{2.27}$$

where,

$$\Delta E = \frac{\mathrm{V_{max}}\{[\mathrm{Na^+}]_i^3[\mathrm{Ca^{2+}}]_o \mathrm{e}^{\frac{\gamma VF}{RT}} - [\mathrm{Na^+}]_o^3[\mathrm{Ca^{2+}}]_i e^{\frac{(\gamma-1)VF}{RT}}\}}{\left(\begin{array}{l}\mathrm{K}_{m\mathrm{Ca}_o}[\mathrm{Na^+}]_i^3 + \mathrm{K}_{m\mathrm{Na}_o}^3[\mathrm{Ca^{2+}}]_i + \mathrm{K}_{m\mathrm{Na}_i}^3[\mathrm{Ca^{2+}}]_o(1+\frac{[\mathrm{Ca^{2+}}]_i}{\mathrm{K}_{m\mathrm{Ca}_i}})+ \\ \mathrm{K}_{m\mathrm{Ca}_i}[\mathrm{Na^+}]_o^3(1+\frac{[\mathrm{Na^+}]_i}{\mathrm{K}_{m\mathrm{Na}_i}}) + [\mathrm{Na^+}]_i^3[\mathrm{Ca^{2+}}]_o + [\mathrm{Na^+}]_o^3[\mathrm{Ca^{2+}}]_i\end{array}\right)(1+k_{sat}\mathrm{e}^{\frac{(\gamma-1)VF}{RT}})} \tag{2.28}$$

and

$$Allo = \frac{1}{1+(\frac{\mathrm{K_{mCaact}}}{[\mathrm{Ca^{2+}}]_i})^n}$$

describes dependence of the adsorption of calcium ion to regulatory sites on $[\mathrm{Ca^{2+}}]_i$ [91]. Table 1. lists the parameter values used in [44] and the original paper [86]. We noticed that in the code of the supplementary materials of Ref. [44], the calcium efflux tends (J_{NaCa}) to increase the intracellular calcium concentration, *i.e.,* a "+" is replaced by "-" in front of J_{NaCa} in Eq.(2.25). As the wrong equation of calcium concentration dynamics used in [44] during the fitting, we tend to use the original values except $K_{\mathrm{M,Caat}}$. This value shows a great discrepancy between the code and the notes in supplementary materials: in the note $K_{\mathrm{M,Caat}}$ is said to be 3×10^{-3} mM, while in code this values is set to be 3×10^{-4} mM. We here take an intermediate value of $K_{\mathrm{M,Caat}} = 0.00125$mM.

Table 2.7: parameter values

Variables	Tong(supplementary)	Tong(code)	Weber	XU
$\mathrm{V_{max}}$(pA/pF)	11.67	11.67	22.6	22.6
$\mathrm{K_{mCaact}}$(mM)	3×10^{-3}	3×10^{-4}	0.125×10^{-3}	1.25×10^{-3}
$\mathrm{K}_{m\mathrm{Na}_i}$(mM)	30	30	12.3	12.3
$\mathrm{K}_{m\mathrm{Na}_o}$(mM)	87.5	87.5	87.5	87.5
$\mathrm{K}_{m\mathrm{Ca}_i}$(mM)	0.007	0.007	0.0036	0.0036
$\mathrm{K}_{m\mathrm{Ca}_o}$(mM)	1.3	1.3	1.3	1.3
n	4	4	2	2
k_{sat}	0.27	0.27	0.27	0.27
γ	0.35	0.35	0.35	0.35

- $\mathrm{Ca^{2+}}$ ATPase pump

The plasmalemmal $\mathrm{Ca^{2+}}$-ATPase (PMCA) is the second mechanisms of removing $\mathrm{Ca^{2+}}$ out from the cells. It is estimated to be responsible for about 30% of $\mathrm{Ca^{2+}}$ removal [108]. The efflux (J_{PMCA}) is described using Hill functions [91] as:

$$J_{\mathrm{PMCA}} = \frac{\bar{J}_{\mathrm{PMCA}}}{1+(\frac{\mathrm{K_{m,PMCA}}}{[\mathrm{Ca^{2+}}]_i})^{n_{\mathrm{PMCA}}}} \tag{2.29}$$

where n_{PMCA} is the Hill coefficient, $\bar{J}_{\mathrm{PMCA}}$ is the maximal velocity of Ca^{2+} extraction, and $K_{m,\mathrm{PMCA}}$ os the Ca^{2+} concentration for half-activation of the pump.

- Membrane calcium channels

The calcium current I_{Ca} is a direct consequence of the Ca^{2+} flow through the ionic channels. However this Ca^{2+} flow is further regulated by the sarcoplasmic reticulum (SR) [109]: SR takes up and stores calcium, using ATPase and the Ca-buffering proteins for later use. Consequently, only a fraction of this flow becomes free Ca^{2+} inside the cell. Taking into account this effect, $J_{\mathrm{Ca,men}}$ reads as:

$$J_{\mathrm{Ca,men}} = \frac{C_m A_c \beta}{z_{\mathrm{Ca}} F V_c} I_{\mathrm{Ca}} \tag{2.30}$$

where I_{Ca} is the total calcium current, including $I_{\mathrm{Ca}L}$, $I_{\mathrm{Ca}T}$ and the calcium component of the non-selective current I_{NSCC}.

2.3.3 Validation of the modified Tong model

Validations have been done by comparing the model response under voltage-clamping conditions with that of a real cell response reported the literatures, as done in [44]. As mentioned before, the model of Tong qualitatively reproduces the experimental data, which allows us to validate our modified version by comparing directly with the original version of the model.

Although the description of the Na^{+}-Ca^{2+} exchanger has been modified, no obvious difference concerning the calcium or potassium channel dynamics can be observed. As illustrated in Fig.2.13–2.15, the records obtained from the modified model collapse very well with the original records of the Tong model. In fact, no distinction can be made between these two models.

Fig.2.16 and Fig.2.17 test the Calcium concentration in the presence of a depolarizing current clamp: injecting a constant current, the variations of the membrane potential is recorded. Although, quantitative difference could be observed, the modified model behaves qualitatively like the original one. Furthermore, both models give a resting potential of -54mV, and an intracellular calcium concentration around 100nM. It has been mentioned in reference [44], that the original model produces a resting membrane potential of -19mV, and a basal intracellular calcium concentration of 610 nM under physiological conditions of ionic concentrations, as the outward Na^{+}–Ca^{2+} exchanger current contributes to hyper-polarize the membrane potential. Interestingly, with the modification introduced here, we do not find any unrealistic value of the membrane potential, even when the sodium conductance is not set to zero.

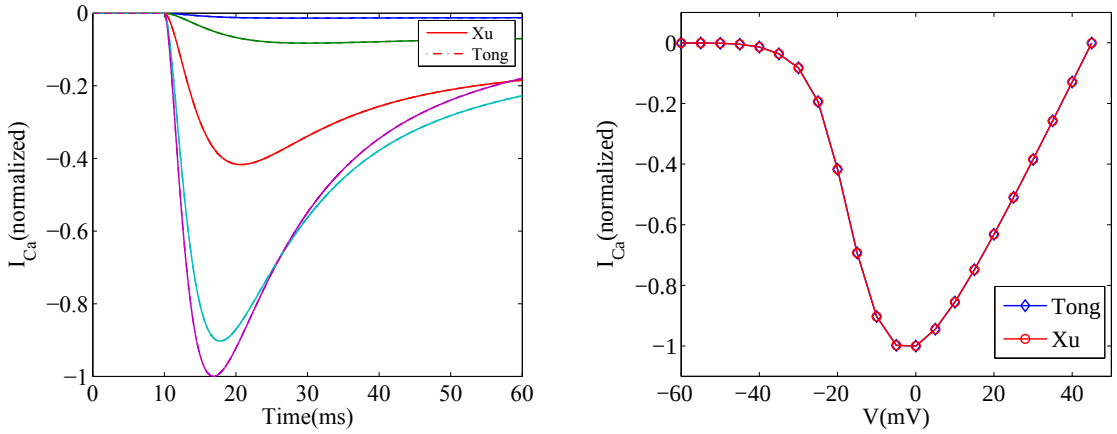

(a) (b)

Figure 2.13: Myometrial I_{CaL} model. (a) Simulated voltage-clamp I_{CaL} at voltage steps of -40 to 0 mV from a holding potential of -60 mV. (b) i–V relation of the peak currents. Data are normalized to the peak current at $V = 0$mV.

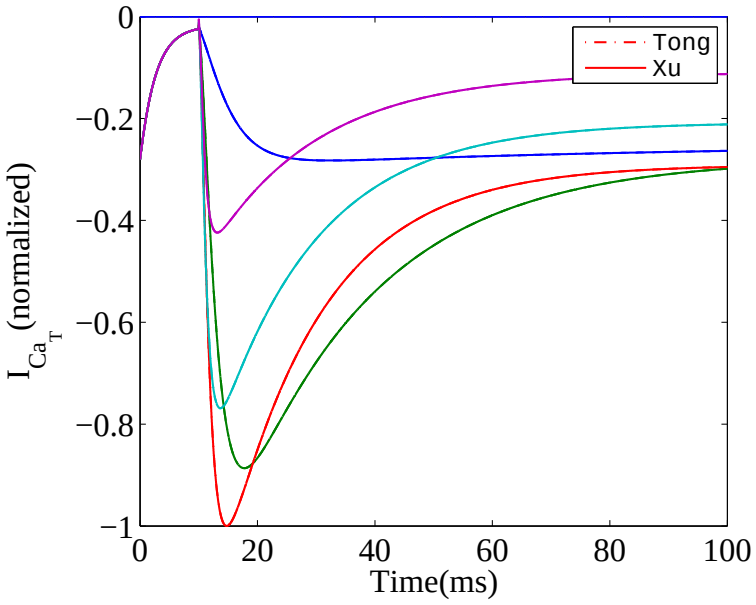

(a)

Figure 2.14: Myometrial I_{CaT} model. simulated I_{CaT} at voltage steps of -60 to 20mV from a V_h of -80 mV. Data are normalized to the peak current at $V = -25$mV.

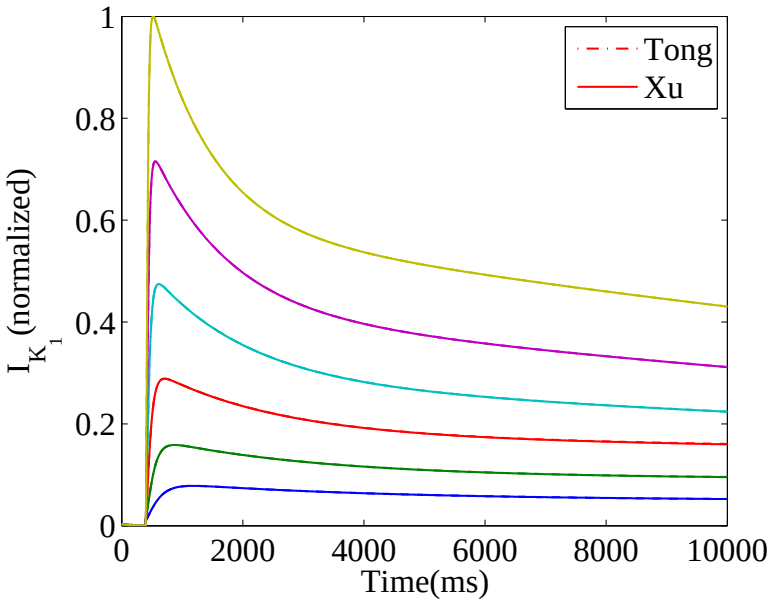

(a)

Figure 2.15: Myometrial I_{K_1} model. Simulated time tracings of I_{K_1} at voltage steps of -40 to 10 mV from a holding potential V_h =-80 mV. Data are normalized to the peak current at 10mV.

2.4 Single cell response under stimulus

Excitable uterine myocytes are capable of generating continuous activity when submitted to an external current of appropriate intensity [43].

Fig.2.18 shows different patterns of activity, predicted by the modified model of Rihana. For an intermediate value of the current, $I_{st} = 0.124\mu\text{A/cm}^2$, it generates a single action potential, and relaxes to its resting state (Fig.2.18a). Increasing the current larger than a critical value $I_c = 0.1360\mu\text{A/cm}^2$, repetitive spikes are obtained, with a period of about several minutes (Fig.2.18b). Further increase in the stimuli reduces oscillation period (Fig.2.18c). The changes of the oscillating periods versus the stimuli shows a logarithmic law (Fig.2.18d), indicating that a Homoclinic bifurcation takes place as the system passes from excitable regime to oscillating regime [110].

When an external current is applied, sustained activity can also be observed in the modified model of Tong, see Fig.2.19. The similarities between the results obtained with the modified Rihana and Tong model suggest that the results obtained in this thesis are robust, i.e., not finely dependent on the details of the model, or its implementation. In the rest of the manuscript, we restrict our discussion to the modified Tong model.

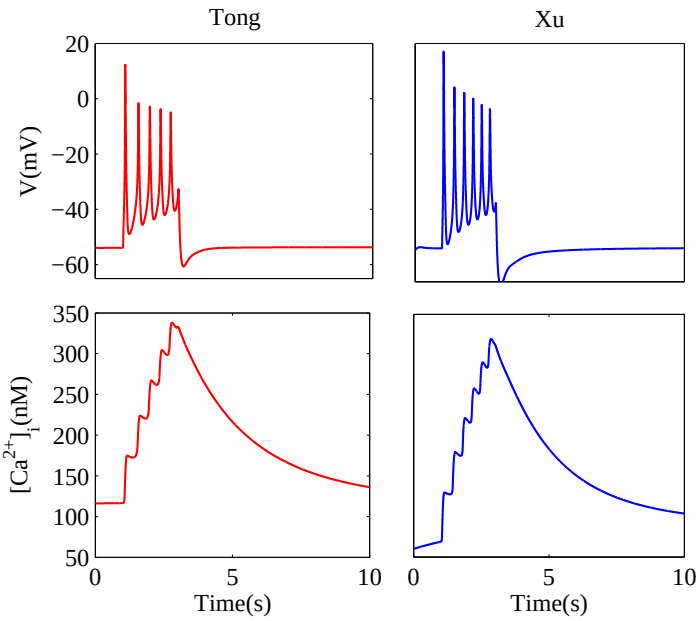

Figure 2.16: Action potentials ($V(t)$) during a 2s depolarizing current clamp $I_{st} = -0.5pA/pF$ under control conditions (Figure 12 in Tong's paper). Comparison between two codes (same parameters are used).

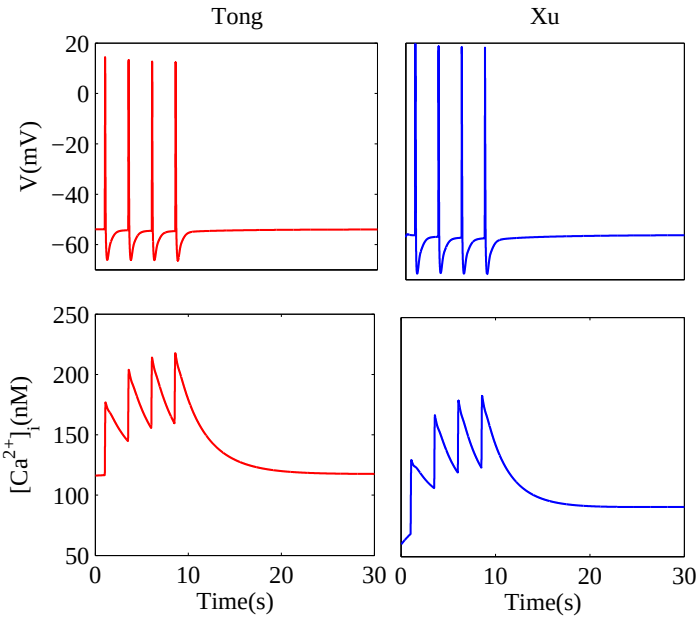

Figure 2.17: Reproducing Figure 13 in Tong's paper. Simulation of the simultaneous recordings of myometrial V_m . Four consecutive single spike APs modeled by -1.5pA/pF of 20ms, applied at 0.4Hz.

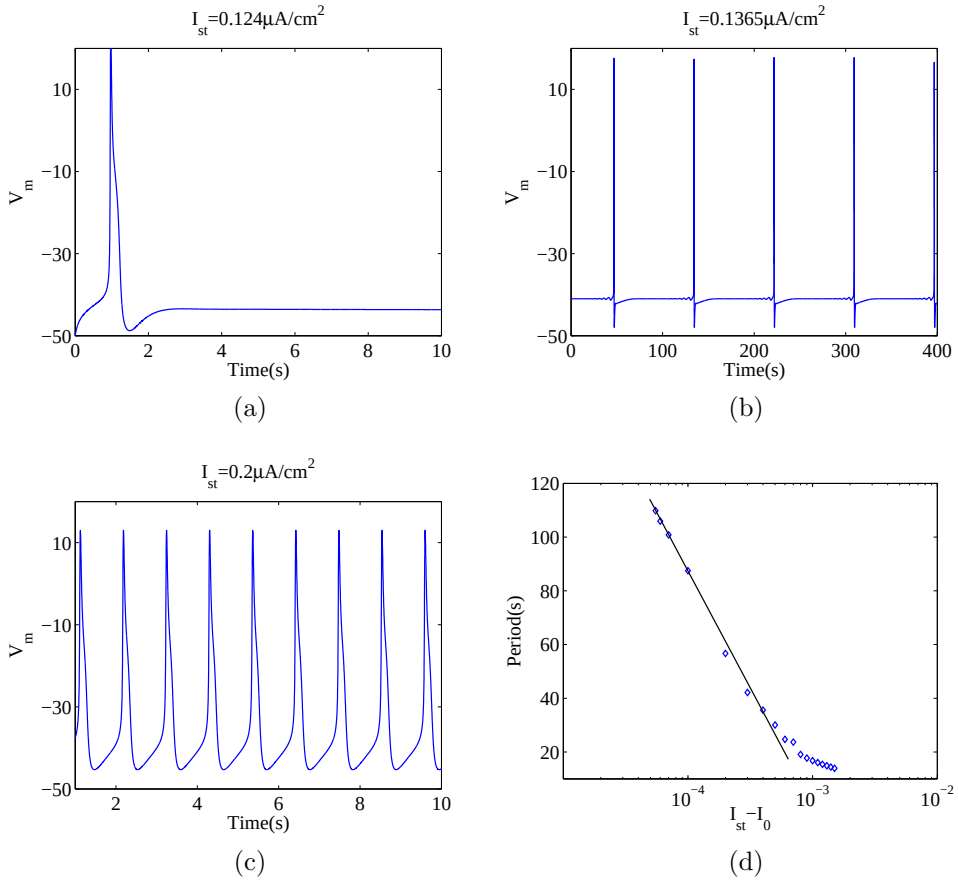

Figure 2.18: Modified Rihana's model: different uterine electrical activities under stimulus currents and oscillation periods. (a): Single action potential induced by a constant current of 0.124 μA/cm^2. (b), (c): repetitive action potentials simulated in response to a current larger than a threshold value I_c. (d): logarithmic changes of period with the increase of stimulus currents indicates a homoclinic bifurcation. $I_0 = 0.1364\mu$ A/cm^2

2.5 FHN as a simplified myocyte model

Excitability describes the influence of external changes to the system behavior: the system only responds to strong perturbations, while it is not affected by small perturbations. This all-or-none property is of crucial importance in brain functioning [111, 112], regulating the propagation and integration of synaptic signals. In a neuron or a smooth muscle cell, the excitability is manipulated by the number and properties of voltage gated ion channels [73, 11, 44], which involves high dimensional non-linearity. Here we will show that the FitzHugh-Nagumo model, which contains only two variables, a fast and a slow one, captures the main features of the excitability. In fact, this modeling of excitable media by the interaction of a fast and a slow

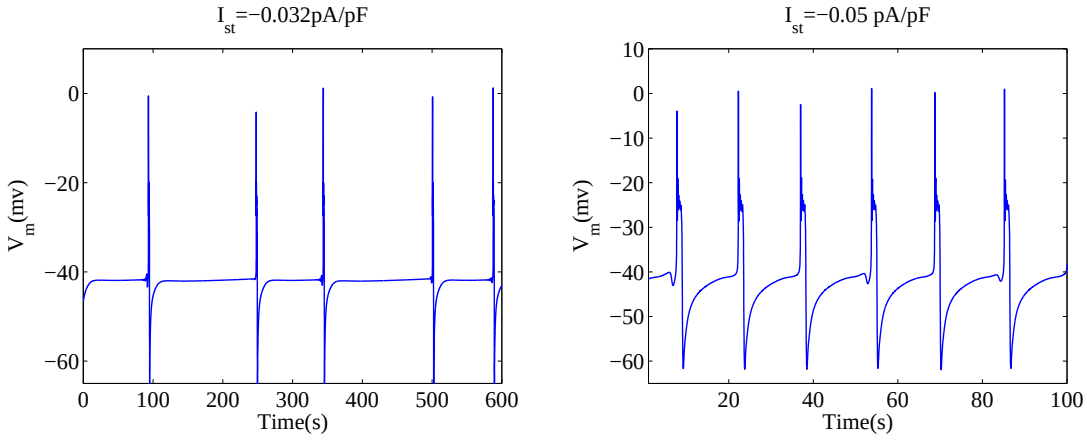

(a) (b)

Figure 2.19: Repetitive action potentials under constant stimulus currents observed in the modified Tong's model.

variable has been very successful. Many other models have been proposed, such as Hindmarsh-Rose model [113], Oregonator [114], *etc.* The Hindmarsh-Rose model, developed in 1984 by J. L. Hindmarsh and R. M. Rose, allows for bursting, which provides a very realistic description of the rapid firing of the neurons compared to the relatively long interval between firing, and for this reason, it is frequently used in the study of neuron science. The Oregonator model is the simplest realistic model describing the chemical oscillations, and is mostly used in the study of chemistry.

2.5.1 Description of FHN model

The FitzHugh-Nagumo model (FHN) is a generic model for excitable cell and can be applied to a variety of systems, in the biological sciences, including neuroscience [115, 116] and the study of the heart [54, 55], but also in chemistry [117]. It was first introduced by FitzHugh in 1961 [9] as a simplification of the Hodgkin-Huxley equations. Using the fact that n and h have slow kinetics compared to m, and that $n+h$ is approximately equal to 0.8, the original Hodgkin-Huxley model (Equ. (2.2)), can be reduced to a two variables system [118]:

$$\begin{aligned} C\frac{\mathrm{d}V}{\mathrm{d}t} =& -g_K n^4(V-E_K) - g_{Na} m_\infty^3(V)(0.8-n)(V-E_{Na}) - g(V-E_l) + I_{st} \\ \frac{\mathrm{d}n}{\mathrm{d}t} =& \frac{n_\infty - n}{\tau(V)} \end{aligned} \tag{2.31}$$

The simplified description of the electrical impulse in a cell is amenable to a geometric representation, in the form of a phase space description [87]. Noticing that the V-

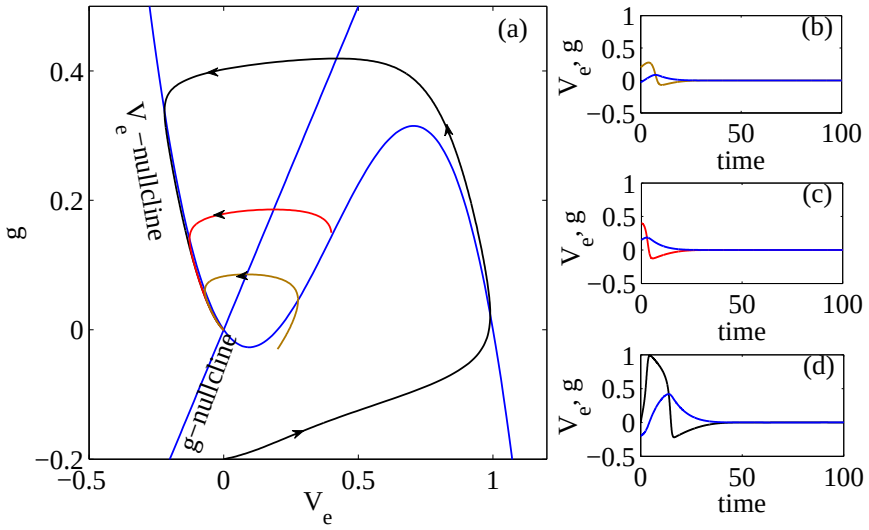

Figure 2.20: Phase portrait and its kinetics of the FitzHugh-Nagumo model at $I_{st} = 0$. The system returns to its stable fixed point directly when small perturbations are introduced (gray and red curve in (a)). Their corresponding time variations are shown in (b) and (c). A large enough perturbation from the fixed point leads to an action potential before it returns to its fixed point (d).

nullcline, obtained from the condition $\dot{V} = 0$, has a cubic shape, while n-nullcline is approximately a straight line, FitzHugh suggested a polynomial model as

$$\begin{aligned} \frac{\mathrm{d}V_e}{\mathrm{d}t} &= F(V_e, g) = AV_e(1 - V_e)(V_e - \alpha) - g + I_{\text{est}} \\ \frac{\mathrm{d}g}{\mathrm{d}t} &= G(V_e, g) = \epsilon(V_e - g) \end{aligned} \tag{2.32}$$

In this simple model, the variable V_e represents the membrane potential, and g represents the re-polarizing current. The parameter α is the excitation threshold, A represents the characteristic rate of activation, and ϵ the recovery rate of the medium – note that ϵ is much smaller than A, so that activation is fast, and recovery is slow.

Despite the fact that the model can be deduced, to some extend, from the original Hodgkin-Huxley equations, it is not able to reproduce many quatitative features of the propagation of electricity in neurons and muscles. Still, it correctly reproduces the existence of a threshold of excitation, as well as the existence of a recovery period. As a result, an external current can elicit an action potential. In 1964, Nagumo devised a circuit using tunnel diodes for the nonlinear element. Hence, Equ. 2.32 became the famous FitzHugh–Nagumo model (FHN).

Without any loss of generality, in the study here, we restrict ourselves to the set of parameters α =0.2, $A = 3.0$ and ϵ=0.08 (Eq. (2.32)). As shown in Fig.2.20, in the absence of any current, $I_{\text{est}} = 0$, the V_e-nullcline intersects the g-nullcline at (0,0), so

that (0,0) is the only fixed point of the system. We observe that the system returns to the fixed point when a small perturbation is applied (panel b and c). On the contrary, when a large perturbation is applied, the solution is observed to vary by a large amount before returning to the fixed point, see panel d.

2.5.2 Stability analysis

Much insight can be obtained by performing a linear stability analysis of the system in the vicinity of the fixed point when an external stimulus is applied. The analysis consists in linearizing Eq.(2.32) around the only fixed point (V_e^0, g^0), that is, in considering a small perturbation $(\delta V_e, \delta g)$ around the fixed point $(V_e, g) = (V_e^0, g^0)$, and by writing $F(V_e^0 + \delta V_e, g^0 + \delta g) \approx \partial F/\partial V_e(V_e^0, g^0)\delta V_e + \partial F/\partial g(V_e^0, g^0)\delta g$ and $G(V_e + \delta V_e, g + \delta g) \approx \partial G/\partial V_e(V_e^0, g^0)\delta V_e + \partial G/\partial g(V_e^0, g^0)\delta g$ which results in the system:

$$\begin{pmatrix} \delta\dot{V}_e \\ \dot{\delta g} \end{pmatrix} = \begin{pmatrix} \frac{\partial F}{\partial V_e} & \frac{\partial F}{\partial g} \\ \frac{\partial G}{\partial V_e} & \frac{\partial G}{\partial g} \end{pmatrix} \begin{pmatrix} \delta V_e \\ \delta g \end{pmatrix} = \mathbf{M} \begin{pmatrix} \delta V_e \\ \delta g \end{pmatrix} \tag{2.33}$$

which defines the Jacobi matrix $\mathbf{M}$. The time evolution is determined by the eigenvalues λ of $\mathbf{M}$, which are found to be:

$$\lambda_{1,2} = \frac{T \pm \sqrt{T^2 - 4\Delta}}{2} \tag{2.34}$$

where Δ and T are the determinant and trace of the matrix $\mathbf{M}$. For this set of parameters, the two eigenvalues λ_1 and λ_2 are conjugated. As the real part of the

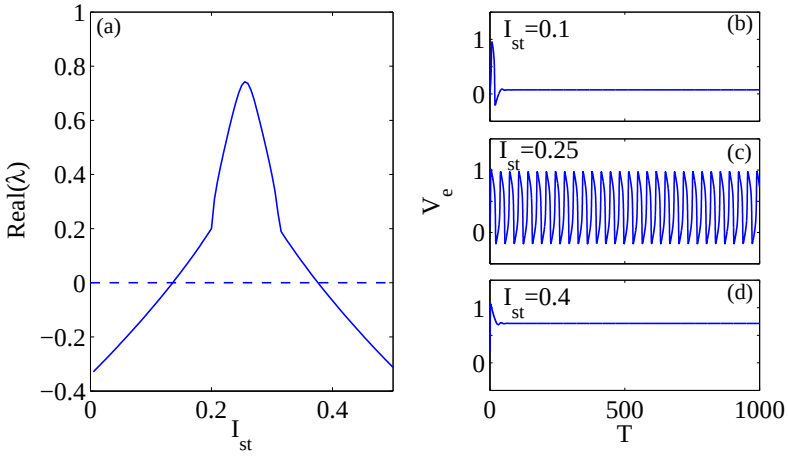

Figure 2.21: (a) Changes of the real part of the eigenvalues λ_1 and λ_2 as I_{st} increase. Oscillations are observed when $real(\lambda)$ is positive . (b)∼(d), System dynamics under different I_{st}.

two eigenvalues passes from negative to positive values, the stable fixed point loses its stability, hence oscillations appear. Fig.2.21 shows the relations between $real(\lambda)$ and the system behavior. We see that oscillations are only observed when the eigenvalues have a positive real part. A more detailed analysis can be found in Ref. [119, 120].

2.6 Conclusion

In this chapter, we first established two realistic models of the uterine myocyte. The first model, based on the work of Rihana *et al.* [43], deals with 5 ion channels. The second model is based on the work of Tong *et al.* [44], which contains detailed descriptions of 14 different currents. With minor corrections on the Na^+–Ca^{2+} exchanger, although quantitative differences are found between these two models, they behave qualitatively the same, both well manifesting properties of excitability.

The excitability is one of the main characteristics of the uterine smooth muscle cells—the myocytes. To well describe it, Rihana's model takes 11 variables (differential equations needed to describe whole cell electrical activities), and 24 variables in Tong's model. While a FHN model, which only contains two variables, is sufficient to capture this property. This simplicity allows us to study the uterine activities at the organ level, which usually involves millions of uterine cells.

Chapter 3

Coupling induced oscillations in Uterus

As mentioned in the introduction, aside from the smooth muscle cells which are physically excitable, being able to generate action potentials under proper stimuli, there are passive cells in the uterus. In this chapter, we will see that the interaction between these two cell types can give rise to spontaneous oscillations.

3.1 Description of passive cells

The dynamics of the membrane potential V_p of such passive cell can be well described by the equation [121]:

$$C_p \frac{\mathrm{d}V_p}{\mathrm{d}t} = -G_p(V_p - V_p^r) \tag{3.1}$$

Here V_p^r stands for the equilibrium potential. C_p and G_p are the membrane capacitance and the conductance. Contrary to the case of excitable cell, the membrane potential V_p always relaxes exponentially to its resting state,$V_p \to V_p^r$ when $t \to \infty$.

A fibroblast is a passive cell. In fact, Eq.(3.1) was first introduced by Kohl *et al.* to describe the fibroblasts in the sino–atrial node region of rat heart [121]. In the uterus, the population of fibroblasts is small [27], but it plays an important role in remodelling the human uterine cervix during pregnancy and parturition [122, 123]. The size of fibroblasts is also small: their shape is approximately spherical, with a diameter of $\sim 8\mu$m [124]. The very small size of the fibroblast results in individual cells having a capacitance of only about $4 - 6$pF [125, 124], which is much less than those of myocytes or ICLCs (85pF [27]). Their resting potential, V_F^r, varies over a large range, from -70 to 0 mV, but mostly in the range -25mV $\leq V_F^r \leq$ 0mV (in $\sim 75\%$ of all cases), with a peak of the distribution at -15mV [126]. We describe the dynamics of the fibroblast membrane potential, V_F, by Eq. (3.1), with a membrane conductance $G_F = 1nS$ [121], and $V_F^r = -15$mV.

ICLC are also passive cells. Duquette *et al.* [27] demonstrated that uterine ICLCs

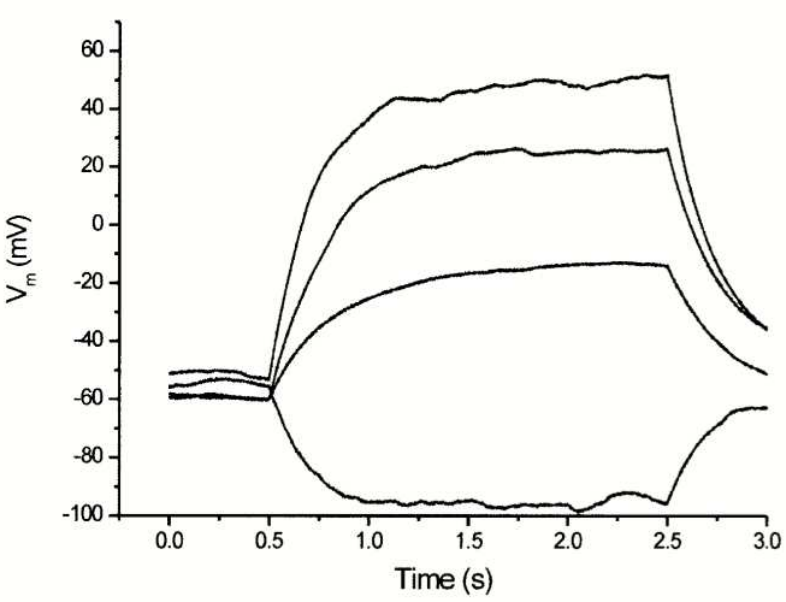

Figure 3.1: Membrane potentials recorded from a ICLC in response to a hyperpolarizing and three progressively increasing depolarizing current pulses. Only passive electronic potentials, but not active responses, were recorded from this cell, indicating its inability to generate action potentials (replotted from Ref.[27]).

did not exhibit spontaneous depolarizations. Experimental investigations led to the conclusion that there are no inward currents in ICLCs, therefore excluding the possibility to generate action potentials [27]. In addition, by applying an external current, it was found that the membrane potential of the cell relaxes essentially exponentially, with a characteristic time of the order of $0.2 \sim 1s$, see Fig.3.1. This suggests that the dynamics of the membrane potential of ICLCs can also be well described by Eq. (3.1). The capacitance of the ICLC is found to be $C_I \sim 84.8 \pm 18.1$ pF, and the input resistance to be $G_I \sim 3.04 \pm 0.50$ GΩ, close to the values of the myocytes. The resting potential V_I^r is found to be $V_I^r \sim -58 \pm 7$ mV, that is, ~ 10 mV higher than the membrane potential of the myocytes. Note that the variation of the relaxation time suggested by Fig.3.1, could result from a dependence of G_I in the membrane potential. Although Eq. 3.1 is a simplification, it is expected to capture the main aspects of the dynamics.

3.2 Coupling induced pacemaker activity in FHN model

Pacemaker activity (spontaneous oscillation) can exist in the mixed medias of excitable and passive elements [54, 55]. The uterus contains excitable cells (myocytes) and passive cells (fibroblasts and ICLCs). It is promising that the interaction be-

tween myocytes and ICLCs or/and fibroblasts could give rise to pacemaker activities in uterus. We study here the interaction between an myocyte, described by the FHN model which captures many electrical properties of myocytes, and an electrically passive cell, whose membrane potential obeys [121]:

$$\frac{\mathrm{d}V_p}{\mathrm{d}t} = K(V_p - V_p^r) \tag{3.2}$$

Here V_p^r and K indicate the resting potential and the inverse of the time scale (product of membrane resistance and capacity: $K^{-1} = C_p/G_p$) of the passive cell, respectively. Taking into account the fact that fibroblasts or ICLC have a higher resting potential, and typically a smaller capacitance than myocytes [124, 125], we take here $V_p^r = 1.5$ and $K = 0.25$. This choice is made without any particular attempt to reproduce finely the results of the realistic physiological model; we are mostly interested here in some qualitative understanding of the system.

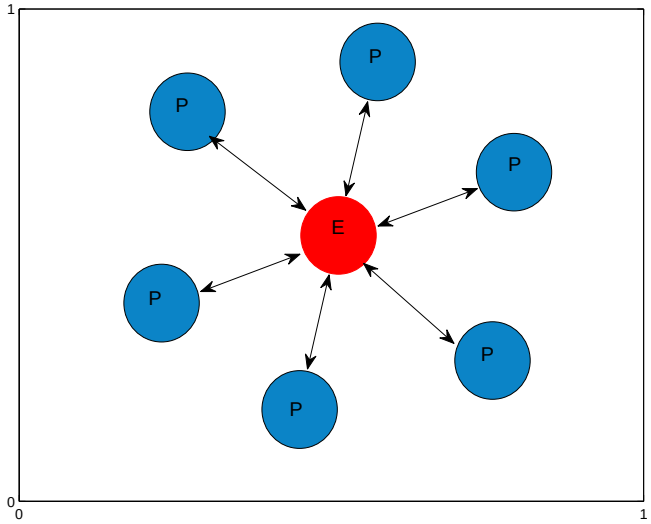

Figure 3.2: Schematic illustration of the coupled FHN system. Excitable element (E) is surrounded by n_p identical passive elements(P). Interactions (arrows) only exist between Excitable and Passive elements.

We are asking here what is the evolution of a cell pair, consisting of one myocyte, coupled to a passive cell. The problem has been studied by Jacquemet [54], and our approach follows his original analysis. The precise problem that we have in mind can be simply modeled by Fig.3.2: one myocyte cell (Fig.3.2) is coupled to n_p identical passive cells described by Eq. 3.2 ($n_p = 6$ in Fig. 3.2). In the case where all the values

of V_p are identical for all the passive cells, the equations for the system simply read:

$$\frac{\mathrm{d}V_e}{\mathrm{d}t} = AV_e(1-V_e)(V_e-\alpha) - g + n_p C_r(V_p - V_e) \tag{3.3a}$$

$$\frac{\mathrm{d}g}{\mathrm{d}t} = \epsilon(V_e - g) \tag{3.3b}$$

$$\frac{\mathrm{d}V_p}{\mathrm{d}t} = K(V_p^r - V_p) + C_r(V_e - V_p) \tag{3.3c}$$

where C_r is coupling strength between the two cell types, and n_p indicates the number of passive elements attached to the excitable one.

The reason why the system Eq.(3.3) can lead to oscillations can be traced back to the difference in the resting potentials of the cells. The coupling C_r leads to a depolarizing current for the myocyte, which under proper conditions can be large enough to lead to an oscillatory state. In the following, we refer to the system Eq.(3.3) as the 0-dimensional (0-D) model, as this set of equations is simply for one myocyte, independent of any spatial effect. This case can be also thought of as a mean field limit, where the coupling between myocytes is so strong that only the averaged number of passive cells coupled to the myocyte, $f = \langle n_p \rangle$ plays a role, and the local spatial fluctuations can be ignored. Note that in general, the averaged number f needs not be an integer number. For this reason, we replaced n_p by f, and have investigated the properties of the system Eq.3.3 for an arbitrary value of f and C_r.

The dynamical properties of the system Equ.(3.3) can be discussed by carrying out the linear stability analysis, as discussed in 2.5.2. The Jacobi matrix around a fixed point (V_e^0, g^0, V_p^0) is:

$$\mathbf{M} = \begin{pmatrix} 3AV_e^{0\,2} + 2A(1-\alpha)V_e^0 - (A\alpha + n_p C_r) & -1 & fC_r \\ \epsilon & -\epsilon & 0 \\ C_r & 0 & -(K + C_r) \end{pmatrix} \tag{3.4}$$

where it is understood that (V_e^0, g^0, V_p^0) is a fixed point of the system. The analysis of the eigenvalues of the matrix $\mathbf{M}$ shows that at a given coupling strength, C_r, when the value of f exceeds a critical value, f_c^1, the system bifurcates from excitable to oscillatory. We also observe that when f exceeds another threshold f_c^2, the system becomes again non-oscillatory. A detailed study in the (C_r, f) parameter space leads to the identification of the region where the system oscillates, as shown in orange in Fig. 3.3. One observes that at a given value of f, larger than a critical value, oscillations are found by increasing the coupling strength C_r. Our numerical work suggests a linear relation between f and $1/C_r$. In fact, in the case of a relatively rapid relaxation of the passive cell, that is, for a large enough value of the parameter K in Eq.3.2 or 3.3c, we may assume that the relaxation of V_p to its equilibrium value is very fast, given the value of the myocyte membrane potential V_e: V_p is obtained by solving $\mathrm{d}V_p/\mathrm{d}t = 0$. This substitution leads to the addition to the right hand side of Eq.3.3a, of a term equal to $f/(1 + K/C_r)(V_p^r - V_e)$. This implies that at a fixed value

of V_p^r, the behavior of the system can be understood as a function of the parameter I_{est}, which in turn implies that the threshold values $f_c^{1,2}$ behave as $A + B/C_r$. This is completely consistent with our numerical findings, see the insets of Fig.3.3.

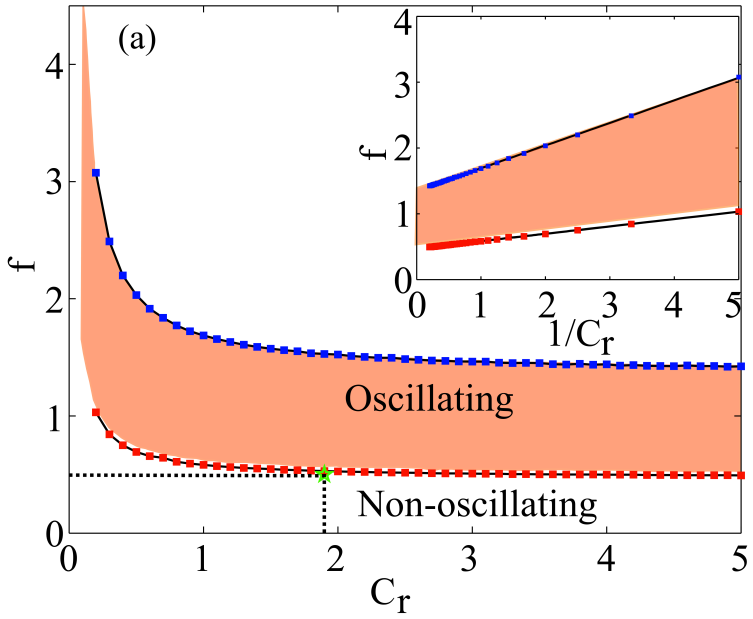

Figure 3.3: The 0-d system has oscillating solutions in the yellow region when the passive cell fraction f is in the range $[f_c^1 f_c^2]$. These two values can be obtained by linear stability analysis (red coloring) or numerical integration (dots).

The dynamical properties of the system Eq. 3.3 in the (C_r, f) plane can also be investigated by direct numerical integration. We solved Eq.3.3 using a fourth-order Runge-Kutta scheme, implemented in C, with a time step $dt = 0.05$. The initial condition was chosen to be random. The results, concerning the state (oscillatory, excitable) of the system are shown in Fig. 3.3. The filled symbols show the points where a transition between oscillatory and excitable is observed. These transitions can be directly compared to the stability analysis presented above. We find an extremely good agreement between the results of the direct integration and the stability analysis concerning the values of f_c^2.

On the other hand, discrepancies are found for the other boundary, f_c^1. This difference between the two bifurcations is a result of the difference in the natures of the transitions. Oscillations appear, close to f_c^1, with a finite amplitude. This is a result of the subcritical nature of the corresponding bifurcation [120]. As a result, oscillations persist for values of f smaller than f_c^1. An example, at $C_r = 1.9$ is given in Fig.3.4. Panel (a) and (b) show the amplitude Am, defined as the difference between the maximum and minimum values of variable V_e, and frequency of oscillation, respectively. Numerical integrations give a critical value of $f^0 = 0.529$, whereas numerical stability analysis leads to $f_c^1 = 0.545$. Panel (c) provides details of the region

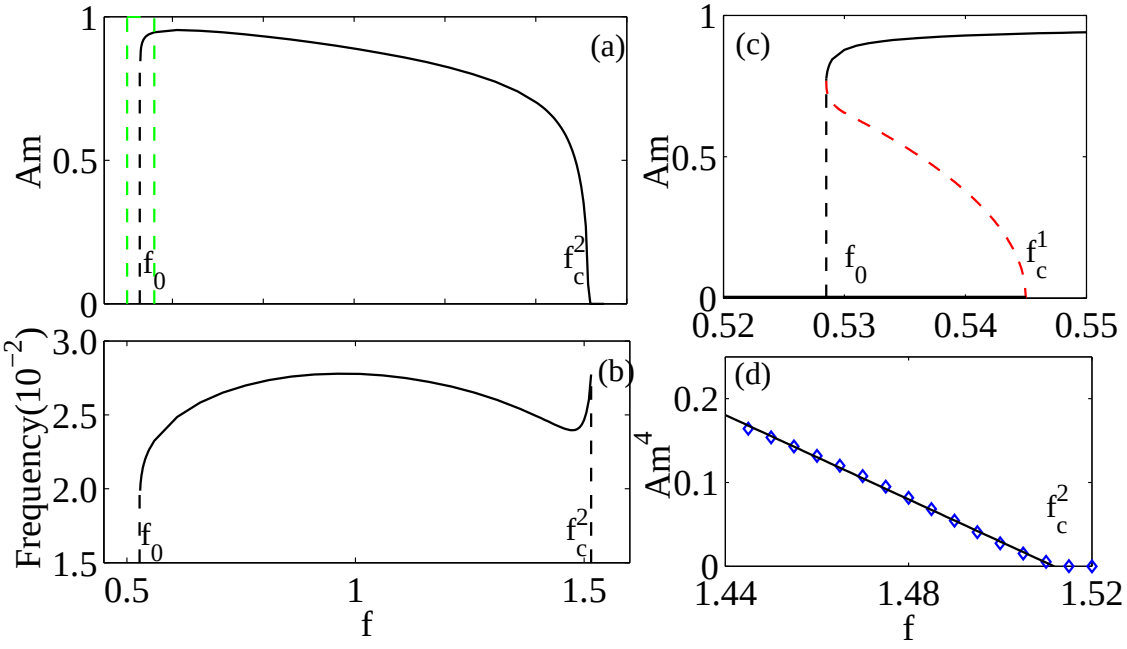

Figure 3.4: Coupled cell-pair dynamics at $C_r = 1.9$ and varying f. (a), (b) variations of oscillating amplitude and frequency at different f. (c) Between $f_0 = 0.529$ and $f_c^1 = 0.545$, one observes bistability; the red dotted line is a schematic drawing of the unstable branch. (d) Close to f_c^2 oscillations vanish like $A_m \propto (f_c^2 - f)^{1/4}$.

of values of f where one sees that the system has two attracting basins for values of f such that $f_0 \leq f \leq f_c^1$. The branch with a high value of the amplitude corresponds to an oscillating solution, whereas red dashed curves schematically shows the un-stable oscillating branch, where the system eventually relaxes to its fixed point.

The existence of a multiplicity of basins of attraction even in the simplest 0-D problem, may seem at first sight as a curiosity. We merely notice here that this multi-stability has implications for the study of the transition in 2-dimensional systems, to be discussed in Chapter 4

In comparison, we noticed that the conjugated eigenvalues of the Jacobian Matrix at the fixed points have zero real parts at the bifurcation point. This suggests the bifurcation from oscillatory to non-oscillatory behavior close to $f = f_c^2$ occurs to via regular Hopf bifurcation. While surprisingly, the amplitude A_m vanishes like $A_m \propto (f_c^2 - f)^{1/4}$, rather than $A_m \propto (f_c^2 - f)^{1/2}$ (see panel d).

In summary, our numerical solutions allow us to determine the dependence of the

values f_0, f_c^1 and f_c^2 as a function of C_r:

$$f_0 = \frac{0.112}{C_r} + 0.471 \tag{3.5a}$$

$$f_c^1 = \frac{0.117}{C_r} + 0.484 \tag{3.5b}$$

$$f_c^2 = \frac{0.343}{C_r} + 1.349 \tag{3.5c}$$

With these equations, an estimation of a coupled cell-pair dynamics can be obtained at a given f and C_r.

3.3 Coupling induced pacemaker activity in realistic model

We have seen in the previous section that coupling between myocyte, modeled by the generic FHN model, and the passive cells provides a way to sustained oscillations in the uterus. Together with similar works [54, 127, 55, 128], we hypothesized that the spontaneous action potentials are initiated by the coupling between passive cells and myocytes. Indeed, as stated in the introduction, experiments have demonstrated the role of the intracellular coupling of uterine myocytes in the transition from weak and desynchronized contractions, to powerful synchronous contractions during labour [36, 37]. Furthermore, the disruption of the gap junctions by chemical means can inhibit the uterine contractions [51]. In the uterus, close contact between ICLCs and smooth muscle cells has been observed [27]. Although, up to now, no direct evidence shows the existence of electrical coupling between myocytes and fibroblasts via gap junctions, studies of cardiac tissues *in vitro* strongly suggest such a coupling [56, 129]. All these suggest us to carry out detailed studies on the role of gap junctional coupling in the uterus.

We begin with considering the role of the coupling between myocytes and passive cells. The gap junctions, composed of connexin proteins, provide channels of low electrical resistance between cells. Through these pores a current can flow from cell to cell when the cellular membrane potentials are different. To evaluate the influence of passive cells on the electrical behavior of the myocyte, we consider a biophysical model composed of a myocyte coupled to n_p passive elements, while no connections between passive cells (see Fig. 3.2). Taking into account the two types of passive cells (ICLCs and fibroblasts) in the uterus, the interactions between excitable and passive

cells via the gap junctions can be described by the following differential equations:

$$C_m \frac{\mathrm{d}V_m}{\mathrm{d}t} = -I_{ion} - n_I G(V_m - V_I) - n_F G(V_m - V_F) \tag{3.6a}$$

$$C_I \frac{\mathrm{d}V_I}{\mathrm{d}t} = -G_I(V_I - V_I^r) - G(V_I - V_m) \tag{3.6b}$$

$$C_F \frac{\mathrm{d}V_F}{\mathrm{d}t} = -G_F(V_F - V_F^r) - G(V_F - V_m) \tag{3.6c}$$

Here n_I and n_F indicate the number of ICLCs cells and fibroblasts attached to a myocyte; G is the gap junction conductance; G_I and G_F are the membrane conductance of ICLCs and fibroblasts respectively. The conductivity of a single gap junction channel is $\sim$ 50 pS[130], thus the increase of gap junction channel during pregnancy can be modeled by the parameter G, which describes the excitable–passive cell coupling strength. For simplicity, we assume all ICLCs and fibroblasts are identical, with resting potential of V_I^r and V_F^r respectively. With a gap junction channel, each passive cell (with V_p denoting its membrane potential) contributes a current $G(V_m - V_p)$ to the myocyte. Thus the parameters n_I and n_F count the number currents received of ICLCs and fibroblasts. While a passive cell is only coupled to a myocyte, the coupling current to the passive one is simply $G(V_p - V_m)$.

To understand the mechanisms of uterine contraction, we investigate the influence of different parameters on the system behaviors by varying: 1), the coupling strength G that mimics the development of gap junctions expressions between myocyte and passive cells; 2) the number of passive cells a myocyte coupled to which describes the changes of effective n_p as excitable–excitable coupling increases ; and 3), the passive resting potential V_p^r. We first consider a system composed of one myocyte and ICLCs and no fibroblasts. The membrane capacitance and conductance are set as C_m=80pF, G_I=1.0nS respectively. Considering the difference between V_m^r and V_I^r, as well as the large error bars of the experimented data, we set V_I^r=-40mV in the following simulations.

3.3.1 Role of G

In the presence of coupling, a myocyte generates spontaneous action potentials due to a coupling current from passive cells to the myocyte, resulted from the difference of membrane potentials. The most significant change during pregnancy is the increase of gap junctions. Increasing G gradually, the system passes from quiescent state to rhythmic activity.

To study this effect, in the simulations, we consider here a myocyte only coupled to one ICLC cell, *i.e.,* $n_p = n_I = 1$, and set $V_I^r = -40$mV. At small G, the myocyte membrane potential V_m eventually reaches a resting state close to V_m^r. By gradually increasing G to 0.18nS, the coupled system (Equ.3.6) gives rise to spontaneous action potentials after a long transient time ($\sim$10mins). A typical oscillating pattern close to the critical value is depicted in Fig.3.5(a). Further increase in G leads to a decrease of

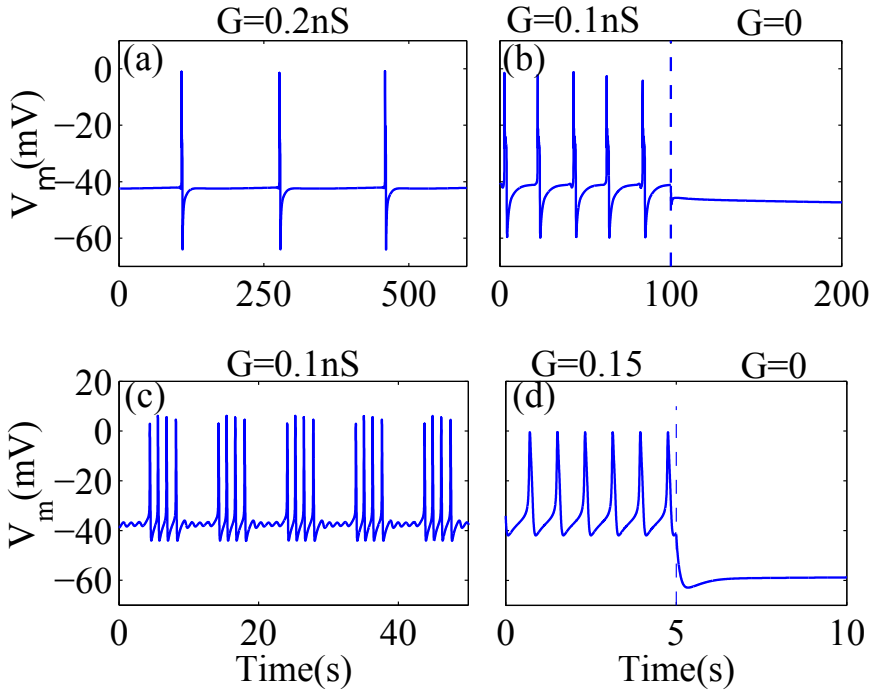

(a)

Figure 3.5: Myocyte-ICLC cell pair behavior of the two models under different coupling strength. (a-b), modified Tong's model with $g_{\mathrm{Na}} = 0.03$nS/pF. (a) Long period ($\sim$ 5min) spikes at G=0.2nS. (b), plateau-type action potentials at G=0.5nS. Breaking down the gap junctions ($G = 0$, after the dashed line) terminates the oscillations. (c-d) Similar behaviors in the modified Rihana's model with $V_f^r = -20mV$. (c) Bursting at $G = 0.1nS$. (d) regular spiking is observed at G=0.15nS, while no oscillations after setting $G = 0$.

the oscillation periods (panel b). Same as observed in mammalian uteri [51], breaking down the gap junctions immediately terminates the spontaneous generation of action potentials (panel b).

We noticed that when G is close to threshold value $G_o = 0.1778$ nS, the amplitude of the oscillation remains the same, while the oscillation period T_{osc} diverges logarithmically as $T_{osc} \sim \ln(G - G_o)$, as shown in Fig. 3.6. This strongly suggests that the transition to an oscillatory state occurs via a homoclinic bifurcation [131, 132].

Interestingly, we noticed that qualitatively similar behaviors could be observed using the modified Rihana's model. As shown in Fig.2.18 and Fig.3.5(c-d), repetitive action potentials are generated when a proper external stimulus current is applied as well as in the case of coupling with a passive cell. As both the models capture the essential properties of the cells' electrical behavior, we restrict our discussion to the modified Tong's model presented in Chapter 2. To capture the changes of the sodium conductance during pregnancy, we increase g_{Na} to 0.04nS, which corresponds to late

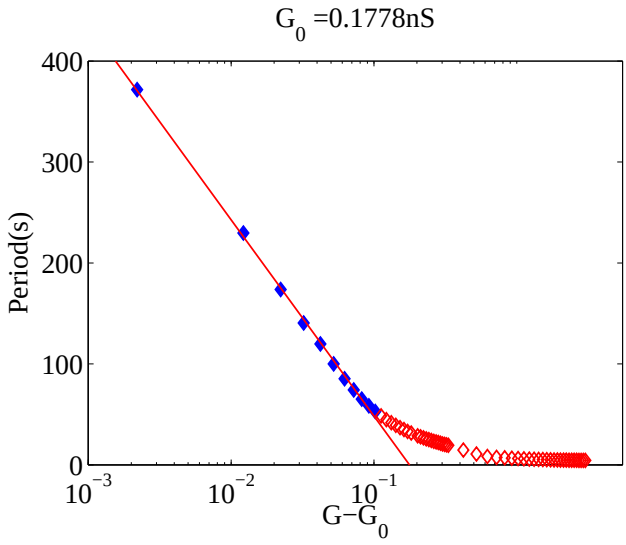

Figure 3.6: The oscillation period T_{osc} diverges logarithmically: $T_{osc} \sim \ln(G - G_c)$. Parameters: $n_p = n_I = 1$, $V_p^r = -40mV$.

pregnancy.

3.3.2 Role of V_p^r

As mentioned already, the coupling current $I_s = G(V_p - V_m)$ is due to the the difference in membrane potential between adjacent cells. The membrane potential V_p

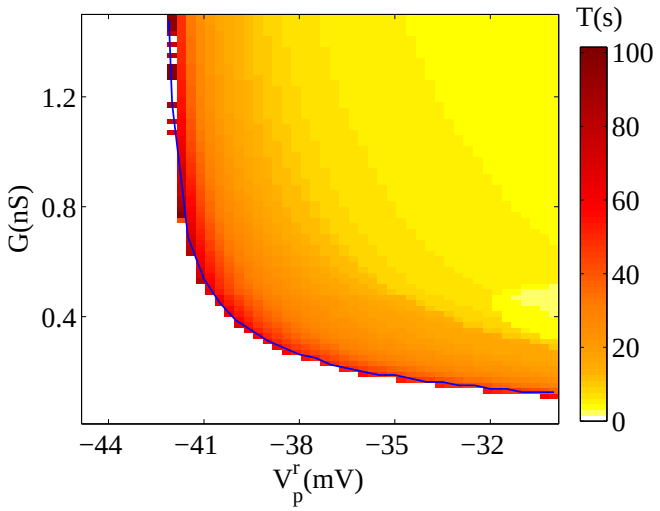

Figure 3.7: Influence of passive cell resting potential on the cell-pair behavior. The color code indicates the oscillating period(s). Parameter: $n_p = 1$.

of the passive cells, is higher when the resting potential V_p^r is higher. Increasing the resting potential of the passive cell V_p^r makes it possible to push the myocyte membrane potential above the excitation threshold, thus making it possible for the pair to oscillate, provided the coupling is strong enough.

Fig. 3.7 shows the domain in the (G,V_p^r) plane, where oscillations in the pair made of a myocyte and a passive cell ($n_p = n_I = 1$). Oscillations are observed only for a restricted set of parameters. When the value of V_p^r is very small, the coupling with an ICLC never results in the appearance of spontaneous oscillations. This can be understood by noting that when V_p^r is close to the resting membrane potential of the myocyte, the coupling term leads only to a small modification of the membrane potential of the cell. Provided the membrane potential of the myocyte is below some excitation threshold, no oscillation is observed.

3.3.3 Role of n_p

Anatomical studies of the uterus reveal that passive cells are distributed unevenly [31]. This implies that each myocyte can be connected to a varying number of passive cells (0, 1, 2 or more). This uneven character is counterbalanced by the coupling between myocytes. This coupling is known to increase as pregnancy progresses, especially close to the term. As a result of this coupling, the passive cells are "shared" by more than one myocyte. The effective number of ICLCs coupled to a myocyte becomes non-integer.

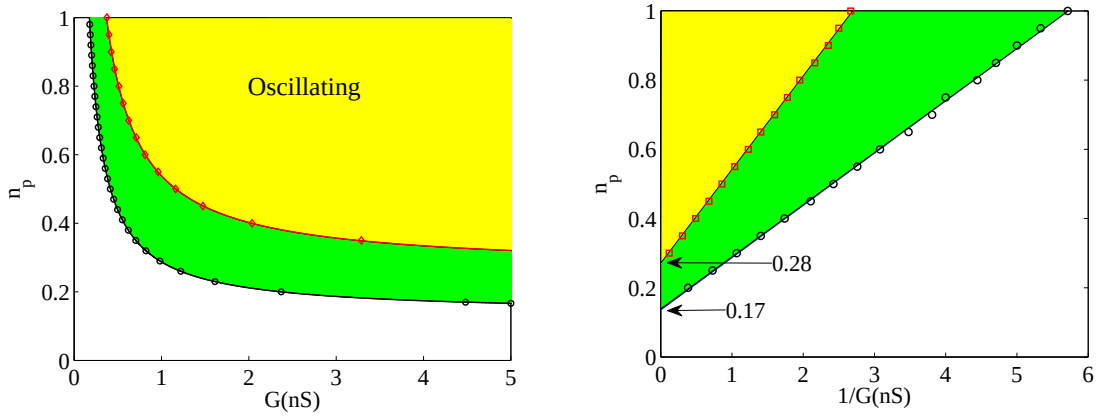

(a) (b)

Figure 3.8: Oscillating regions in (n_p, G) parameter space with/without (blue/yellow) the consideration of fibroblasts influence.

For this reason, we ask now in the plane (G, n_p) where do oscillations appear. Fig. 3.8 shows the result, for a value of the passive cell resting potential set to $V_p^r = -40$ mV. We observe that when the number of passive cells increases, the value of the

coupling necessary to see oscillations decreases. This can be qualitatively understood by noting that the depolarizing current is proportional to the product $n \times G$. Thus, the limiting value of n_p for the threshold of oscillation can be written as $n_p = A/G+B$, as shown in the right panel of Fig. 3.8.

From Fig. 3.8, we see that the oscillations can be observed only if there are at the minimum a fraction of 22%=$(n_p/(1+n_p)$)of passive cells in the uterus. However, we know that ICLC account only for $18 \pm 2\%$ of the total cell population [31], which is not enough to trigger oscillations in the system.

3.3.4 Combined effect of ICLC and fibroblasts.

We have seen in Sect. 3.3.2 that a myocyte generates spontaneous action potentials due to the membrane potential difference that triggers a coupling current from passive cells to the myocyte. The higher V_p^r is, the easier it generates oscillations. Unfortunately, ICLCs have a low resting potential close to that of myocyte and the population fraction in the uterine tissue is too small to generate oscillations.

Aside from ICLC, the uterine tissue also contains other kinds of passive cells. We pay particularly attention to the fibroblasts here, which have a small membrane capacitance, $C_F = 6$ pF, and a high resting potential $V_F^r = -15mV$. These cells play an important role in the development of the uterus during pregnancy [122, 123]. Their role in altering the electrical activities in cardiac tissue has been studied both numerically numerically [133] and experimentally [68]. However, no such study has been carried out in the case of the uterine tissue. We thus consider here the case that the fibroblasts are coupled to uterine myocyte through gap junctions. The fraction of fibroblasts among the non-muscular cells is relatively small; we set a relative fraction $n_F/n_p = 10\%$, where n_p is the sum of the number of ICLC n_I and of fibroblasts n_F.

Fig.3.9 shows the influence of fibroblasts in the triggering of oscillations. Comparing with the yellow region Fig.3.8 (in the absence of fibroblasts), the oscillating domain in the (G,n_p) plane is largely expanded. In particular, we find that the addition of a small number of fibroblasts allows to reduce the minimum fraction of passive cells necessary to see oscillations, from $n_p \approx 0.28$ to $n_p \approx 0.18$.

In this section, we have demonstrated that uterine contractions can be originated from the coupling between myocytes and the ICLCs. With structure modifications done to the Na^+-Ca^{2+} exchanger in the Tong's modell, a single myocyte is capable of generating spontaneous electrical activities when a stimulus current is applied. The coupling current acts a current and leads to the appearance of spontaneous activity. This coupling current increases when the coupling between myocytes and when passive cells n_p is increased.

We note that the electrophysiological changes during pregnancy, leading to an increase of G as well as g_{Na} tend to facilitate the appearance of a spontaneous electrical activity. However, the dependence of the results on the parameters provides constraints on the model. As stated above, the population of ICLC is not sufficient, if taken without the influence of other cells (fibroblasts).

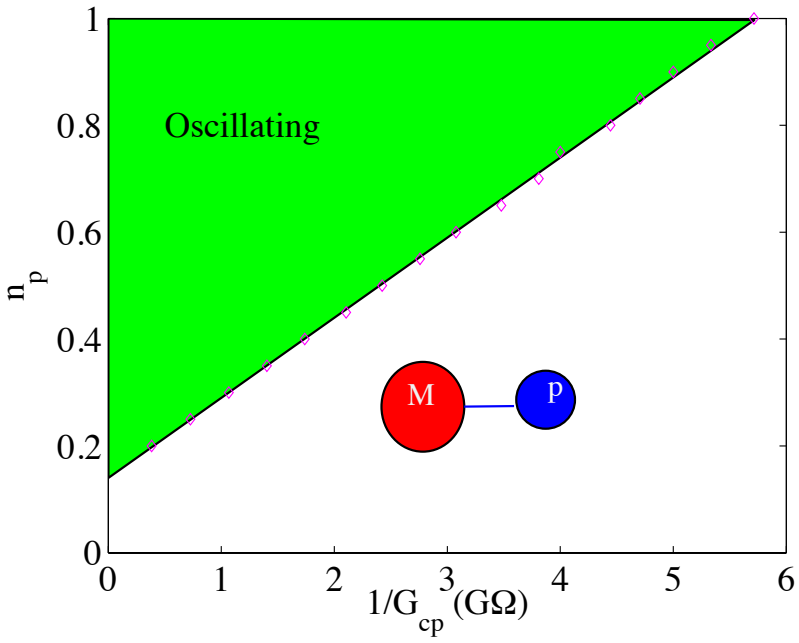

Figure 3.9: Influence of fibroblasts. By adding the small fraction(10%) of fibroblasts, global oscillations could be observed in the uterus. parameters: $C_f = 6.0$pF,G_f=1.0nS

Theoretical estimates

Myocytes are cells of size ∼212μm [33], typically much larger than ICLC (size ∼75μm [30] or fibroblasts (size ∼8μm [124]). As a consequence, the membrane capacitance of myocytes is much larger than the membrane capacitance of passive cells (C_m ∼120μm [27], C_I ∼85μm [27] and C_F ∼4.5μm [124]). On general grounds, the relaxation time of a cell is proportional to the cell capacitance, which leads to the expectation that the membrane potential in the small cells (fibroblasts, ICLC) evolves much faster than the membrane potential of the myocytes.

To document this effect, we computed the relaxation time in a system consisting of a myocyte, coupled to a fibroblast and an ICLC. We begin by considering the case where the deviation from the resting membrane potential of the myocytes is small, so the full equation can be linearized:

$$\frac{\mathrm{d}V_m}{\mathrm{d}t} = -\frac{1}{C_m}(G_m(V_m - V_m^r) + n_I\frac{GG_I}{G+G_I}(V_m - V_I^r) + n_F\frac{GG_F}{G+G_F}(V_m - V_F^r) \quad (3.7)$$

Together with Eq. 3.6b, 3.6c, the equations can be simply written as:

$$\frac{\mathrm{d}}{\mathrm{d}t}\begin{pmatrix} V_m \\ V_I \\ V_F \end{pmatrix} = \begin{pmatrix} -\frac{1}{C_m}(G_m + n_F G + n_I G) & \frac{n_F G}{C_m} & \frac{n_I G}{C_m} \\ \frac{G}{C_I} & -\frac{G_I+G}{C_I} & 0 \\ \frac{G}{C_F} & 0 & -\frac{G_F+G}{C_F} \end{pmatrix}\begin{pmatrix} V_m \\ V_I \\ V_F \end{pmatrix} + \begin{pmatrix} \frac{G_m}{C_m}V_m^r \\ \frac{G_I}{C_I}V_I^r \\ \frac{G_F}{C_F}V_F^r \end{pmatrix} \quad (3.8)$$

The solution of this set of equation can be written as a sum of three exponentially decaying solutions, of the form $\exp(-\lambda_i t)$, $i = 1, 2, 3$. The decay rates, λ_i are obtained by diagonalizing the 3×3 matrix in the right-hand side of Eq. 3.8. Fig. 3.10 shows the decay rates of the solutions, sorted in such a way that $\lambda_1 \geq \lambda_2 \geq \lambda_3$. The solutions have been determined numerically as a function of the coupling conductance, G. We have used here $C_m = 120$pF, $C_I = 80$pF and $C_F = 6.0$pF (shown with diamonds), $C_m = 60$pF, $C_I = 80.0$pF and $C_F = 6.0$pF (shown with left pointing triangles), and $C_m = 120$pF, $C_I = 40.0$pF and $C_F = 6.0$pF (shown with squares). The values of the conductances are $G_m = 0.33$nS, $G_I = 0.5$nS and $G_F = 1.0$nS. The three decay rates are widely different, being separated by one order of magnitude from each other. The highest decay rate, λ_1 depends neither on the capacitance of the myocyte nor on the capacitance of the ICLC, and can therefore be associated with the dynamics of the fibroblasts. Similarly, we find that by diminishing the capacitance C_I by a factor 2 leads to an increase of the intermediate decay rate λ_2 by a factor ~ 2. Same application done to C_m leads to an increase of λ_3 by the same factor. Therefore this demonstrates that λ_2 characterizes the relaxation associated with ICLC, and λ_3 the relaxation of the myocytes. In addition, we note that the eigenvector associated with λ_1 (respectivement λ_2, λ_3) has its largest component in the third (respectively second, first) direction, thus demonstrating that each of the three eigenvalues are indeed associated with the relaxation of the membrane potential in one of the three coupled cells, as shown in Fig.3.11

The main conclusion here is that the membrane potential of the myocytes has the slowest dynamics, by at least one order of magnitude compared to the dynamics of ICLC or fibroblasts. This feature suggests that the membrane potentials of the fibroblast, and to a lesser extend, of the ICLC relax very quickly towards the equilibrium value, consistent with the value of the myocyte. From a mathematical point of view, this suggests to eliminate the value of V_F and V_I, to reduce Eq. 3.6a, 3.6b, 3.6c to a single equation, where V_I and V_F are obtained by setting $\mathrm{d}V_I/\mathrm{d}t \approx \mathrm{d}V_F/\mathrm{d}t \approx 0$, *i.e.*, by solving $G_p(V_p - V_p^r) + G(V_p - V_m) = 0$ where $p = I$ (respectively F) for the ICLC (respectively fibroblasts). The resulting equation for V_m reads:

$$C_m \frac{\mathrm{d}V_m}{\mathrm{d}t} = -I_{ion}(V_m) - n_I \frac{GG_I}{G+G_I}(V_m - V_I^r) - n_F \frac{GG_F}{G+G_F}(V_m - V_F^r) \tag{3.9}$$

We consider first the case of a myocyte attached only to ICLC ($n_F = 0$, $n_I \neq 0$) so Eq. 3.9 reduces to:

$$C_m \frac{\mathrm{d}V_m}{\mathrm{d}t} = -I_{ion}(V_m) - n_I \frac{GG_I}{G+G_I}(V_m - V_I^r) \tag{3.10}$$

The electric coupling between the myocyte and the ICLC, G, and the number of ICLC coupled to the myocyte, n_I, enter Eq.3.10 through the parameter $\kappa_I \equiv \frac{GG_I}{G+G_I}$ only. As a result, oscillations appear in the system of coupled cells only when the parameter κ_I reaches some certain values. Noticing that, by definition, $n_I = \kappa_I \frac{G+G_I}{GG_I} =$

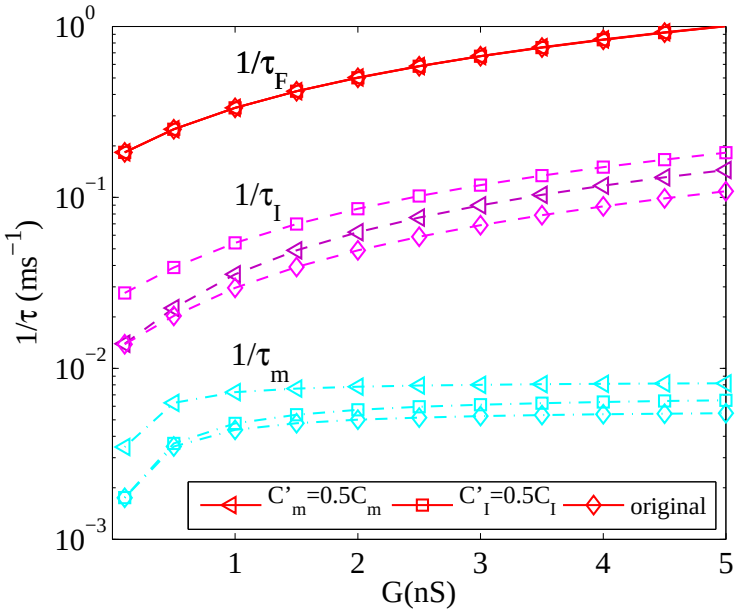

Figure 3.10: Time scale of cell dynamics. Changing C_m(C_I) by 50%, while leaving C_F and C_I (C_m) unchanged reveals fibroblast has the smallest time scale, which is one order of magnitude smaller than the others. The method is applied to determine the time scale of the other cells.

$\kappa_I(1/G+1/G_I)$, one immediately concludes that the existence of oscillations requires that n_I is proportional to $(1/G + 1/G_I)$. This provides a natural explanation for the curves shown in 3.8(b) and Fig.3.9. In addition to the linear relation between n_I and $1/G$, the analysis above allows us to obtain an estimate of the occurrence of oscillations in the uterus.

The fibroblast has an essential role in inducing oscillations in the coupled system by increasing the effective passive resting potential. With the analysis above, fibroblast relaxes to its resting state immediately, while myocyte and ICLCs behave with time scales τ_I and τ_m respectively. Thus we have,

$$V_F = \frac{G_F V_F^r + G V_m}{G + G_F} \tag{3.11}$$

With this assumption, Equ.3.6 is reduced into (see the Appendix B for the detailed derivation):

$$-C_m \frac{dV_m}{dt} = I_{ion} + n_p G_{gap}(V_m - V_p) \tag{3.12a}$$

$$-C_I \frac{dV_p}{dt} = (V_p - V_p^r)G_p + G(V_p - V_m) \tag{3.12b}$$

Here V_p and V_p^r are the equivalent passive cell membrane potential and its resting

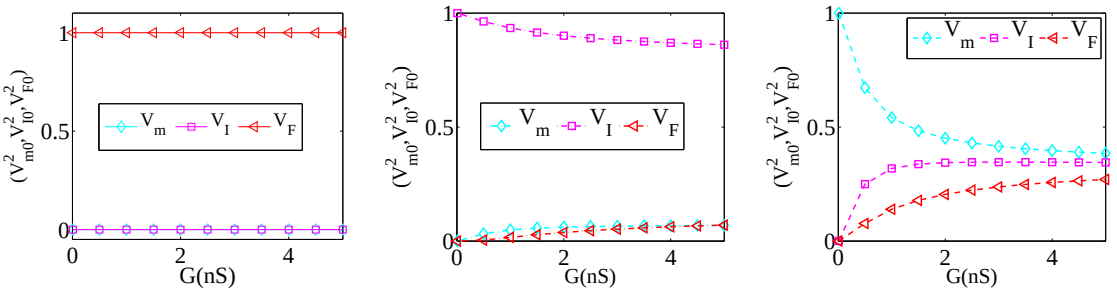

Figure 3.11: Components of eigenvectors associated with λ_1(a), λ_2(b) and λ_3(c)

potential, defined as

$$V_p^{(r)} = \frac{n_I V_I^{(r)} + n_F V_F^{(r)}}{n_p} \tag{3.13}$$

From Eq.(3.13), it is easy to understand the role of fibroblasts: it increases the effective resting potential, hence the coupling current. Taking into account the ratio between n_I and n_F, and their resting potentials, we worked out that effective resting potential $V_p^{(r)}$ is about -35mV.

The green region in Fig.3.8 shows the effect of an effective passive cell with $V_p^r = -35mV$. Clearly, oscillations could be observed by increasing the gap junction conductance G, provided there are at least $n_p/n_M > 17\%$ in the entire organ, *i.e.,* the passive cell population should be larger than 14.5%. As we mentioned above, the passive cell population accounts for about 20%. We would expect oscillations to occur at later stage of pregnancy due to the increase of gap junctions.

3.4 Discussion & Conclusions

Without the evidence of pacemaker cells in the uterus, the origin of spontaneous activities observed close to labor is not well understood. The coexistence of excitable and passive cells in the uterus, namely the myocytes and the Interstitial Cajal-Like Cells (ICLCs), implies interactions between them. Through these interactions, our numerical simulations using the very generic FHN model show that spontaneous oscillations may result from the coupling between the two populations.

In addition to the pacemaker activity observed in the generic model, the experimental investigations on the role of coupling on the uterine contractions and the direct observations of the gap junction connections between myocyte and ICLCs, promoted the hypothesis that the coupling between myocytes and the passive cells is the key role in triggering rhythmic activities in uterus.

The essential reason for the induction of oscillations in the coupled myocyte-passive cells pair system is the resting membrane potential difference between these cell types.

Our results show that at a given passive cell resting potential larger than the critical value, oscillations can be observed by increasing the coupling strength G. The fibroblasts, with a relatively high resting potential, largely facilitate the generation of oscillations: both in terms of the required coupling strength G and the number of passive cells n_p. Our study here also revealed the effective role of fibroblasts in the coupled system is nothing but increasing the effective passive resting membrane potential. This allows an easier analysis in the future work, as no distinctions are needed between fibroblasts and ICLCs.

The similar observation both in the coupled FHN model and the realistic myocyte model suggests that the oscillations that we have obtained here, with a realistic model of uterine cells, are in fact a general phenomenon, observable for the general class of excitable cells.

Our work here is based on recently published models of uterine cells [78, 43, 44], especially the Tong *et al.*. It is motivated by the electrophysiological changes observed during pregnancy, in particular at the late stage. In fact, we are restricting ourselves to the set of parameters observed shortly before delivery. The gap junctions between myocytes and passive cells provide a coupling, which is helpful to generate a depolarizing current for the myocyte.

The investigation of other aspects [98, 96, 134], such as the change of membrane potential of the myocytes from -70mV to -55mV [134] shows that spontaneous oscillations may result from a combined effect of several electrophysiological changes during

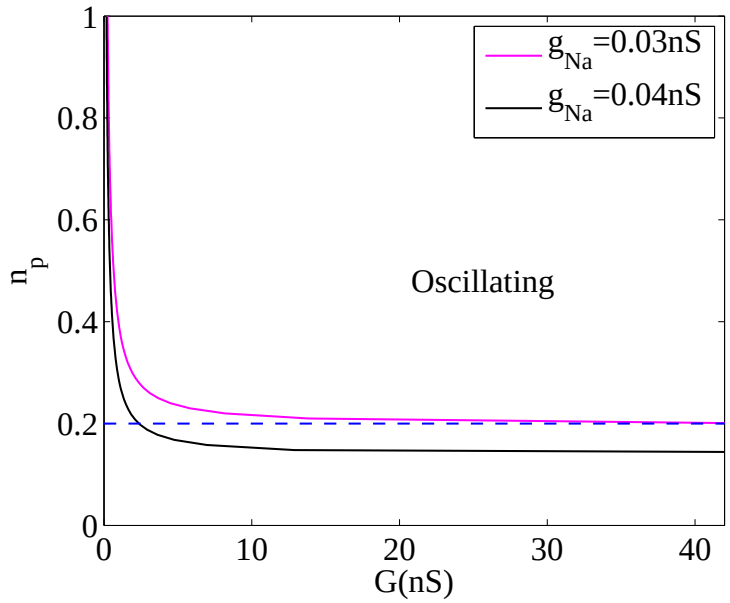

Figure 3.12: Influence of g_{Na} on the induction of oscillations. At $n_p = 0.2$, comparing to the case of $g_{\mathrm{Na}} = 0.04$, extreme larger gap junction channels (~ 800) are needed to trigger oscillation when g_{Na}=(0.03nS) is slightly reduced.

the pregnancy. A particularly important example is provided by the sodium channels. As shown in Fig.3.12, at a state of lower sodium channel expression (g_{Na}=0.03nS), to induce oscillations in a cell-pair system with $n_p = 0.2$, gap junction channel expressions as large as ~ 800 channels are needed. The increase of the sodium conductance, up to values of $g_{\mathrm{Na}} = 0.06nS$, could significantly facilitate the generation of oscillations. We believe that all these factors together guarantee quiescent state at early pregnancy and forceful contractions right before the term.

Chapter 4

Oscillations in extended systems: clusters and synchronisation

In the previous chapter, it has been seen that excitable myocytes, coupled to passive cells, can oscillate. The question that is asked here is whether, and how, an extended system with myocytes and passive cells can synchronize, potentially leading to the strong contractions observed in the uterus before birth. Again, we stress that the emergence of oscillations would occur here without the presence of pacemaker cells, which makes the problem very different from the problem of the emergence of a rhythm in other organs, such as the heart.

In the previous section, we have explored the implication of the increase in the coupling between one myocyte and several passive cells. Here, we investigate the implications of the increased coupling between mycocytes, at the level of a tissue. For the ease of computation and analysis, we begin our analysis with the phenomenal FHN model in Section 4.1, and check the results using the realistic model in Section 4.2.

4.1 2-D FHN model of the uterus

The qualitative similarity between the realistic myocyte model and the simple FHN model, as well as between the coupled myocyte-ICLCs cell-pair and the coupled FHN gives us the confidence to discuss role of gap junctions coupling between excitable myocytes using the FitzHugh-Nagumo model.

4.1.1 Model & Method

Anatomical investigations have shown the detailed structure of the uterine wall. As illustrated in Fig.4.1, the myocytes (light color who have weak or no affinity to the Methylene blue dye) form an interlacing network with pathways connecting the cells, while the ICLCs (dark blue, having strong affinity to the dye) are scattered in the network [30]. We abstract this information and model the uterus tissue with a $N_x \times N_x$ nodes Cartesian grid, with each node standing for a myocyte cell; on top of it passive

cells are randomly distributed. Passive cells are few, and scattered in the whole tissue, thus no direct connections between them are expected. Fig.4.2 gives schematic illustration of the uterine model. Each myocyte (red circle) may couple to n_p passive cells.

As stated previously, myocytes are connected by gap junctions, which is a low resistance pathway that allows ions to go through freely. Thus a current is expected when the neighboring cells have a difference in their membrane potentials. Together with current from the passive cell, $n_p^{i,j} C_r (V_p^{i,j} - V_e^{i,j})$, the electrical dynamics of each cell (i, j) in the tissue is described as following:

$$\begin{aligned}
\frac{\mathrm{d}V_e^{i,j}}{\mathrm{d}t} &= AV_e^{i,j}(1 - V_e^{i,j})(V_e^{i,j} - \alpha) - g^{i,j} + n_p^{i,j} C_r (V_p^{i,j} - V_e^{i,j}) + D\nabla^2 V_e^{i,j} \\
\frac{\mathrm{d}g^{i,j}}{\mathrm{d}t} &= \epsilon(V_e^{i,j} - g^{i,j}) \\
\frac{\mathrm{d}V_p^{i,j}}{\mathrm{d}t} &= K(V_p^r - V_p^{i,j}) + C_r(V_e^{i,j} - V_p^{i,j})
\end{aligned} \tag{4.1}$$

The term $D\nabla^2 V_e^{i,j}$ added to the equation of the excitable element represents the resistive coupling between neighboring excitable cells. In fact, we use only the 5-stencil representation of the Laplacian, which couples a cell of index (i, j) to the 4

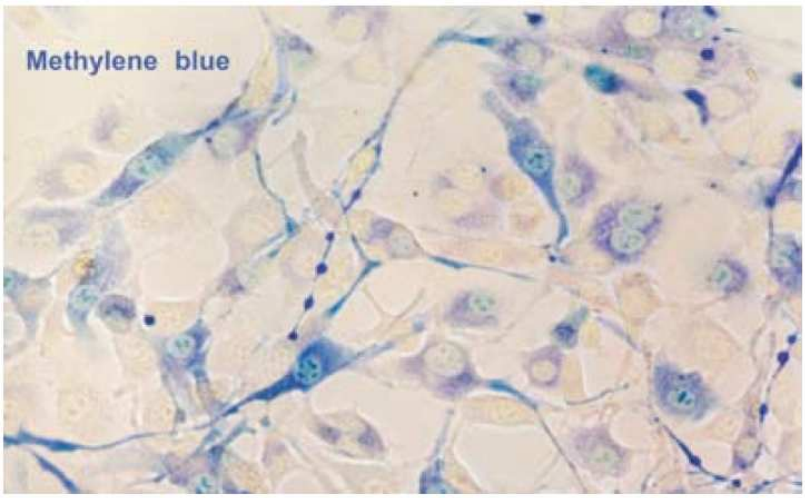

Figure 4.1: Representative methylene blue staining of myometrial ICLC in culture [30]. The myocytes (ligth color, with no affinity for the dye) forms a networks, while the ICLCs(dark blue color, with strong affinity for the dye) scattered in the network. Original magnification: $\times 400$.

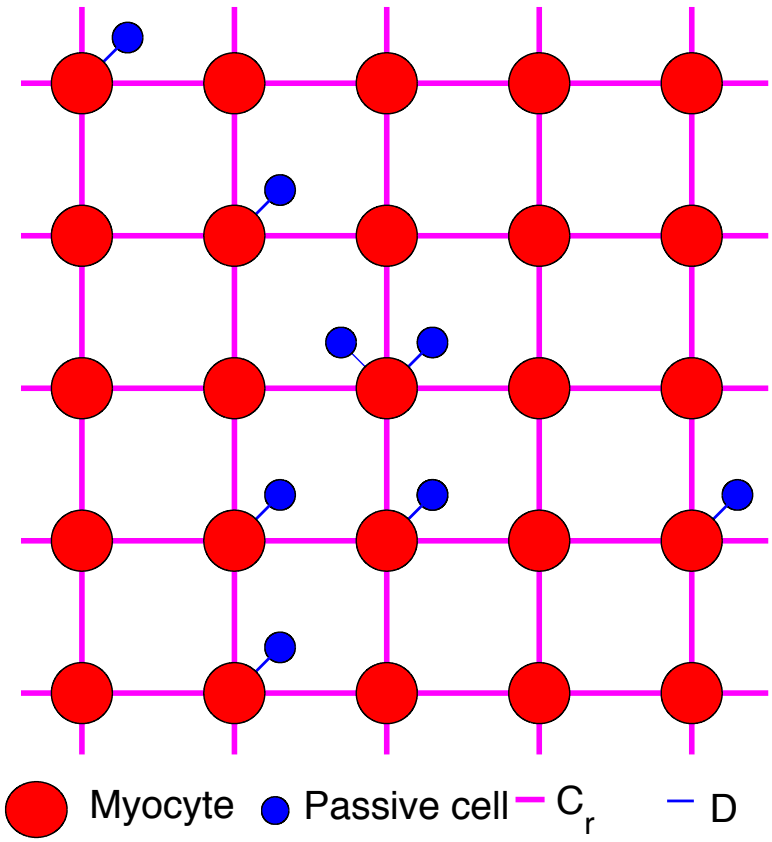

Figure 4.2: Schematic illustration of a 2-D uterine model. Myocytes form a regular grid, and passive cells (ICLCs and fibroblasts) scatter on the top.

neighbor cells $(i \pm 1, j)$ and $(i, j \pm 1)$ as:

$$D\nabla^2 V_e(i,j) = D \times \\ (V_e(i+1,j) + V_e(i-1,j) + V_e(i,j-1) + V_e(i,j+1) - 4V_e(i,j)) \tag{4.2}$$

A random number of passive cells, $n_p^{i,j}$, are attached to a myocyte (i, j). The total number of passive cells in the system is N_p. We fix here N_p, or alternatively, the ratio $f = N_p/N^2$, which we choose to be equal to 0.5. We took as values of the parameters A = 3.0, $\alpha = 0.2$, $\epsilon = 0.08$, $K = 0.25$ and $V_p^r = 1.5$. In our investigation of the global synchronization of the system, we vary both C_r and D, which are reminiscent to the changes of gap junctional conductances.

Numerically, Eq.4.1 is integrated with a fourth order Runge-Kutta scheme implemented in C. We are using here periodic boundary conditions. However, we checked that qualitatively similar conclusions would be reached with no-flux boundary conditions. We use a time step $dt = 0.05$. We checked the accuracy and convergence by reducing the time step ($dt = 0.02$) . The results presented here are based on the

analysis of the steady state regimes. In all simulations, we began by integrating the system over a time of $T_t = 2 \times 10^4$, before starting to analyze the solution. The system was integrated for a very long time, typically $T_r = 5 \times 10^3$. We checked in several cases that the results obtained truly characterize the steady state properties of the system.

4.1.2 Passive cell distribution

We consider here systems of 100×100 excitable cells. Additionally, we randomly distribute $N_p = 5000$ passive cells. Fig.4.3 shows a typical pattern of passive elements. The choice of a distribution of passive cells can be viewed as the result of some quenched disorder. In the following, we denote the distribution of passive cells attached to excitable cells a "replica". To characterize a replica, the histogram, shown in the right inset of Fig.4.3, shows the histogram of passive cells attached to one excitable cell, which is essentially close to a Poisson distribution. We will talk about this in the next chapter. The distribution of passive cells being uneven, some regions with a density of passive cells can be observed in the system (white regions in the left inset of Fig.4.3, which represent a zoom of the region marked by a dashed square at the bottom left of the system). Similarly, regions of high density are also formed.

In the rest of this section, we focus on the role of the coupling between excitable cells, *i.e.,* the effect of the diffusion coefficient D. We take $C_r = 4.6$. At this value,

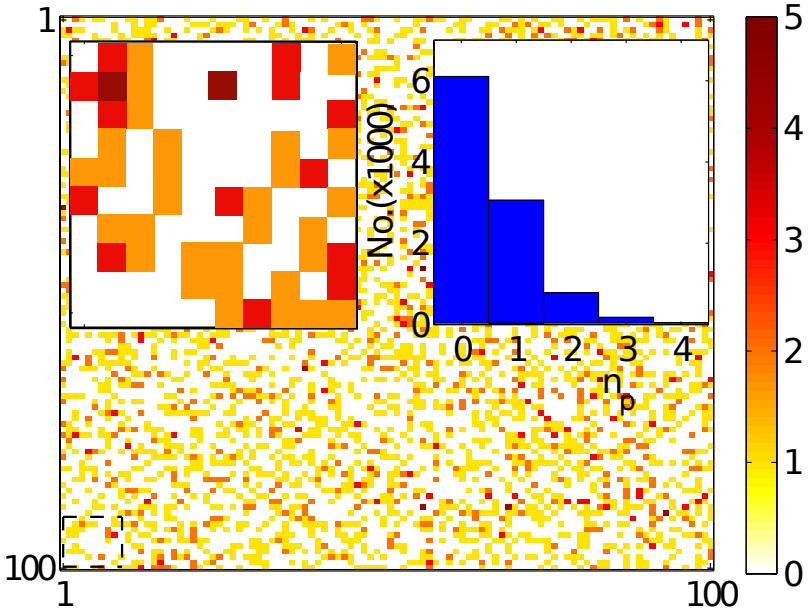

Figure 4.3: Passive elements distribution is a system of size 100×100. A zoom of the rectangular region(reft inset) shows coexistence of low and high passive density regions. The right inset shows a histogram of the number of passive elements coupled to an excitable one.

the analysis of the previous chapter shows that the critical value $f^0 = 0.495$. With our current value $f = 0.5 > f^0$, we therefore expect that oscillations should be seen when the coupling D between excitable cells is large enough (the mean-field limit).

4.1.3 Cluster formation

In the presence of a weak coupling (small values of D), passive elements affect the dynamics of the excitable cells only very close to where they are actually attached. The 0-D analysis shows that oscillations can be seen only for cell pairs with $n_p > f^0 = 0.495$. Therefore, one does not expect to see any activity unless one, or more, passive cell is present.

Fig. 4.4 shows a set of snapshots of the variable $V_e^{i,j}$, at different times. As expected, oscillations are observed in some regions, whereas cells in other regions remain inactive (quiescent). To describe this effect, quantitative measurements are needed. To characterize the state of the system, we introduce the fraction of oscillatory cells, n_{osc}, defined as the ratio between the number of oscillating cells N_{osc} and the total excitable cells $N = N_x^2$. To define a meaningful fraction of oscillatory cells, one needs to introduce a threshold to distinguish oscillations from small amplitude

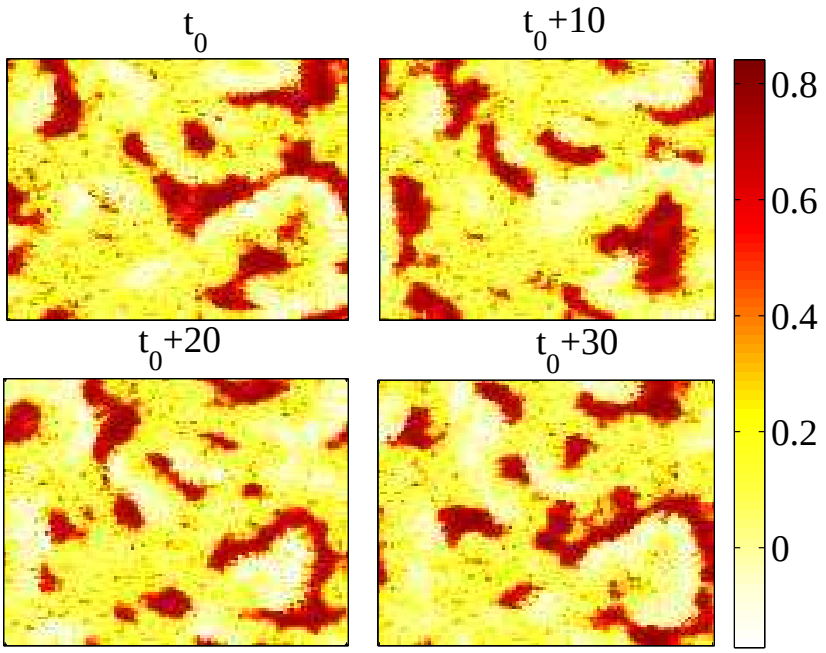

Figure 4.4: Four snapshots of $V_e^{i,j}$ with a time interval of 10. The lattice is composed of 100×100 FHN excitable elements and 5000 passive elements. The distribution of passive cells are shown in Fig. 4.3 . Random initial condition and periodic boundary conditions are used. Parameters: $C_r = 4.6$, $D = 0.5$.

noise. We chose here a threshold of 0.1, which corresponds to an amplitude of about 10% of the maximum amplitude for the oscillation of V_e. The effect of thresholding is illustrated in Fig.4.5, which shows the time evolution of V_e at different locations in the system. The oscillating amplitude, A_m, is defined here as the maximum value between the maximum and the minimum as a function of time. It is found to be of order 1, see panel (a). However, the amplitude may be much lower, as observed in panel (b) or (c). With the threshold taken here, the cell shown in panel (c), whose amplitude is $0.09 < 0.1$, is not counted as oscillating, whereas the cell shown in (b), with an amplitude of $0.35 > 0.1$, is counted as oscillating.

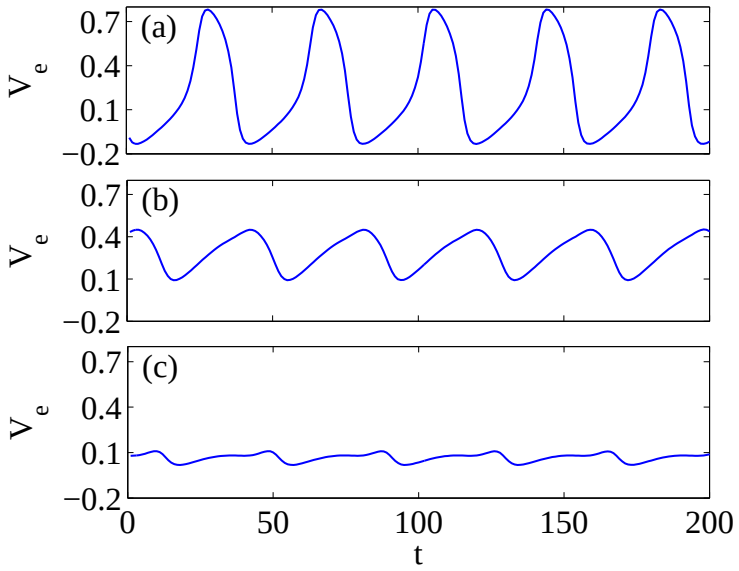

Figure 4.5: Time evolutions of V_e chosen from the system. (a$\sim$ b) oscillating cells, (c) non-oscillating cell ($V_m = 0.09$).

The standard deviation $\sigma^{i,j}$ for a give cell (i, j) , defined as:

$$\sigma^{i,j} = \sqrt{\frac{1}{t_n - t_0} \sum_{t=t_0}^{t_n} (V_e^{i,j}(t_k) - \bar{V}_e^{i,j})^2} \tag{4.3}$$

provides also some information about the variation in time of individual cells: an oscillation with a large amplitude is equivalent to a large standard deviation. The sum in Eq.4.3 refers to a sum of the points in a time series; note that $\bar{V}_e^i$ is the average over time. Fig. 4.6 shows the distribution of amplitude (panel a) and of standard deviation (panel b) for the same replica. As expected, the two patterns correlate very well. We found that a threshold of $\sigma_c = 0.03$ provides a good criterion, essentially equivalent to the criterion for A_m. Interestingly, we notice that the subcriticality of the transition close to f_c^1 makes our results have little dependence on the threshold

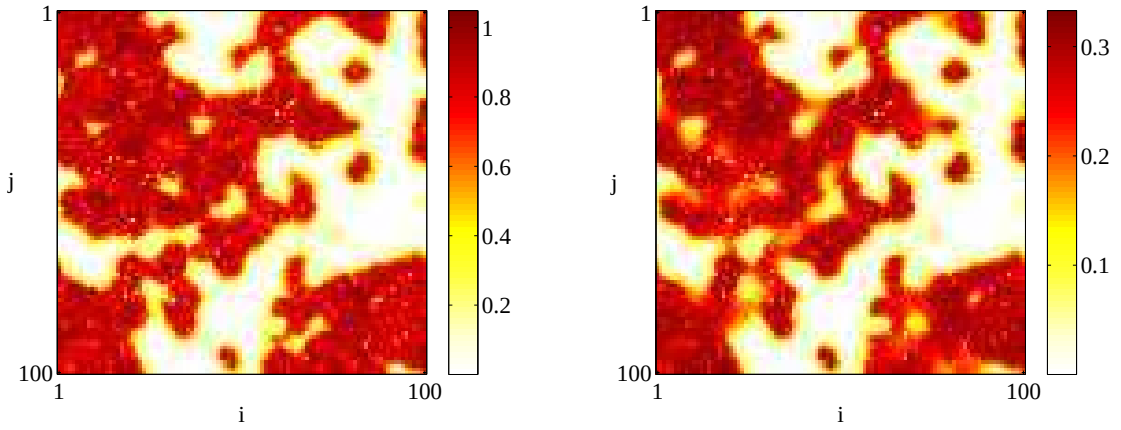

(a) A_m (b) σ

Figure 4.6: (a) Amplitude map (A_m) and (b) the standard deviation map (σ).

value. As we see extreme sharp decreases close to the boundary in the amplitude map or the standard deviation map.

Another interesting quantity is the oscillating frequency. Typical way of estimating the average oscillation frequency is $\Omega = (n-1)/\Delta t$, where n is the number of positive maxima of $V_e(t)$, and Δt is the time elapsed between the first and the last maximum [55]. This method can give incorrect results at the collision point of two

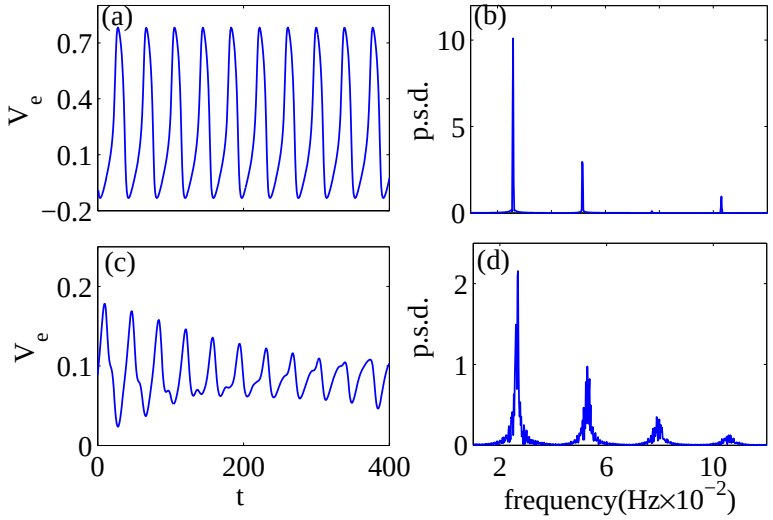

Figure 4.7: (a,b) For regular oscillating signals frequency measured in time space is same as that measured in Fourier space. (c,d) For modulated signals, direct measurement is affected by the modulation, while measured in Fourier space is un-affected.

waves with different frequencies, as shown in Fig.4.7(c).

To avoid this problem, we measure the oscillation frequency in Fourier space. The procedure is the following: we compute the power spectrum density (p.s.d.) of $V_e(t)$, the oscillation frequency is then determined by the position of the hightest peak. An example is given in Fig. 4.7. For regular oscillating signals (without any modulation) the two methods give the same results (panel (a),(b)). For signals as shown in panel (c) direct measurement gives a higher value, as it counts the tiny peaks resulted from the modulation of another signal, while the measurement from Fourier space (panel (d)) is not affected.

The quantities previously defined are now used to study the role of the coupling in the emergence of a global synchronization in the system. Fig. 4.8 shows spatial activity in the system at 3 different values of coupling strength D, starting from a random initial condition. At low coupling ($D = 0.2$), small "islands" with oscillating cells are scattered in the system. No ordered behavior is observed. Close examination of oscillation frequency reveals that within each "island", all cells are oscillating with

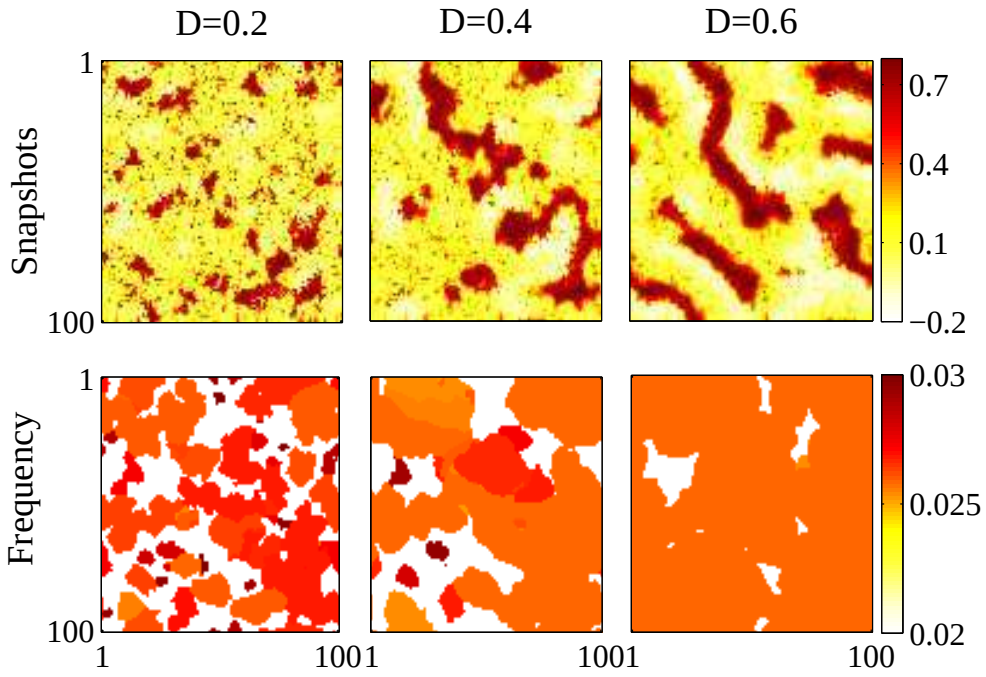

Figure 4.8: Snapshots of the variable V_e in a two dimensional domain at different coupling D starting from random initial conditions. When the coupling is small ($D = 0.2$) there is no order behavior. With the increase of coupling D, oscillating regions emerge and enlarge. Propagating waves are observed ($D = 0.4$ and $D = 0.6$). The last row shows pseudocolor plots of the corresponding oscillation frequencies. Increasing D results in decreasing the number of clusters (N_C) with distinct oscillation frequencies.

the same frequency, while different islands usually have different frequencies. We call these islands as "clusters". Here, we introduce two new quantities to describe this phenomena: the number of oscillating frequencies N_F and the number of clusters N_C. As some clusters may have the same frequency, and they are well separated, N_C is usually larger than N_F. At small D, both quantities are larger than one. We refer to this behavior as cluster synchronization (CS). With increasing D, clusters get larger and the number of different oscillation frequencies gets smaller. As the clusters grow, waves generated at different sources propagate within the clusters (D=0.4). The number of clusters as well as the wave sources and the corresponding number of frequencies decrease, eventually resulting in a single frequency ($D = 0.6$). As there are still a few cells staying quiescent, we term it as local synchronization (LS). Further increasing D, only one wave source persists in the system. It generates waves that propagate through out the entire system, as shown in Fig. 4.9. We term this behavior as global synchronization (GS), which is characterized by all elements in the system oscillating with the same frequency.

These results presented above show a close connection to two well-known observations of the electrical behavior in the pregnant uterus: (1) the gap junction which serves as the coupling between myocytes shows a remarkable increase close to the parturition and (2) activities are initially irregular, but toward labor coherent activities involving millions of cells are observed [135].

4.1.4 Global synchronization

We have seen that increasing the coupling leads to a globally synchronized state, characterized by all cells oscillating with the same frequency, although possibly with different phases. We now document that, upon further increasing of the strength of the coupling, the phases of the system also synchronize, leading to all cells oscillating collectively, therefore optimizing the contraction of the organ.

Fig. 4.9 shows an example. Comparing with the case at $D = 1.0$, more cells fire simultaneously at $D = 4.0$. A coherent state (COH), characterized by a state where all cells oscillate in phase is expected when D is further increased. Coherence is of significant importance in biological system [136]. To characterize the emergence of a coherent state, we define the maximum firing phase difference $\Delta\Phi$ by:

$$\Delta\Phi = max(\frac{|t_i - t_0|}{T}) \tag{4.4}$$

Here t_0 is the time duration after which a reference cell first reach its maxima. t_i is the elapsed time from starting point when the i^{th} element first reaches its maxima, and T is the oscillation period. The maximum is taken over the entire system. Clearly, the more cells oscillate simultaneously, the smaller $\Delta\Phi$ is, and a perfectly coherent state gives $\Delta\Phi = 0$. Fig. 4.10 shows the measured maximum firing phase difference at different values of D. One could see that $\Delta\Phi$ goes to zero linearly as a function of $D^{-\frac{1}{2}}$, which is expected from the laplacian term $D\nabla^2 V_e$ in Eq. (4.1).

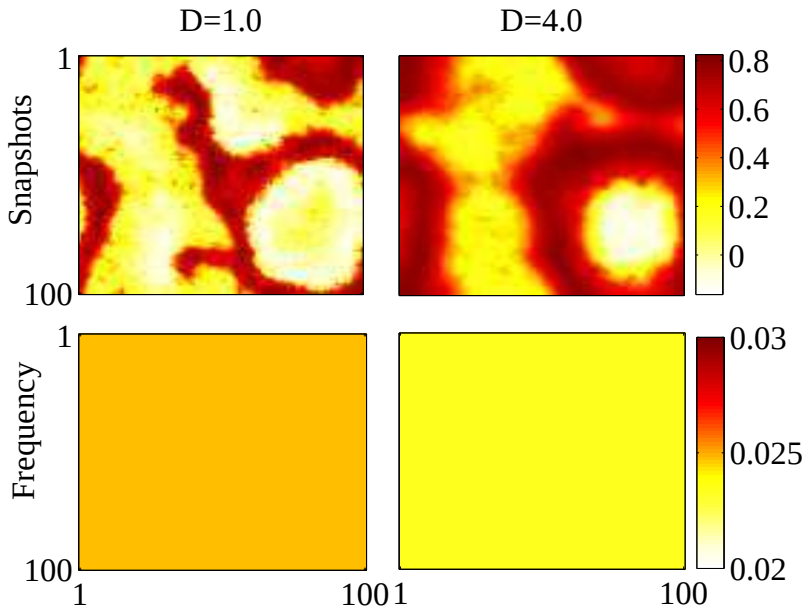

Figure 4.9: Snapshots and the corresponding frequencies show global synchronization resulted from increasing coupling strength D. Random initial conditions are used.

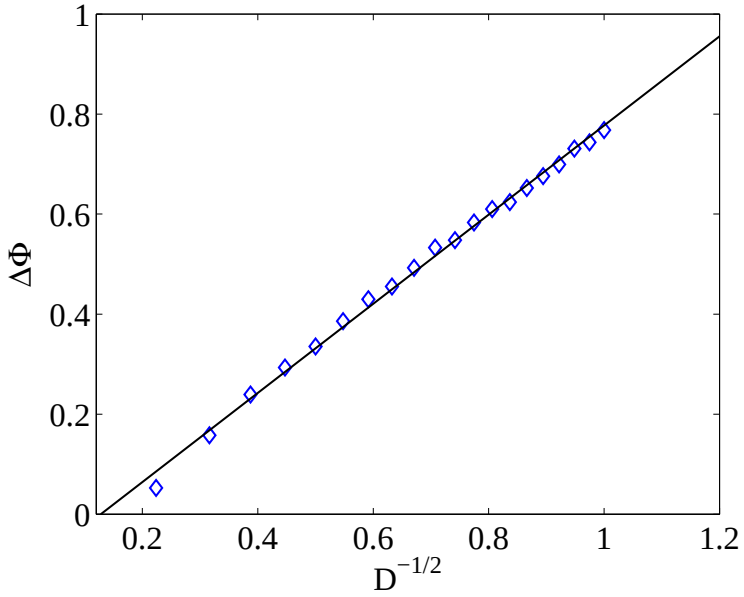

Figure 4.10: Coherent state resulted from increase coupling. Maximum firing phase difference goes to zeros linearly as function of $D^{-\frac{1}{2}}$. Random initial conditions are used for each D.

When the system has reached a coherent state (COH), each excitable element shares the same amount of passive cells ($f = 0.5$). Its oscillation frequency can therefore be estimated from the 0-D analysis: $\omega = 0.0211$. Hence, a determination of the oscillation frequency at different coupling strength (D), provides a good way to understand the mechanisms of the appearance of COH. Interestingly, the results show two different scenarios that lead to COH state: 1), the frequency decreases continuously towards the mean field limit value ω with the increase of D when initial conditions are chosen randomly and 2) the oscillation frequency goes to the mean field limit value through jumps when the system is allowed to evolve starting from a random initial state at small D, and then adiabatically increasing D.

Fig. 4.11 shows the changes of the measured oscillation frequencies as a function of D, after the system has reached the globally synchronized (GS) state. The frequency of *scenario 1* continuously decreases to the ultimate value ω (dashed line), while for *scenario 2*, it first increases with D, then suddenly jumps to a lower value. Depending on the starting states, it may take several jumps before the frequency reaches the ultimate value. For a given coupling D, there are different frequency branches. This suggests that the system is multistable. Indeed, depending on the initial conditions, different oscillating patterns are observed at a given value of D. Fig. 4.12 shows the

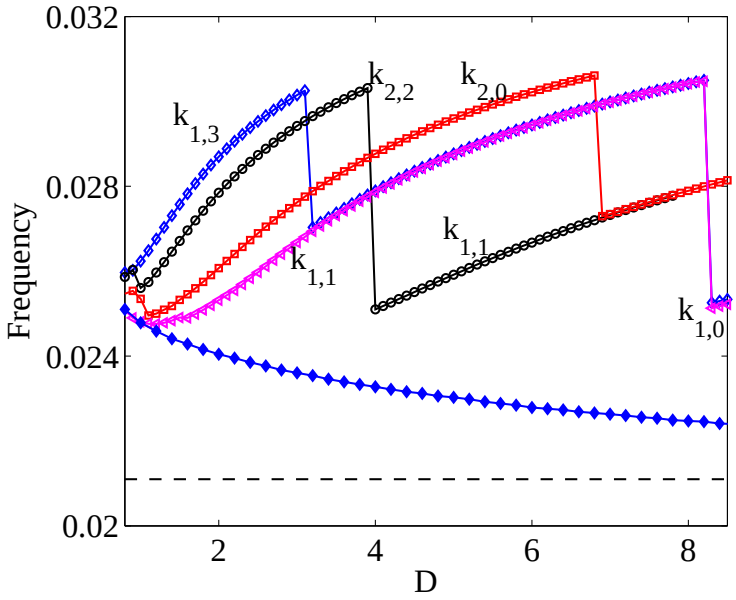

Figure 4.11: Changes of global oscillation frequency with the increase of D show two scenarios leading to the COH state. Solid curve with filled symbols, corresponding to random initial condition at each D, shows a continuous decrease of the frequency. Solid curve with open symbols corresponds to gradually increasing D starting from a random initial state at low D. Dashed line shows the ultimate frequency determined by the *0-D* analysis.

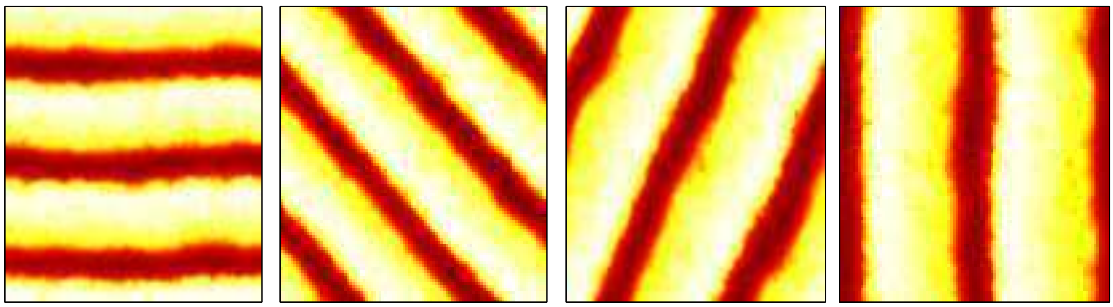

Figure 4.12: Four different oscillating patterns associated with the 4 distinct oscillation frequency branches in Fig. 4.11 (from top to bottom). Snapshots are taken at $D = 3.1$. The characterizing wave numbers are $(3,1), (2,2), (2,0)$ and $(1,1)$ from left to right, respectively.

four observed different oscillating patterns at $D = 3.1$ associated with the frequencies shown in Fig. 4.11 (from top to bottom). Interestingly, we noted that the oscillations of highest frequency are always associated with the highest wave number in the system, k, defined in our 2-D system by $k^2 = k_x^2 + k_y^2$, where k_x and k_y are the wave numbers in the two directions x and y.

The observation is that the lower the frequency, the lower the value of k. Hence, at different values of D, different oscillating patterns can be quantitatively identified by the value of k. The four patterns shown in Fig. 4.12 can be labelled by $(k_x, k_y) = (0,3)$ (panel a) $(2,2)$ (panel b), $(2,1)$ (panel c) and $(2,0)$ (panel d).

When random initial conditions are used for each value of D (*scenario 1*), only target waves are observed (see Fig.4.9). For *Scenario 2*, patterns with different wave numbers are successively observed before a final jump to the pattern of $k_x = k_y = 0$. We also noticed that a jump in frequency is always associated with a drastic change in the oscillating pattern: from large wave number pattern to patterns with smaller k. Fig. 4.13 shows observed oscillating pattern at $D = 5.0$ after the frequency jumps. Panel (a) and (b) show the observed patterns which correspond to those in Fig.4.12. For $D = 3.4$, the pattern with $(k_x, k_y) = (0,3)$ jumps into a pattern with $(k_x, k_y) = (0,2)$, identical to the one shown in panel (c) of Fig.4.12. This is consistent with the changes in frequency: after the jump, the observed frequencies for the two solutions become identical, see (see Fig. 4.11). The pattern with $(k_x, k_y) = (2,2)$ turns into a pattern with $(k_x, k_y) = (1,1)$ at a larger $D(=3.9)$.

The dramatic change of oscillating pattern and its associated jump in frequency can be normalized in terms of diffusion coefficient D and the square of the wave number k^2. Fig.4.14 shows the variation of oscillating frequency with Dk^2. One sees that all the frequency branches merge into one, and the frequency increases monotonically with Dk^2. The frequency increase in excitable media with the presence of noise has been reported, and an explanation was given in term of the excitation

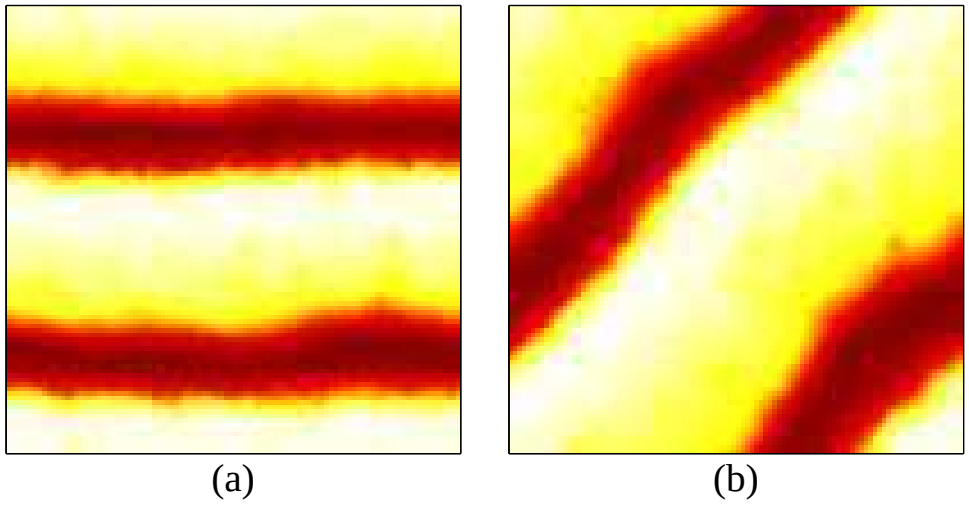

Figure 4.13: Snapshots of variable V_e after the frequency jumping. (a) Corresponding oscillating pattern ($D = 5.0$) of panel (a) in Fig.4.12 after the frequency jumping at $D = 3.4$. (b) Corresponding oscillating pattern ($D = 5.0$) of panel (b) in Fig.4.12 after the frequency jumping at $D = 3.9$.

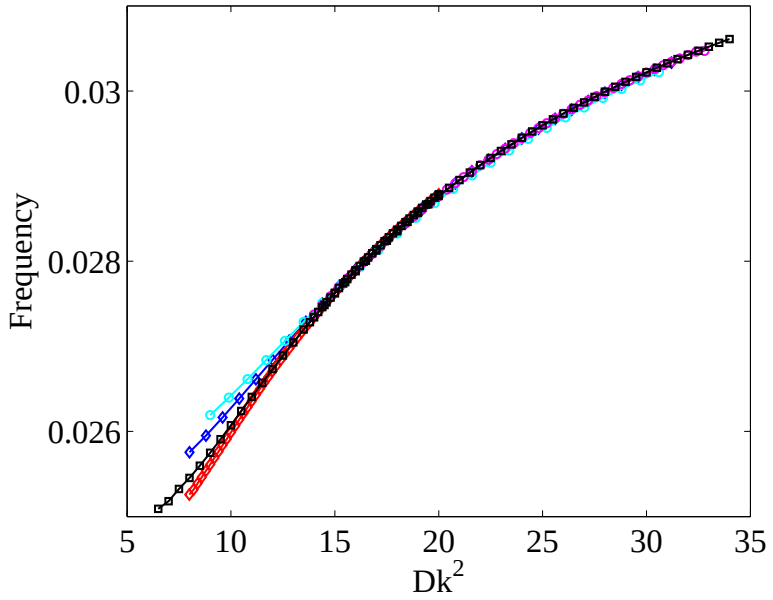

Figure 4.14: Changes of oscillation frequency with Dk^2. All the frequency branches merge into one.

across a potential barrier [137]. Here, a simple explanation can be given as the following: the increase of D makes propagation of the action potential easier, thus

the oscillation frequency must increase to keep the oscillating pattern unchanged.

4.1.5 Phase diagram

To get more information on the dependance of dynamics of the heterogeneous ensembles on the (D, C_r) parameter space, we carried out a set of numerical experiments on a system of size $N_x = 100$ containing 50% of passive cells. To determine the dynamical properties of each point in the space, we let the system evolve from a random initial condition. After discarding the transient, n_{osc}, N_F and N_c are calculated, hence determine its dynamical properties.

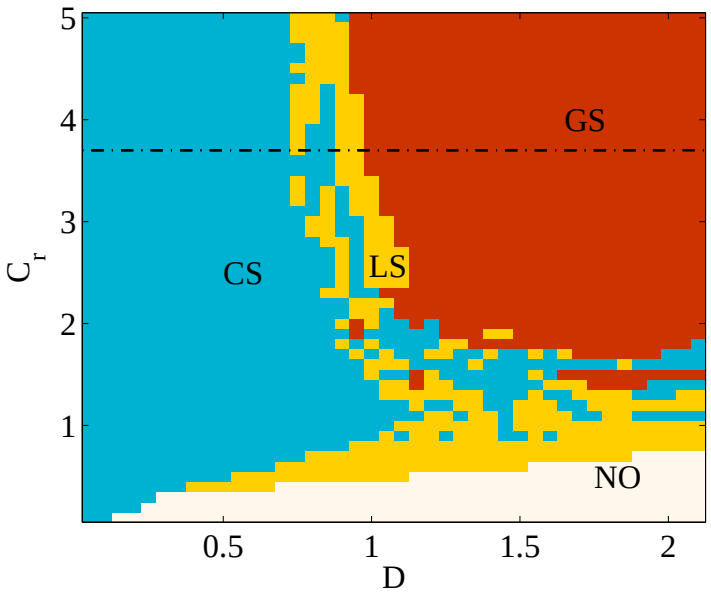

Figure 4.15: Different dynamical regimes in the (D, C_r) parameter space of two different replicas of $N_x = 100$ and $f = 0.5$. Dashed horizontal line represents the critical value of C_r that is able to trigger oscillations with $f = 0.5$ from the *0-D* analysis. Completed absence of oscillation (NO) is expected below this line as $D \to \infty$, and global synchronization (GS) is expected above the line. Cluster synchronization (CS) and the local synchronization (LS) regions appear at intermediate values of coupling strength, but with large fluctuations.

Fig. 4.15 shows the results calculated from a fixed replica. A rich variety of different dynamics can be identified in the system. The cluster synchronization (CS) is characterized as $n_{osc} < 1$ and $N_C > 1$. Both local synchronization (LS) and Global synchronization states have $N_C = 1$. The only difference is that LS has $n_{osc} < 1$ while GS has $n_{osc} = 1$. We see at a given coupling strength between passive and excitable element (C_r), the increase of the diffusion D (the coupling between excitable elements) leads the system pass from cluster SC to GS or to no activity (NO), which

is characterized by $n_{osc} = 0$, via local synchronization (LS) regime, depending on the value of C_r. Close to the no oscillation region, there are only a small fraction of oscillating elements in the LS regime. While close to the GS regime, the LS states contain a large amount of oscillating elements, which could be seen as a GS state but with some defects. The appearance of global synchronization requires both large D and C_r. Reducing either of the two leads to a destruction of GS.

From the *0-D* analysis, one would expect that no global synchronization could be observed below the line of $C_r^0 = 0.112/(f - 0.472) = 3.82$ (see Eq. (3.5)), which is indicated by the dashed line in figure. Surprisingly, GS appears far below the critical value at intermediate D. With the increase of D, the boundary shifts toward the dashed line, and eventually ends at it. One would argue that this regime largely depends on the initial conditions. The continuous region below the dashed line shows no such dependence. Thus the only possible reason comes from the distribution of passive elements, *i.e.,* the replica. A potential explanation would be as the following: at intermediate D, the influence of passive elements is limited in the neighboring excitable elements, which gives an average f in the local region larger than f_c^1. Consequently, these elements play the role of pacemakers, organizing the whole system. With increasing D, the influence of passive elements reaches the entire system, resulting in $f = 0.5 < f_c^1$ everywhere. No pacemaker regions exist, hence GS disappears. A more detailed discussion will be given in the next chapter.

The above observations suggest that there are large fluctuations close to the transition. This motivates a detailed study on how the replicas influence the transition from the asynchronous state at low coupling strength to coherent state at high coupling. A quantitative description can be given in terms of the oscillating fraction n_{osc}, the number of frequencies N_F and the number of clusters N_C.

We first focus on the transition to global synchronization (GS). For this reason we fix $C_r = 4.6$, which is above the dashed line in Fig.4.15, and vary D. Fig. 4.16 shows the averaged variations of the oscillating fraction n_{osc} as coupling D is increased. Here the average is taken over 33 realizations. To reveal the changes of the clusters, the fraction of oscillating cells in the largest cluster (the main cluster) n_m, defined as the number of oscillating cells in the largest cluster divided by the total excitable cells N_x^2, is also plotted in the figure. The corresponding number of oscillating frequencies, N_F and the number of clusters, N_C are shown in Fig. 4.17.

At low coupling strength, oscillations are scattered in the system. No prevailing cluster is observed, as indicated by the large difference between the total oscillating fraction and that of the main cluster. Several small oscillating regions coexist ($N_C > 1$), oscillating with a given frequency, and each of them contains a small number of oscillating cells ($n_{osc} < 1$). With the increase of D, oscillations expand, and small clusters merge, forming larger clusters. This is accompanied by a reduction in the number of oscillation frequencies as well as the number of clusters. This cluster synchronization (CS) turns into local synchronization (LS), when N_C or N_F reduces to 1, while oscillations do not reach the entire system ($n_{osc} < 1$). The global synchronization (GS) appears when D is further increased.

Indeed, the appearance of different oscillating regimes largely rests on the distribution of passive elements (the replica). As illustrated in the insets of Fig. 4.17 and Fig. 4.16 which show the standard deviations of n_{osc}, N_F and N_C have large fluctuations, especially at low coupling. These fluctuations may result from the distribution of initial conditions, as discussed in Section. 4.1.4. A detailed discussion will be given in the next chapter.

We now turn our discussion to the transitions towards no oscillation (NO). In the uterus, the passive cell, mainly composed of Interstitial Cajal-Like Cells (ICLCs) and fibroblasts, comprise about 20% of the cell population in the uterine tissue [27, 30]. One knows from Chapter 3 that with the constraint on f, a critical value of C_r is required which guarantees the pacemaker-like behavior, *i.e.,* generating spontaneous action potentials. When C_r is larger than the required value, global synchronization is observed. Then what happens in the case where C_r is less than the critical value? To answer this question, we carried out the same simulations at $C_r = 1.9$, which is below the critical value (see the dashed line in Fig.4.15).

Fig. 4.18 shows the average oscillation fraction with the changes of D. Different from the case at $C_r = 4.6$, the increase of D eventually leads to a complete disappearance of oscillations, rather than a GS state. This is expected from the 0-dimensional analysis: as at $C_r = 1.9$, $f_c^2 = 0.545 > f = 0.5$. We label this state as no oscillation (NO), which is characterized by $n_{osc} = 0$. The inset shows the corresponding standard

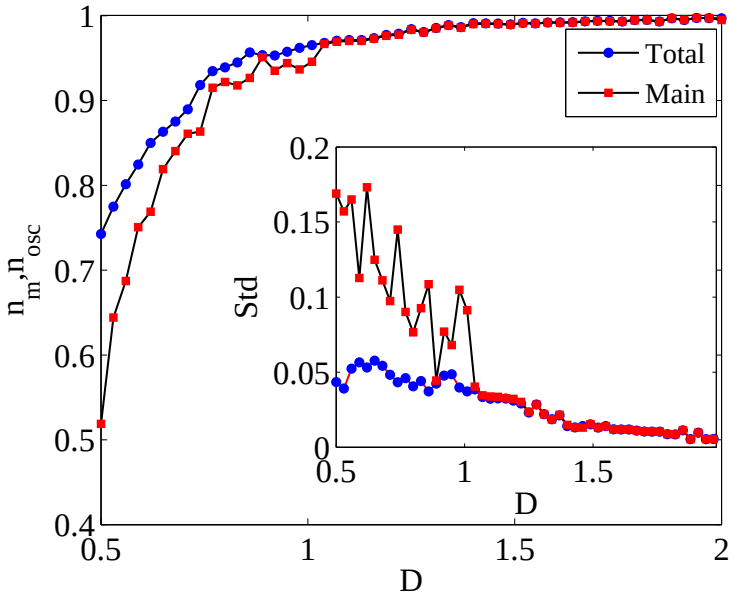

Figure 4.16: Variation of oscillating fraction n_{osc} in the entire system as well as in the largest cluster n_m with coupling strength D at $C_r = 4.6, N_x = 100$ and $f = 0.5$. Data is averaged over 33 different replicas. The corresponding standard deviation is shown in the inset.

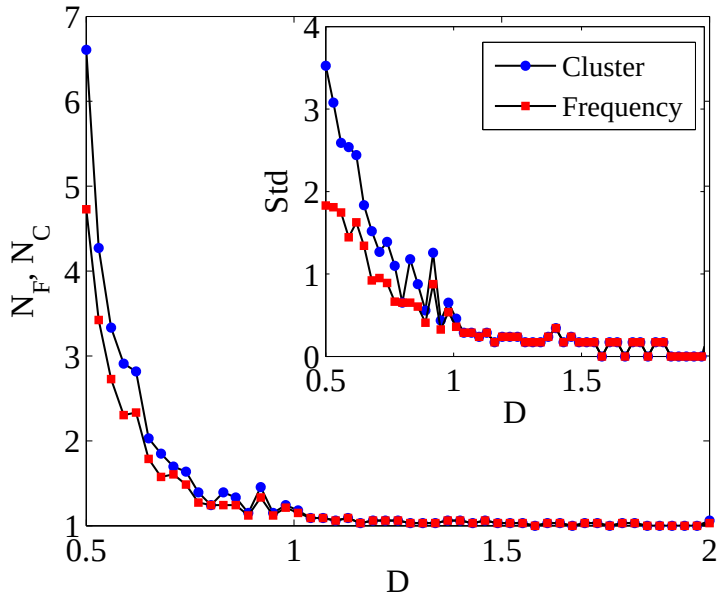

Figure 4.17: Variations of the averaged number of clusters N_C and the number of oscillating frequencies N_F with the coupling strength D. Parameters are same as in Fig. 4.16

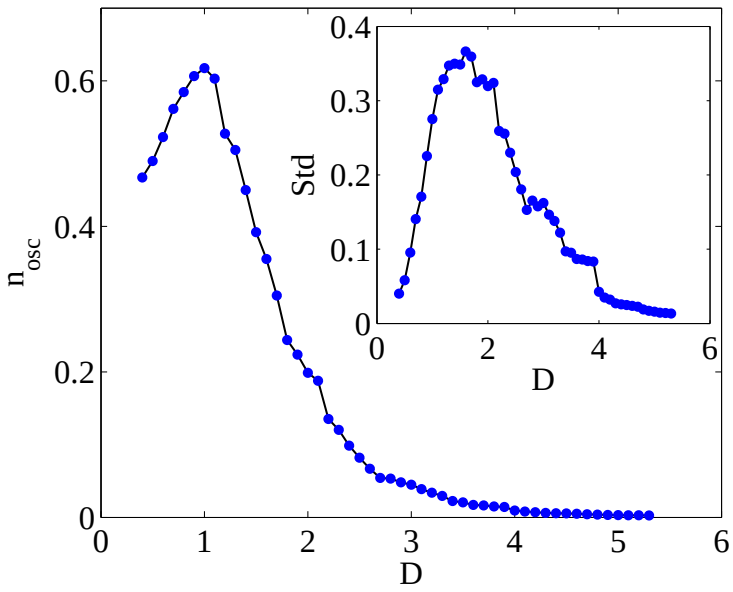

Figure 4.18: Variation of oscillating fraction n_{osc} in the entire system with coupling strength D at $C_r = 1.9, N_x = 100$ and $f = 0.5$. The corresponding standard deviation is shown in the inset. Average over 50 replicas.

deviations. One sees that extremely large fluctuations exist for intermediate values of D. A close look reveals that global synchronization could be achieved from some replicas at intermediate D, while not for others.

4.2 2-D realistic model of the uterus

We have shown in the previous section, using the FHN model, that the global synchronization can indeed result from the increase of coupling strength in mixed medium of excitable and passive elements. To verify what it is the case in the pregnant uterus close to term, we restrict here our discussion on the uterine behavior using a realistic model.

4.2.1 Model & Method

Considering the fact that in the uterus, passive cells (mainly ICLCs and fibroblasts) occupy as many as 18±2% ($= n_p/(1+n_p)$, i.e. $n_p \sim 25\%$) of the total cell populations [31], in the model we set the average $f =< n_p >= 0.2$. That gives the total passive cell population $N_p = fN_x^2$. Taking into account the length of uterine myocyte (225μm) [33], in the studies here, N_x is set to 50, which gives a system size of 1cm×1cm, close to the tissue preparations used in real experiments [138, 139].

Connected by gap junction channels, the membrane potential of each myocyte is the tissue is described as follows:

$$\begin{aligned} C_m \frac{\mathrm{d}V_m^{i,j}}{\mathrm{d}t} &= -I_{ion}^{i,j} - n_p^{i,j} G(V_m^{i,j} - V_p^{i,j}) - D\nabla^2 V_m \\ C_p \frac{\mathrm{d}V_p^{i,j}}{\mathrm{d}t} &= -G_p(V_p^{i,j} - V_p^r) - G(V_p^{i,j} - V_m^{i,j}) \end{aligned} \tag{4.5}$$

Here $n_p^{i,j}$ indicates how many passive cells are connected to the myocyte at (i,j), and we assumed all passive cells have the same resting potential $V_p^r = -35mV$. $I_{ion}^{i,j}$ is the total ionic currents, described in Section 2.3. Since the random distribution of passive cells, $n_p^{i,j}$ can be 0, 1 or 2 *etc.* for different myocte (i,j). As pregnancy goes on, the gap junctions increase dramatically, which can be modeled by an increase of the diffusion coefficient D and the coupling strength G.

Changes of uterine activity as pregnancy goes on can be studied by integrating Eq.4.5, which involves more than 20 differential equations for each cell. To solve it, we use a fourth-oder Runge-Kutta scheme implemented in C. A standard 5-point stencil is used for the spatial coupling between the excitable elements, the Laplacian term. The short time constants of some gating variables prevent us using large time steps in the simulations. For example, the activation gate of $I_{K(Ca)}$ has a time constant $\tau_\alpha \sim 0.1$ ms. Noticing the fact that with such a short time constant, the gating variable x_α will relax to its steady state $x_{\alpha\infty}$ quickly, we simply set $x_\alpha(t) = x_{\alpha\infty}(V_m)$. This enables a time step of 0.5 ms to be taken without bringing any qualitative changes of the system

behavior (errors less than 0.2% in measuring the periods of oscillations). However, the integration is still a tedious work: it evolves a total of more than 100 equations for each cell, and for the system we consider here it requires a huge computations. As there are multi-cup clusters available in Pôle Scientifique de Modélisation Numérique (PSMN), we use the Message-Passing-Interface (MPI) library to distribute the work load to different processors.

4.2.2 Results

As mentioned already stages of pregnancy can be described in terms of coupling strengths between excitable myocytes D and between myocytes and passive cells G, We study here the dependence of the system dynamics on these two parameters.

Fig.4.19 shows the spatiotemporal evolution of the membrane potential of the uterine tissue as diffusion coefficient D increases at a given coupling strength $G = 3.5$nS between myocyte and passive cells. At early stage, gap junctions are too few, no action potentials are observed, the uterus stays quiescent (not shown). As the gap junction

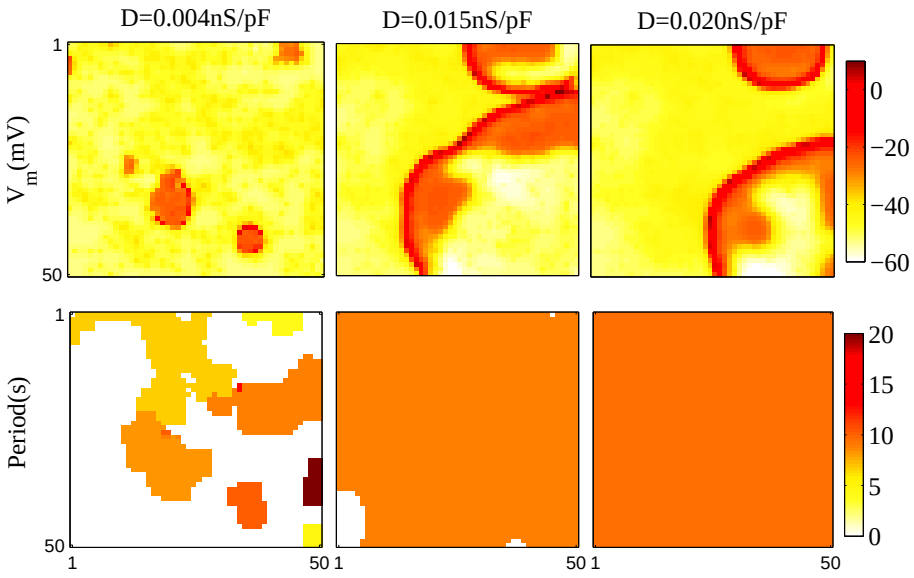

Figure 4.19: Emergence of different global activity regime with increasing gap junction conductance. Snapshots of V_m (first row) in a 2-D uterine model ($N_x = 50$) with 20% passive cells, and with different values of the diffusive coupling between myocytes D. Th second row shows pseudocolor of the periods of individual myocytes in the model. An increase in D leads to a decrease in the number of clusters with distinct oscillation periods, and this eventually leads to globally synchronized oscillations. Simulations are done with $G = 3.5$nS.

between myocytes is increased during pregnancy, we observe a transition from highly localized, asynchronized oscillations to spatially organized global oscillations: For low gap junction density ($D = 0.004$nS/pF), areas with relatively high passive cell density start to oscillate with distinct periods, while the cells in the same area have the same period. Note that regions with low passive cell density stay quiescent. This regime is termed as Cluster-Synchronization (SC). With increased values of D the oscillating clusters merge, forming larger clusters, and reducing of the number of different periods. This eventually ends up with only one period in the system. Depending on the coverage of oscillations, there are two regimes: Local synchronization (LC), characterized by $n_{osc} = N_{osc}/N_x^2 < 1$ and Global synchronization characterized by $n_{osc} = 1$ as studied in the FHN case [140].

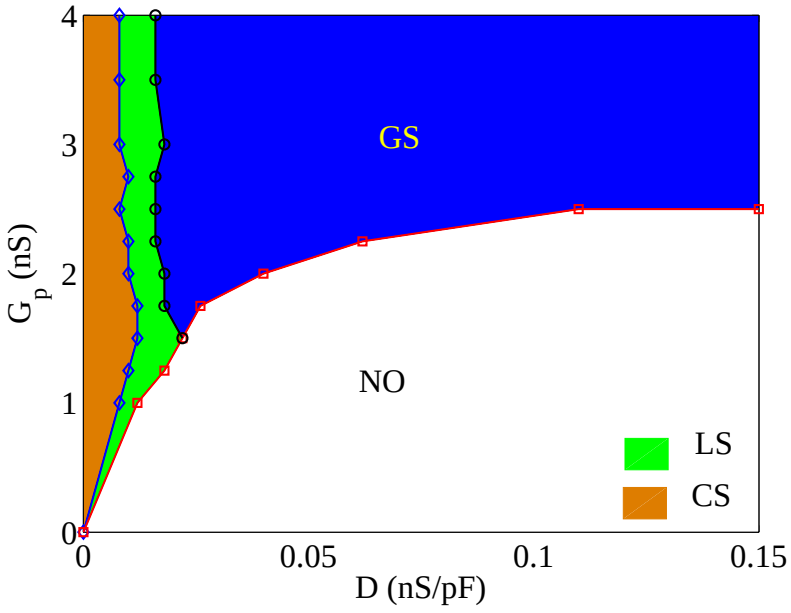

Figure 4.20: Different dynamical regimes of the uterine tissue model in (G, D) parameter plane indicating the regions (i) without any oscillating activity (NO), (ii) cluster synchronization (SC), (iii) local synchronization (LS), and (iv) global synchronization (GS).

To get a deeper insight of the different activity regimes exhibited in the system by increasing gap junction conductance, we built a phase diagram in (G,D) parameter space (see Fig.4.20). In addition to the above mentioned regimes, we also observe a region in which all the cells stay quiescent, which we label "No Oscillation" (NO). As one would expect the boundary between the NO and GS tends to a value of $G \sim 2.7$nS determine by $n_p = A/G + B$ as D goes to infinity. Below this critical value, the increase of D eventually leads to a complete disappearance of oscillations. The observation that global synchronization only appears at large D and G suggests that the break-down of the gap junctions (*i.e.,* small D and G) could lead to the

disappearance of the uterine rhythmic activity. Indeed, Tsai *et al.* has shown that the disruption of the gap junction communications by chemical agents immediately inhibits the spontaneous uterine contractions [51].

The spontaneous increase of gap junctions during pregnancy suggests that the uterus undergoes a series changes from the left-bottom corner of the phase diagram to the right-up corner. This allows the uterus to experience different dynamical regimes, from quiescent to global activities via cluster synchronization.

To further understand the electrical activities right before parturition, we also looked at the propagation of action potential waves in the system in the regime of GS. As depicted in Fig.4.21, spiral like waves emerge in the system. Comparing to the experimental measured pattern of propagation of action potentials recorded in rat uterus [141], as depicted in Fig. 4.22, our results faithfully reproduce the observed features.

Fig.4.23 shows a trajectory of the tip of spiral waves. The tip moves randomly in the system. When the tip moves out from the system, it follows a long period of quiescence, after which waves of action potential settle in again. A long time trace of the membrane potential of one randomly chosen cell in the system shows bursting behavior (see Fig.4.24): a series of action potentials follow a long time period of quiescence. We noticed that each burst composed of several long period spikes (∼20s) and fast spikes (short period, ∼1s). These fast spikes are related to the appearance

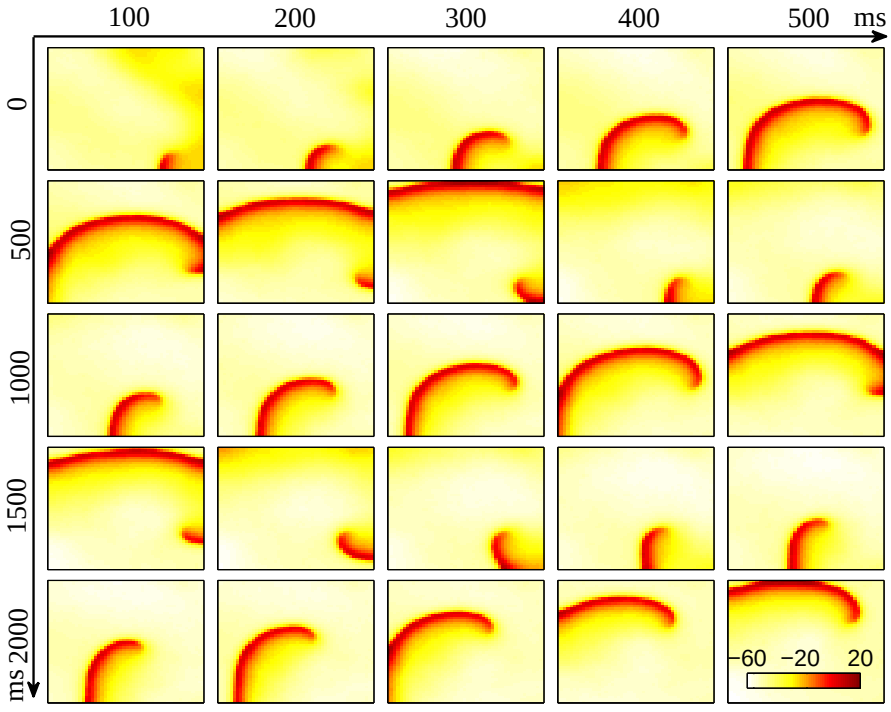

Figure 4.21: Patterns of electrical activity observed in the model. Action potentials rotate around the tip of the spiral. Parameters: $G = 3.5$nS, $D = 0.1$nS/pF.

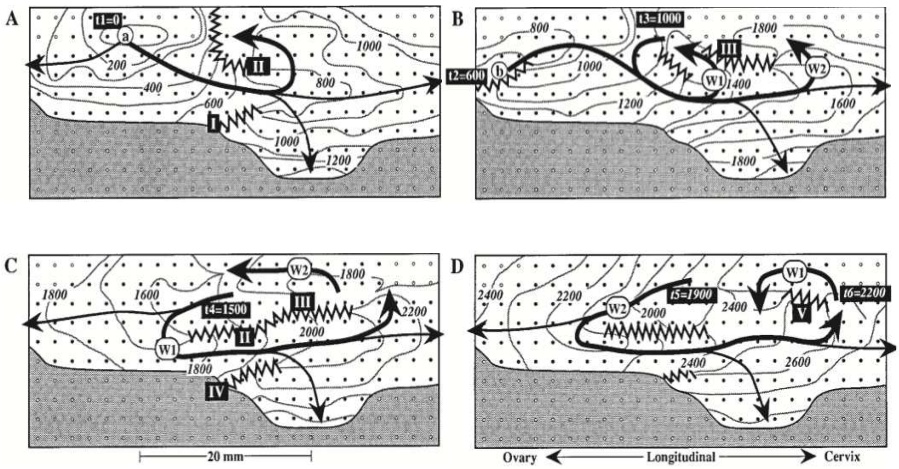

Figure 4.22: Experimentally measured propagation of action potentials in pregnant uterus. A through D display a continuous sequence of propagation during a period of 2.8 seconds. Replotted from [141]

of spiral waves.

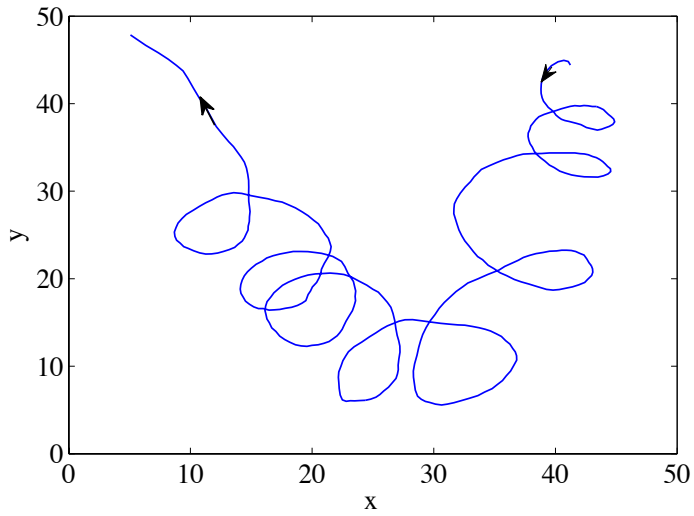

Figure 4.23: Trajectory of the spiral tip of the spiral waves shown in Fig.4.21.

Bursting of membrane potential is of crucial importance to the generation of forceful contraction in uterus. The frequency, amplitude, and duration of contractions are determined mainly by the frequency of occurrence of the uterine electrical bursts, the total number of cells that are simultaneously active during the bursts, and the duration of the uterine electrical bursts, respectively [23]. Simple excitation-contraction

models [44, 47] suggest a high-frequency-pass mechanism in the generation of calcium induced contractile force. This indicates that the strength of contractile force is mainly determined by the number of fast action potentials. We have mentioned previously that spiral waves terminate as the tip moves out from the system. Since the tip does a random walk in the system, doubling the system sizes can lead to increase of the number of fast spikes by a factor 4. Stronger contractile force is expected in larger uterus.

With the increase of the gap junction conductance D, these waves become more regular: generated in a region with relative high passive cell density and propagating through out the whole system (See Fig.4.25). We noticed that it takes about 340 ms for the wave to propagate from one side to the other side. By assuming the cell length is 225μm [33], we got a action potential propagation velocity of 3.2cm/s. This observation is consistent with the experimentally measured value [139, 142].

4.3 Discussion & Conclusion

We demonstrated in this chapter, using the FHN model, the appearance of synchronization in heterogeneous systems without any oscillating agency can be achieved through self-organized manner. Depending on the coupling strength, a rich variety of collective behaviors is observed; in particular, at intermediate coupling strength, groups of cells spontaneously form clusters that oscillate at different frequencies while maintaining same frequency within each clusters. With the increase of coupling strength, clusters expand and merge with each other forming larger clusters, and

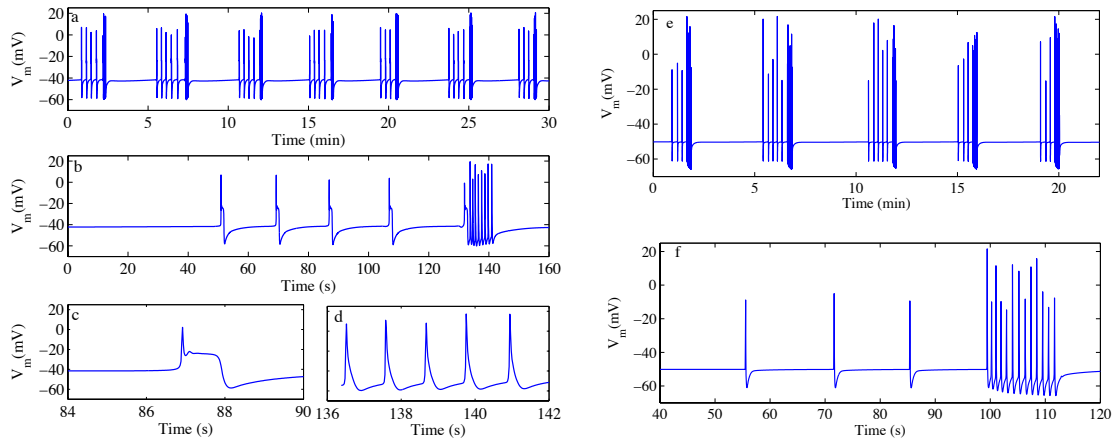

(a) $N_x = 50$ (b) $N_x = 100$

Figure 4.24: Bursting behavior of uterine electrical activity. Each burst comprises long period spikes and fast spikes, which correspond to spiral waves. Increasing the system size leads to an increase of fast spikes within a burst, with evident change of the inter burst interval.

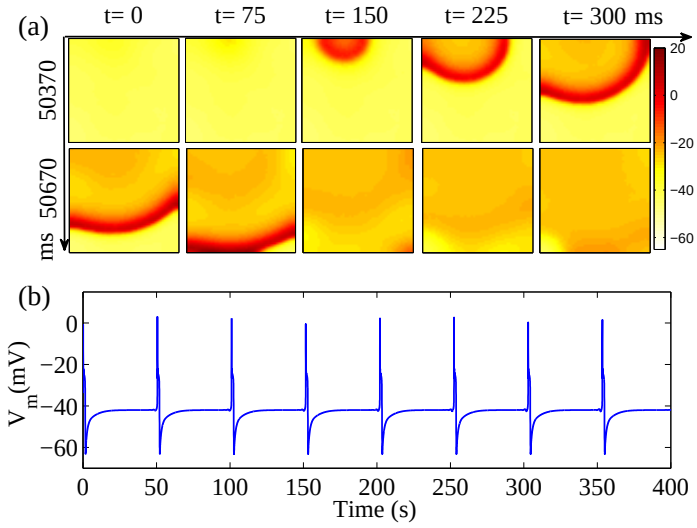

Figure 4.25: (a) Wave patterns at large coupling strength D=0.2nS/pF. A wave front takes about 340ms to from top of the system to the bottom. (b) Time trace of the variation of membrane potential of a randomly chosen cell in the system.

eventually give rise to a globally synchronized state. Coherent state marked as all cells firing simultaneously is achieved by further increase of the coupling. These results catch qualitatively a set of changes occurring in the uterus during pregnancy, and can be used to explain several important features known about the emergence of contractions.

The mechanism of synchronization in uterus suggested by the studies of coupled FHN system has been confirmed by considering a realistic uterine model, in which no pacemaker-like agencies has been identified experimentally. The emergence of spontaneous oscillations in the coupled excitable and passive systems gives reasonable explanation of the origin of uterine contractions, as close connections between myocytes and ICLCs do exist in the uterus [27]. The dramatic increase of gap junctions during pregnancy [36] suggests that the changes in the uterus with time are similar to increase D and C_r simultaneously in Fig. 4.15, which leads from quiescence at low coupling, eventually to global synchronized oscillations at strong coupling. In addition, the frequency enhancement in the case of adiabatic increase of coupling is also consistent with experiments [134].

The results obtained both from the very generic FHN model and the realistic model show a great similarity. Although in the case of FHN model, we considered a system containing a larger number of passive element fraction comparing with that in the uterus, no qualitative changes is observed compared to the realistic model. Comparing to the results obtained using $f = 0.7$ [140], smaller f only shifts the transition boundaries to high values of C_r. This suggests that the mechanisms of synchronization we discussed here can be applied to a broad class of systems composed of passive and excitable elements [65, 66, 132].

Besides these qualitative description, the realistic model went much further: (1) The irregular action potential propagating patterns have been reported in rat uterus [141], the similarities have been confirmed both in terms of wave direction and wave velocity; (2) Bursting of the action potential, which is of crucial importance for a successful expulsion of the fetus, is observed at tissue level. Indeed, to the best of our knowledge, no bursting has been reported *in vitro* or *in vivo* experiment at the single cell level, but it does appear in the uterus [36]. These results strongly prove our assumption of the role of gap junction couplings in process of pregnancy.

Chapter 5

Disorder-induced fluctuations, system-size dependence and scaling

5.1 Introduction

In the previous chapters, we have studied the appearance of electrical activity, leading to uterine contractions using both a realistic model (Tong's model) and a generic model (FitzHigh–Nagumo model). Our work suggests that the increase of the coupling, resulting from the increased expression of gap junctions during pregnancy, can lead to an electrical activity that is synchronized over the entire uterus, eventually leading to strong contractions and to the expulsion of the fetus. Using available information on the structure of the uterine tissue, we have introduced a simple model with excitable cells on a simple square lattice, in a 2-dimensional system of size $N_x \times N_x$, each excitable cell being coupled to a varying number n_p of passive cell. The number n_p was chosen randomly, to reflect the strong variability observed in real tissue [30]; in the study, we restricted ourselves to simple probabilistic laws, such as the binomial or the Poisson law [143]. Once the specific distribution has been chosen, the mean value of the distribution of passive cells, $f \equiv mean(n_p)$, is thus the parameter that characterizes the distribution. The numerical solutions of this model exhibit a variety of irregular spatio-temporal regimes, reminiscent of what has been observed in other systems of coupled cells, essentially in the cardiac context [65, 66, 132, 68, 144]. In relation to the physiological problem, the systematic dependence of the behavior of the solution of the model has been studied as a function of the two coupling coefficients: D between excitable cells, and C_r between passive and excitable cells [140]. The main conclusion of this work concerns the emergence of synchronized oscillations when the coupling coefficients D and C_r become large enough, in qualitative agreement with what is known for uterine tissue.

However, the disorder, due to the random distribution of passive cells coupled to excitable cells, has not been addressed so far. The importance of the disorder in various phase transitions has been studied very extensively [145, 146]. In our case, we are interested in the transition towards a regime of sustained activity, and the

question we are asking is: how does disorder affect the transition ?

A given distribution of passive cells attached to the myocytes in the lattice can be viewed as a particular realization of a quenched disordered system. We use here the terminology of the spin glass theory [147], and denote an individual realization as a replica. Whereas one may expect that the emergence of synchronized oscillations in the system, which is a macroscopic property, should depend on the macroscopic properties of the system, *i.e.*, the mean value f, one may also expect that the detailed (microscopic) properties of the distribution will be important, hence that the transition may depend on the particular replica. We are therefore interested here in the fluctuations in the macroscopic behavior of the system, due to the particular disorder of the system (replica).

To this end, we characterized the nature of the numerical solutions, and determined the dependence of these solutions on the two coupling coefficients, D and C_r [140]. One of the main features observed in our numerical study of systems with a relatively small size, $N_x \approx 100$, is the existence of very large fluctuations of the behavior of the system for a given set of coupling parameters, (D, C_r), depending on the replica (see Fig.4.16). In fact, for a given set of coupling parameters, the system can be either in a state where *all* the cells oscillate with the *same* frequency, whereas for other replicas, the system can be in a state where the majority of cells are inactive, with a weak activity localized in some sub-domains of the system.

These very different behaviors can be understood qualitatively by observing that for a set (D, C_r), oscillations are possible only when the number of passive cells coupled to a given excitable cell f is within a certain range, $f_c^1 \leq f \leq f_c^2$ (see Fig.3.3 in Chapter 4). One of the main observations of this chapter is that for values of $f \leq f_c^1$, the dynamics of the system strongly differs from one replica to the other. This is manifested in particular when studying the dependence of the dynamics when the coupling coefficient D is varied. This is due to the fact that close to the threshold $f \approx f_c^1$, the local fluctuations of passive cell density, not just the mean value over the entire tissue, are important. The definition of the local density involves a coarse-graining length, d. On general grounds, this length is expected to be related to the coupling between excitable cells, that is, $d \propto D^{1/2}$. At a given value of the coupling coefficient between ecitable cells, D, and between excitable and passive cell, C_r, whether cells oscillate or not will therefore be critically dependent on the detailed properties of the distribution of passive cells attached to excitable elements. In this work, we quantify these effects, and characterize these large replica-to-replica fluctuations.

One consequence of the above pictures is that the properties of the system should depend on the size N_x of the system. Indeed, as the size of the system N_x increases, the probability that, for a given couple of values of D and C_r, the fluctuation of the number of coupled passive cells around a myocyte becomes larger. As a result, the probability to find oscillating cells, for a given set of coupling parameters D and C_r is expected to increase with the size N_x of the system. We characterize this finite-size effect, and show indeed a dependence of the properties of the system with its size, typically involving the logarithm of the size, $\ln N_x$.

The picture presented in the previous paragraph leads to the prediction that the parameter that controls the *averaged* behavior of the system is the combination $\sqrt{\frac{D}{\ln(N_x)}} \times \mu$; where $\mu \equiv (f - f_c^1(C_r))/f_c^1$ represents the difference between the averaged number of passive cells connected to an excitable cell, f, and the critical value, $f_c^1(C_r)$, estimated from *0*–D analysis Eq.(3.5b), normalized by the ratio $\sqrt{\frac{D}{\ln(N_x)}}$, which represents a competition between diffusion, which tends to smooth the local differences of the passive cell density, and the increase of the system size, which allows the system to explore more local configurations of the passive cell distribution. The introduction of this variable can be interpreted as a scaling relation, familiar in the context of transition to the thermodynamic limit in statistical mechanics (finite-size scaling). We demonstrate that this variable correctly represents our own numerical results.

5.2 Global oscillations and large fluctuations

The model we consider here is same as that presented in Chapter 4: excitable cells form a grid of size $N = N_x \times N_x$, with each nodes representing an excitable cell, and $M = N \times f$ passive cells are randomly distributed on the top of the lattice. The system dynamics is governed by Eq.(4.1). As usual, C_r and D describe the excitable–passive and excitable–excitable coupling strengths, respectively.

Each excitable cell (i, j) is locally coupled to a different number $n_p^{i,j}$ of passive cells. The quantities $n_p^{i,j}$ are integer numbers and were chosen by the following procedure: a set of M pairs of indices (i, j) were randomly generated, each pair having the same probability $(= 1/N)$. A particular pair of indices can be chosen an integer number of times; we then attach to each node, *i.e.*, to each excitable cell, as many passive cells as the number of times that its indices appear in the list of M pairs. Spatial distributions of the set $\{n_p^{i,j}\}$ are refered to as replicas. Each replica can be viewed as a realization of a quenched disorder.

We have shown in Chapter 4 that as long as there is more than $f = 0.484$ passive cells attached to a myocyte, oscillations could be observed by increasing C_r, the coupling strength between passive and excitable cells. We considered here the case $C_r = 1.9, f = 0.5$ (green ★), which is slightly below the oscillating boundary, as shown in Fig.3.3. At this coupling strength $C_r = 1.9$, f is smaller than $f_c^1 \approx 0.545$ and $f_0 \approx 0.529$, below which finite amplitude solutions do not exist. The deviation between the value of f and the threshold is:

$$\mu = (f_c^1 - f)/f_c^1 \approx 5.710^{-2} \ll 1 \tag{5.1}$$

which characterizes the distance to the onset. With this set of parameters, several features of the solutions can be predicted from the following arguments.

• When the coupling between excitable cells is very strong, $D \to \infty$, a mean-field approach $n_p^{i,j} = f$ is expected to become exact and the analysis of the 0-D system

leads to the expectation that no oscillations exist.
• In the opposite limit of a very weak coupling, $D \to 0$, cells which are not coupled to a passive cell do not oscillate, whereas cells coupled to a single passive cell oscillate, and no global behavior is expected to emerge.

We focus here on the situation of intermediate coupling between excitable cells. To this end, we integrate the system (Eq. (4.1)) numerically with a fourth-order Runge-Kutta scheme, using time step $dt = 0.05$, starting from random initial conditions. The time variation of V_e is recorded for 5000 time units, after having integrated for $20,000$ time units, which turned to be sufficient to reach the statistically steady state of the system. The recorded signal is then used to calculate the fraction of oscillating cells n_{osc}, the frequencies, and other quantities characterizing the evolution of the system as a function of D (see Chapter 4). The results reveal that the typical oscillation periods are of the order of 37, in our time units. The value of the period is typically determined

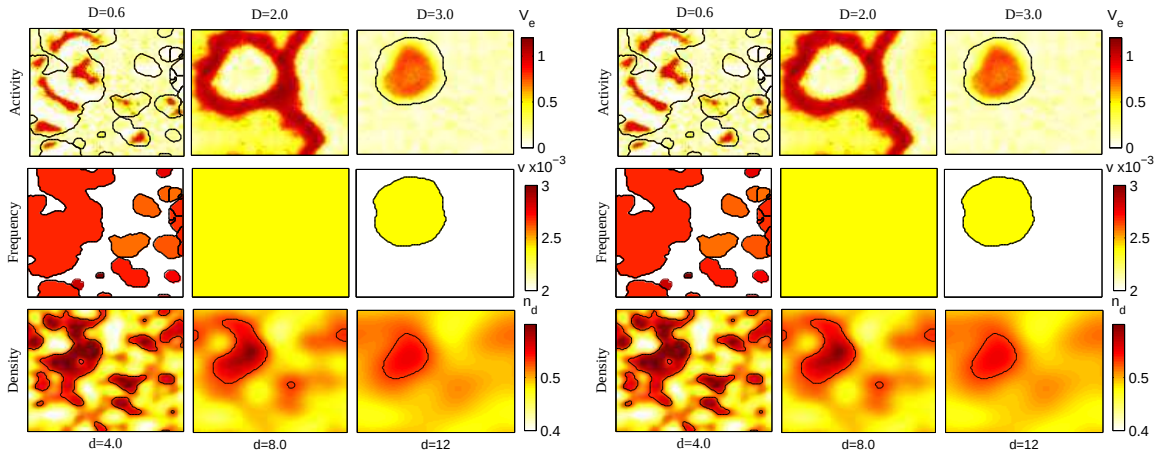

(a) Replica 1 (b) Replica 2

Figure 5.1: Replica-dependent fluctuations close to the transition to sustained oscillations in 2D systems of coupled excitable and passive cells, with identical sets of parameters ($f = 0.5$, $C_r = 1.9$, $N_x = 100$), and increasing values of the coupling strength D. Snapshots of activity V_e for two different replicas are shown in the top rows of (a) and (b). The frequencies of individual oscillators in the medium are shown in the pseudocolor plots in the second row (white corresponds to absence of oscillation). The last row shows the local density of passive cells averaged over a length scale d indicated below each frame. For the replica shown in (a), we observe global synchronization at $D = 2$ followed by progressive cessation of spontaneous periodic activity in the system indicated as a shrinking region of oscillating cells when coupling is increased further. However, for the replica in (b), coherent oscillation is not observed as D is increased, with the existing localized oscillating clusters having distinct frequencies gradually decreasing in size.

by the relaxation of the slow variable, $\sim 1/\epsilon$ [87]. Fig. 5.1 shows several snapshots for two different replicas and for increasing values of the diffusion coefficient D. One sees that, as shown in Chapter 4, oscillations exist in localized regions of various sizes, denoted as clusters, where propagating waves are observed. Depending on the replica, global synchronization (GS), defined as all cells in the system oscillate with the *same* frequency, can be observed, see Fig. 5.2a ($D = 2$,middle column), even in the case of $f < f_0$. On the contrary, no trace of global synchronization is observed for other replicas: oscillations remain confined within localized regions, and oscillations occur with different frequencies, as indicated in the second column of Fig. 5.1b.

Another illustration of the quantitative difference between the dynamical regimes observed for different replicas can be seen from the phase diagrams, obtained by varying both the coupling coefficient between excitable cells D and between excitable and passive cells C_r[140]. Fig. 5.2 shows two phase diagrams corresponding to two different replicas of size $N = 50^2$. As already seen (see Chapter 4), the observable dynamical regimes are either (i) no oscillations (NO); (ii) oscillations exist in clusters in which all cells share the same frequency but with different frequencies from one cluster to another (region labeled "CS" for cluster synchronisation), (iii) oscillations exist in one cluster but with some non-oscillating cells in the system (region labeled "LS", for local synchronisation), and (iv) oscillations exist everywhere in the system with the same frequency ("GS", for global synchronisation). These regimes, color coded as explained in the caption of Fig. 5.2, are shown for two different replicas. In

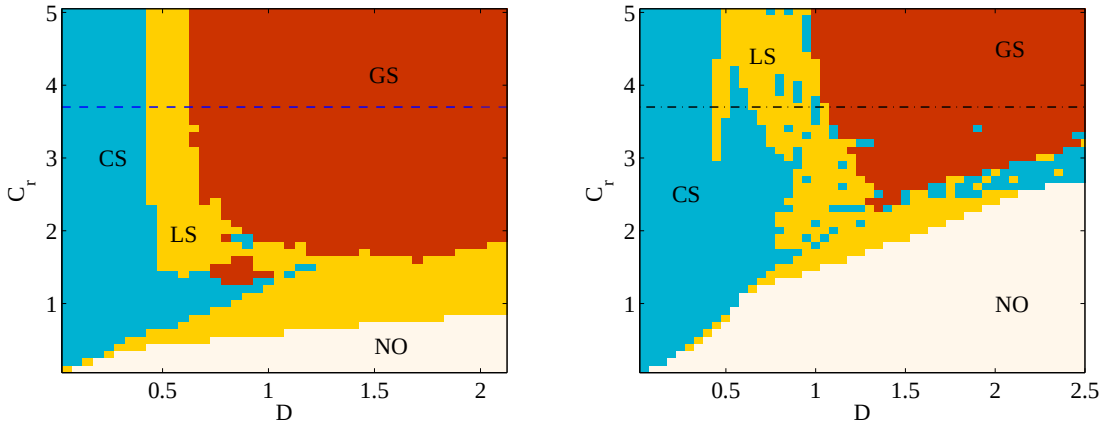

(a) Replica 1 (b) Replica 2

Figure 5.2: (a,b) : Phase diagrams for $f = 0.5$ in two systems of size $N = 50^2$ with different replicas. Every point was evolved out of random, hence different, initial conditions. Horizontal dashed line represents the value of C_r^0 such that $f_c^1(C_r^0) = f$. Below this line the system is subcritical according to the 0-d analysis and no oscillation exist for $D \to \infty$.

particular, it is seen that a globally coupled (GS) state can be observed for values of C_r much smaller than the critical value $C_r^0 = 3.7$, below which no oscillations are observed in the 0-D model.

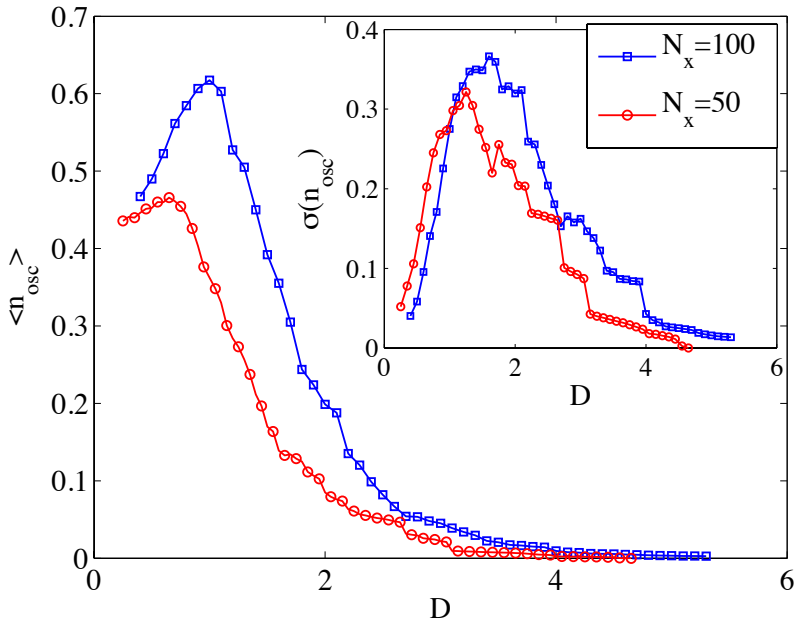

Figure 5.3: Averaged value of the fraction of oscillating cells $\langle n_{osc} \rangle$ for system sizes $N_x = 50$ and $N_x = 100$. Each point is obtained by averaging over 200 replicas. $C_r = 1, 9$, $f = 0.5$, $\mu = 5.7 \times 10^{-2}$.

The general aspect of the phase diagrams shown in Fig. 5.2, is very reminiscent of the corresponding phase diagram shown in Chapter 4, Fig. 4.15, obtained in a system of size $N_x = 100, f = 0.5$. By comparison, it can be noticed that the boundary separating CS and GS shifts toward smaller D. This suggests a size dependence of the system behavior. To characterize this size dependence, we have carried out simulations, as done in section 4.1.5, on systems of small size $N_x = 50$, with the same value of f. The value of n_{osc} was determined for at least 200 replicas. The average of n_{osc} is shown in Fig. 5.3. In addition to the value shown in Fig. 4.18 with $N_x = 100$ (blue diamonds), we also show values obtained for $N_x = 50$ (red open squares). Fig. 5.3 shows that, as the coupling coefficient D increases, the average number of oscillating cells in the system decreases, and eventually reaches zero. This is consistent with the 0-D analysis. The high values of the standard deviation, shown in the inset, reveals strong replica–to–replica dependence.

Despite these similarities, a clear difference can be observed: oscillations vanish at larger values of D for larger systems. This size dependence will be analyzed more thoroughly in the following section.

5.3 Fluctuations of passive cell density and local activity

The behavior described in the previous section can be qualitatively understood by noticing that diffusion effectively couples excitable cells which are within a distance $\propto \sqrt{D}$. As a consequence, one may expect that a given excitable cell is sensitive not so much to the passive cells that are directly coupled to it, but more to all the cells that are within a distance $\propto \sqrt{D}$ from this cell. This suggests to relate the observed activity of a cell in the system to the fluctuations of the density of passive cells in a domain surrounding the cell.

5.3.1 Averaging procedure

With this motivation, we begin by defining how we computed the local density of passive cells surrounding a given excitable cell. We define the local passive density $\bar{n}_d$, coarse-grained over a scale d as the convolution $\bar{n}_d = K_d * n$ of the initial distribution of passive cells $n_p^{i,j}$ with a 2-dimensional averaging kernel $K_d(i,j)$. The kernels we have considered are all separable, in the sense that $K_d(i,j) = k_d(i/d) \times k_d(j/d)$.

Because the coupling term is effectively described by a Laplacian term, a natural choice for the coarse-graining kernel K_d is the Gaussian kernel, obtained with k_d^G given by:

$$k_d^G(i) = \frac{1}{\sqrt{2\pi d^2}} \exp(-\frac{i^2}{2d^2}) \,, \tag{5.2}$$

For the analysis discussed below, it is also convenient to consider the simpler "top hat" square kernel, k_d^{TH}, defined by:

$$k_d^{TH}(i) = \frac{1}{d} H(|i - d/2|) \,. \tag{5.3}$$

where, $H(x)$ is the Heavyside function, defined as $H(x) = 1$, for $x>0$, and $H(x) = 0$ otherwise. In this latter case, $\bar{n}_d(i,j)$ is simply the number of passive cells, averaged over a square subregion of size $N_d = d^2$ centered at the point (i,j). In the case of the Gaussian kernel K_d^G, the contribution from a site (i',j') to n_p at site (i,j) depends on the distance between the two. The variance of $\bar{n}_d$ can be written as $\sigma_d^2 = \sigma^2/N_d$, where σ^2 is the variance of n_p, and N_d $(= 4\pi d^2)$ is the effective number of sites contributing to $\bar{n}_d$.

The numerical study of the problem, discussed in the rest of this section, has been carried out by using the Gaussian kernel; the top hat kernel will be useful for the theoretical analysis, presented in section 5.4.

5.3.2 Pacemaker-like regions and diffusion

The third line of Fig. 5.1 shows how the passive cell density $\bar{n}_d$ evolves when d is increased. The patterns of $\bar{n}_d$ and of the oscillation amplitude are clearly similar. As can be seen in Fig. 5.1, oscillations are located in regions which correspond to the largest local passive cell density. In addition, we observe that increasing the diffusion coefficient D and increasing the size d lead to similar effects. In fact, increasing D eventually leads to a reduced number of oscillating cells, a consequence of the fact that in the regime investigated in Fig. 5.1, the value of f is lower than the critical value f_0 at very large values of D. In the same spirit, by increasing d, the coarse-graining size, the variance of $\bar{n}_d$ decreases, therefore reducing the variations of the local density of passive cells connected to excitable cells in the system.

To go beyond the qualitative impression given by Fig. 5.1, we define a "pacemaker-like region" as a set of adjacent cells with a local density $\bar{n}_d$ larger than the critical value $f_c^1(C_r)$. The analysis carried out for a single cell (0-D) suggests that these cells are the ones that will lead to oscillation. The number of pacemaker-like regions depends both on the replica and on the coarse-graining length d; this number decreases when d increases, and becomes 0 as d becomes very large.

For a given replica, we look for the smallest value of d, d^* above which the number of pacemaker-like regions in the system is zero. We can then relate this value of d^* to the value D^* of the diffusion coefficient above which the number of oscillating cells in the system vanishes.

The results are presented in Fig.5.4. Each point corresponds to one replica. Several system sizes have been studied, as indicated by the symbols (see the caption). We observe that d^{*2} and D^* are close to being proportional: $d^{*2} \approx TD^*$; $T = 36.6$ being a typical time of the system. The characteristic time $T = d^{*2}/D^*$ is of the order of the slow time scale of the system, $\sim 1/\epsilon$. In fact, the measured value, $T = 36.6$ is in the middle of the range of observed period of oscillations, which from 40 down to 31 when D is increased in a 50×50 system). We do not have any convincing explanation relating T to the oscillation period..

A very important observation from Fig.5.4 is that both D^* and d^* increase when the size of the system increases: the larger the size of the system, where $f \leq f_c^1$, the larger the range of values of D over which oscillations can be seen. Quantifying the size dependence is the object of section 5.4.

5.4 Statistical description

The relation between clusters of oscillating cells and regions containing pacemaker-like regions, suggested by Fig. 5.1, and also by the proportionality between the values of D^* and d^* (see Fig. 5.4) suggests that the fluctuations observed when considering different replicas can be simply understood by investigating the presence of pacemaker-like regions as a function of the coarse-graining size d.

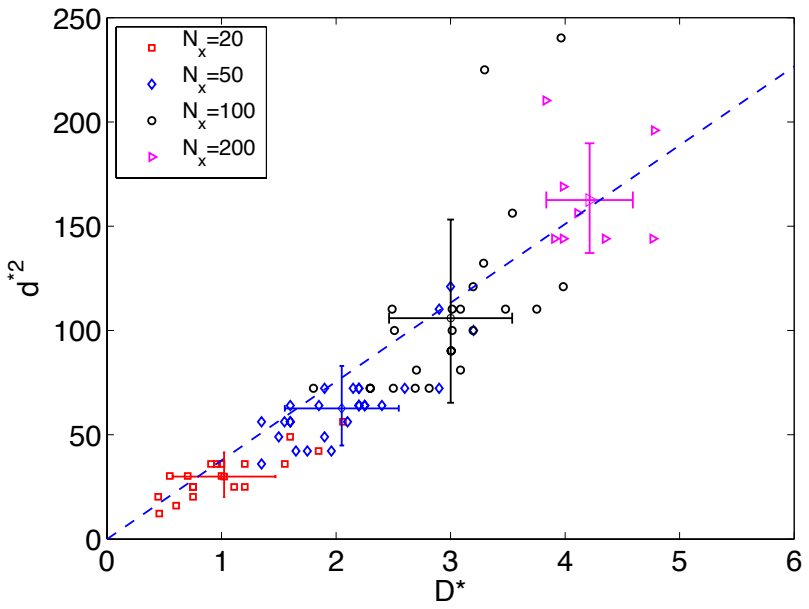

Figure 5.4: Relation between the largest values of coarse-graining length d^* and diffusion coefficient D^* for which a given 2D system possesses regions with oscillatory activity. Each point corresponds to a different replica whereas different symbols represent different system sizes $N = N_x^2$. Error bars centered around averages of replicas for the same system size express the standard deviation. The linear fit between d^{*2} and D^*, shown as a broken line, has a slope $T \simeq 36.6$ that lies in the middle of the range of observed oscillation periods (lying between 31 and 40) for different values of the diffusive coupling strength in a 2D system with $N_x = 50$

In this spirit, in order to understand the main features observed numerically, we analyze here the effect of coarse-graining on the existence of pacemaker-like regions. To simplify the analysis of the coarse-graining process, our analysis is carried out first with the square kernel introduced above, see Eq. (5.3).

5.4.1 Distribution of passive cells

The probability of having N_p passive cells in a region of $N_d = \nu N$ excitable cells, knowing that there is a total of $M = f \times N$ passive cells randomly distributed in a system of $N = N_x^2$ excitable cells, is given by the binomial distribution

$$p^N(N_d, N_p) = C_M^{N_p} \nu^{N_p} (1-\nu)^{M-N_p}\,, \tag{5.4}$$

which reduces when $N \to \infty$ to a Poisson distribution of parameter fN_d :

$$p^{\infty}(N_d, N_p) = \frac{(fN_d)^{N_p} e^{-fN_d}}{N_p!} \tag{5.5}$$

independent of the system size N. For a top hat kernel, the averaging occurs over $N_d = d^2$ sites where d is the coarse-graining length and the local passive cell density $\bar{n}_d = N_p/N_d$.

5.4.2 Probability of having a pacemaker-like region in a subset of N_d cells

Given the probability mass function of passive cells, we write the probability that a cell (i, j) in the center of a region of N_d cells has an effective passive cell density $\bar{n}_d(i, j) = N_p/N_d \geq f_c^1$, *i.e.*, larger than the critical value. In that case, we expect that the corresponding averaging region of size N_d around the center cell (i, j) will behave, at least close to (i, j), as a pacemaker-like region. We have

$$\begin{aligned} P^N(N_d) &= \sum_{N_p=f_c^1 N_d}^{M} p^N(N_d, N_p) \\ &= \sum_{N_p=f_c^1 N_d}^{M} \frac{M!}{N_p!(M-N_p)!} \nu^{N_p} (1-\nu)^{M-N_p} \\ &= I_\nu(f_c^1 N_d, fN - f_c^1 N_d + 1) \end{aligned} \tag{5.6}$$

where $I_x(a, b)$ is the regularized (incomplete) beta function [148]. $P^N(N_d)$ depends on the system size N but for large $N \to \infty$ it tends to a regularized incomplete gamma function that does not involve the system size N anymore:

$$\begin{aligned} P^N(N_d) \to P^{\infty}(N_d) &= \sum_{N_p=N_c}^{\infty} \frac{(fN_d)^{N_p} e^{-fN_d}}{N_p!} \\ &= (fN_d)^{N_c} e^{-fN_d} \sum_{N_p=0}^{\infty} \frac{(fN_d)^{N_p}}{(N_p-1)!} \\ &= \frac{\gamma(f_c^1 N_d, fN_d)}{(N_c-1)!} \end{aligned} \tag{5.7}$$

where $\gamma(a, b)$ is the incomplete gamma function, defined as $\gamma(a, b) = \int_0^b t^{a-1} e^{-t} dt$ [149].

To verify our analysis, we measure the probability of having a pacemaker-like region in the subregion N_d as the following: for a given replica, we first compute the average passive cell density by applying the average process Eq.5.2 and Eq.5.3 for Gaussian and square kernels, respectively, with length d. We then ask whether

the center of a region of size N_d having $\bar{n}_d(i,j)$ larger than f_c^1 for Gaussian (square) kernel. To get a good statistics, we took four well separated regions (the four corners) in each replica. We repeated this procedure for 200 different replicas. Then $P^\infty(N_d)$ can be expressed as the total number of the observations of pacemaker-like regions divided by 4×200. Fig. 5.5 shows a comparison between the numerically measured probabilities and those obtained using the above expressions. Although Eqs. (5.6) and (5.7) are assuming a simple local average as the one given by the convolution with the square kernel (5.3), they also represent perfectly the measurements of the passive cell density obtained by convolution with the Gaussian kernel (5.2), as can be seen in Fig. 5.5.

In the limit of large system sizes N, we can rewrite $P^\infty(N_d)$ by factorizing the first term of the sum in Eq.(5.6) :

$$P^\infty(N_d) = p^\infty(N_d, f_c^1 N_d) \sum_{k=0}^{\infty} \prod_{p=1}^{k} \frac{f N_d}{f_c^1 N_d + p},$$

and then use a Stirling expansion for the first term, while we rewrite the products by keeping only lower order terms in $1/N_d$ in the large N_d limit. Further neglecting

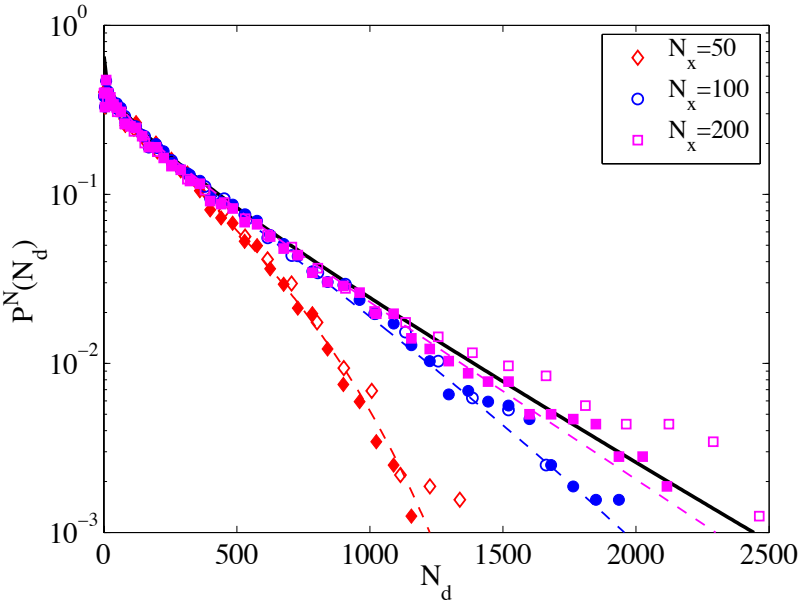

Figure 5.5: Probability $P^N(N_d)$ of having local passive cell density greater than f_c^l in a neighborhood of N_d excitable cells as a function of N_d. Open (filled) symbols represent numerical observations using Gaussian (square top hat) kernel. The broken curves indicate the corresponding probabilities obtained from the analytical expression of $P^N_{N_d}$, Eq. (5.6). The solid curve shows $P^\infty_{N_d}$, the probability values obtained for infinitely large system, Eq. (5.7).

$\nu = N_d/N$, we obtain for any fixed value of μ:

$$P^{\infty}(N_d) \simeq \frac{1}{\sqrt{2\pi f_c^1 N_d}} \frac{\mathrm{e}^{-\lambda f_c^1 N_d}}{\mu} \tag{5.8}$$

where we defined $\lambda = -\mu - \ln(1-\mu)$. To obtain an expression valid for arbitrarily small μ, we remark that $\lambda \simeq \mu^2/2 > 0$ and we use the variable $\mathcal{X} = \mu^2 f_c^1 N_d$ to write:

$$P^{\infty}(N_d) \simeq \frac{1}{\sqrt{2\pi\mathcal{X}}} \mathrm{e}^{-\frac{\mathcal{X}}{2}} \tag{5.9}$$

5.4.3 Probability of having a pacemaker-like region in the system

Fig.5.1 suggests that that oscillations are induced by the presence of one, or several pacemaker-like regions in the system. A reasonable assumption is that pacemaker-like regions are able to entrain a fraction of the system. The dependence of the probability of obtaining a pacemaker-like region in the system on the system size can be simply understood from the following considerations. Consider two systems of sizes N_1 and N_2 ($N_1 > N_2$), with the same amount of average passive cells, expressed by the

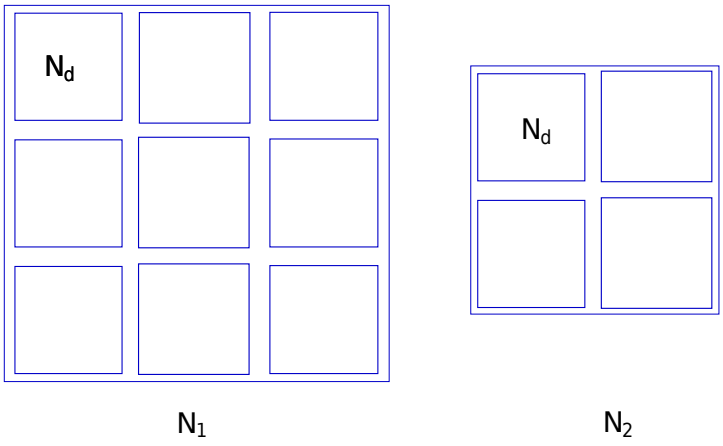

Figure 5.6: Size effect on the pacemaker fraction. Each subregion N_d has the same probability of being a pacemaker p_o. For the N_1 system, its probability of having non-zeros pacemaker fraction is $1-(1-P^N(N_d))^{\frac{N_1}{N_d}}$, and $1-(1-P^N(N_d))^{\frac{N_2}{N_d}}$ for the N_2 system.

fraction f. As a given coarse-graining scale d, or equivalently, at a given value of the coupling between excitable cells D, the larger system contains a larger number of independent subregions N_d, as illustrated in Fig.5.6. The probability of having at least one pacemaker region in a system containing $\eta = N/N_d$ non-overlapping subregions can be expressed as:

$$\Pi^N(N_d) = 1 - \Big(1 - P^N(N_d)\Big)^{\eta} \tag{5.10}$$

Since $1 - P^N(N_d) < 1$, Equ. 5.10 indicates that larger system has higher probability of having pacemaker-like regions at a given d, hence oscillations sustain for larger values of D.

Supposing that the system is indeed composed of non-overlapping subregions of size N_d, the probability of finding at least one pacemaker-like region $\Pi^N(N_d)$ is fully determined by Eq. 5.10, which is plotted in Fig. 5.7 for different system sizes with solid lines. To verify our analysis, we first computed the probability of a system $(N_x \times N_x)$ composed of non-overlapping subregions N_d having at least one pacemaker-like region numerically. As shown previously, the probability is independent on the shape of the kernel, as long as the proper sizes of subregion are taken(gaussian: $N_d = 4\pi d^2$, square: $N_d = d^2$). For simplicity, the square kernel was used. Numerically, we compute the average passive cell density map n_d using a square kernel of size N_d. The system is then divided into $\eta = (\text{int}(N_x/d))^2$ independent subregions of size N_d. We then search for the maximum value $(\bar{n}_d^m)$ of the central points of the η subregions. If $\tilde{n}_d^m$ larger than f_c^1, we put 1, and 0 otherwise, *i.e.,*

$$\begin{array}{ll} 1 & \text{if} \quad \bar{n}_d^m \quad \geq f_c^1, \\ 0 & \text{otherwise} \end{array} \tag{5.11}$$

Here $\text{int}(x)$ gives the integer part of x. The average over 400 realizations of the step function Eq.5.11 associated to N_d gives the probability of finding at least one pacemaker like regions in the system composed of η independent subregions of size N_d, which is plotted in Fig.5.7 with filled symbols. By taking into account the residual, *i.e.,* $n = \text{int}(N_x/d)^2$, Eq.5.10 is consistent with numerical measurements.

Oscillations are expected to vanish when $\Pi^N(N_d)$ is less than $1/2$, which gives the critical values of N_d^* =542, 1094 and 1887 for systems of size $N_x = 50, 100$ and 200 respectively. Using the relation $d^{*2} = TD^*$ obtained from Fig. 5.4, oscillations are expected to vanish at values of $D^* = 1.2, 2.3$ and 4.1. We found that these values are much smaller than the ones measured for the corresponding systems, suggesting that the non-overlapping gives an underestimation of the probability. Indeed, as stated before, oscillations emerge as long as there is a pacemaker-like region, wherever it is in the system. Eq.5.10, by taking N/N_d independent subregions N_d, which does not count properly all possible pacemaker-like regions, is an underestimate $\Pi^N(N_d)$. On the contrary, using exponent N instead of η would over-estimate the probability $\Pi^N(N_d)$ because of correlations in overlapping subregions. To well describe $\Pi^N(N_d)$,

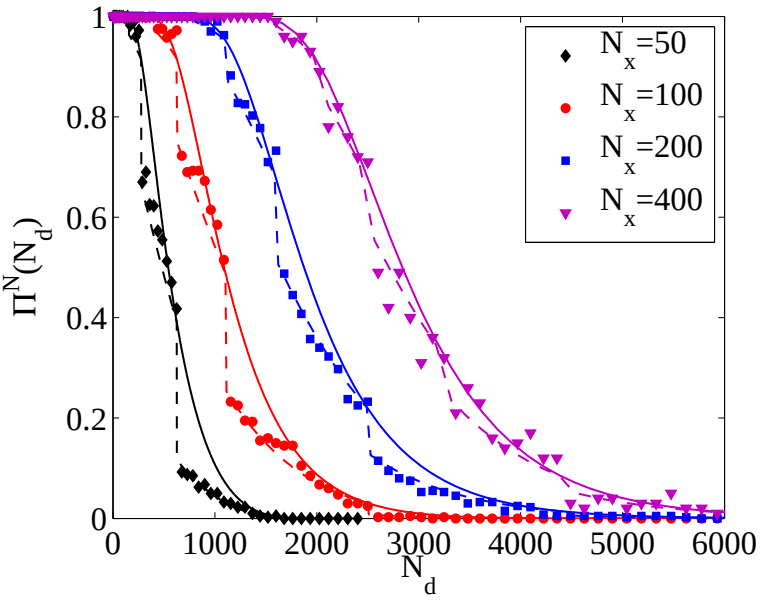

Figure 5.7: The probabilities of having at least one pacemaker-like region in systems containing non-overlapping subregions. Symbols: numerical measurement with square kernel. Lines: theoretical estimation from Eq.5.10

we introduce parameter m. Combined with N/N_d, it gives the effective number of independent subregions:

$$\Pi^N(N_d) = 1 - \left(1 - P^N(N_d)\right)^{m\frac{N}{N_d}} \tag{5.12}$$

gives the probability of having at least one pacemaker-like region in the entire system.

From the numerical point of view, applying the same procedure of Eq.5.11 with the step function that gives 1 when $\max(\bar{n}_d(i,j)) \geq f_c^1$ and 0 otherwise, we get a direct measurement of $\Pi^N(N_d)$. A single step function vanishes for $N_d^* = 4\pi d^{*2}$ where d^* is the value plotted in Fig. 5.4 for the corresponding replica. Averaging over replicas gives a smooth sigmoid-shaped curve, as plotted in Fig. 5.8 as open symbols.

We experimentally measure the effective number (mN/N_d) of independent subsets, so that we can reproduce reasonably well the experimental observations, as can be seen on Fig. 5.8. The value of m is obtained by a least-square fit of numerical curves by the analytical expression Eq. (5.12). We obtain a value of m that has no clear dependence on the system size, which can easily be understood as follows. Consider the covariance of the two variables, $f_d(i,j) = N_p(i,j)/N_d$ and $f_d(i',j')$, i.e., of the average number of passive cells at the two sites (i,j) and (i',j') separated by a distance $l = \sqrt{(i-i')^2 + (j-j')^2}$. It has the exact expression $\sigma\rho(l)/N_d$ where $\sigma = (1-\nu)f$ and $\rho(l) = \exp[-(l/2d)^2]$ is the correlation between the two sites. Thus, how fast the two values of f_d decorrelate is simply given by $\rho(l)$. To estimate the number of

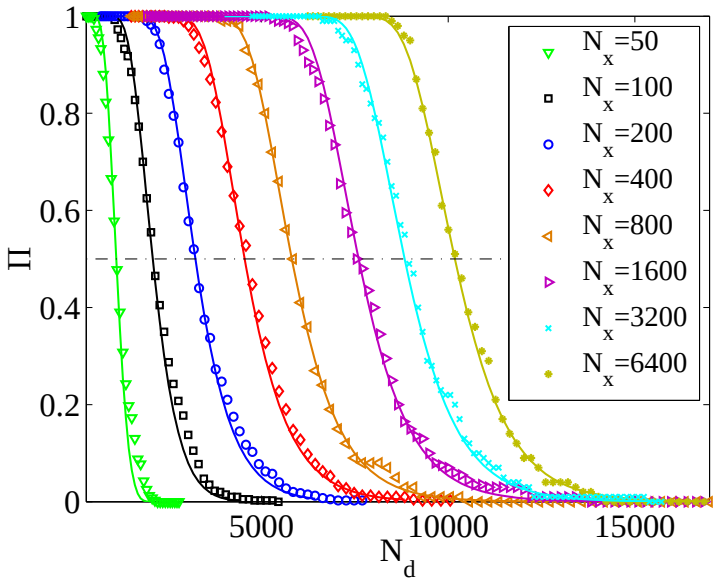

Figure 5.8: Probability of having at least 1 pacemaker-like cell in a system of size $N = N_x^2$ as a function of the number of points N_d under the Gaussian kernel. Different symbols are for different systems size from $N_x = 50$ to 6400, and continuous lines are fits described further in the text.

independent subsets containing N_d points, we introduce κ, defined as the maximum possible correlation between two independent subsets. The correlation length l_0 is then defined by $\rho(l_0) = \kappa$, so that two subsets separated by a distance $l > l_0$ are independent. This implies the existence of N/l_0^2 independent blocks, suggesting in turn that $m = N_d/l_0^2$. Intuitively, one expects l_0 to be of the order of the width of the Gaussian kernel, d, yielding $m \approx 4\pi$. We have numerically obtained the effective number m by least-square fitting of the numerical data shown in Fig. 5.8 with the theoretical expression of Eq. (5.12). This gives values of m lying in the range $9.5 \leq m \leq 16.5$, which is in fact consistent with the heuristic estimate $m = 4\pi$.

5.4.4 System size dependence

From the curves in Fig. 5.8, we define N_d^*, the largest size of the pacemaker region in a system of N excitable cells, and therefore the value of the diffusion coefficient at which oscillations disappear in the system, resp. d^*, as the value of N_d, resp. d, for which $\Pi(N_d^*) = 1/2$. These quantities are defined by averaging over many replicas, for a given system size N. The larger the system size, the larger the probability for a fixed value of N_d. This property is consistent with our previous observation that larger systems sustain oscillations for larger values of D, see (Fig. 5.3).

Fig.5.9 shows the measured values of N_d^*(open circles) for different system sizes. By using the relation $D = Td^2$, with T = 36.6 (see section 5.3.2), we also obtain a measurement using data from Fig.5.4, plotted with open circles. Theoretically, the value of N_d^* is the solution of:

$$\Pi^N(N_d^*) = 1 - \left(1 - P^N(N_d^*)\right)^{m\frac{N}{N_d^*}} = 1/2 \tag{5.13}$$

where m accounts for the effective number of independent subregions. To solve this equation, we assume that the system is large enough such that $P^N(N_d^*)$ is independent of N, and we use the expansion of $P^\infty(N_d^*)$ given by Eq. (5.8). Consequently, the only dependence of $\Pi^N(N_d)$ in N comes from the exponent mN/N_d in Eq. (5.13).

We obtain a linear relation between $\ln(N)$ and N_d^*, reproduced in Fig. 5.9. Neglecting additional logarithmic corrections, one obtains:

$$\mu^2 f_c^1 N_d^* = 2\log N + 2\log \frac{\mu^2 f_c^1 m}{\log(2)\sqrt{2\pi}} \tag{5.14}$$

Eq. 5.14 effectively defines N_d^*. For large systems, the behavior of N_d^* is well described

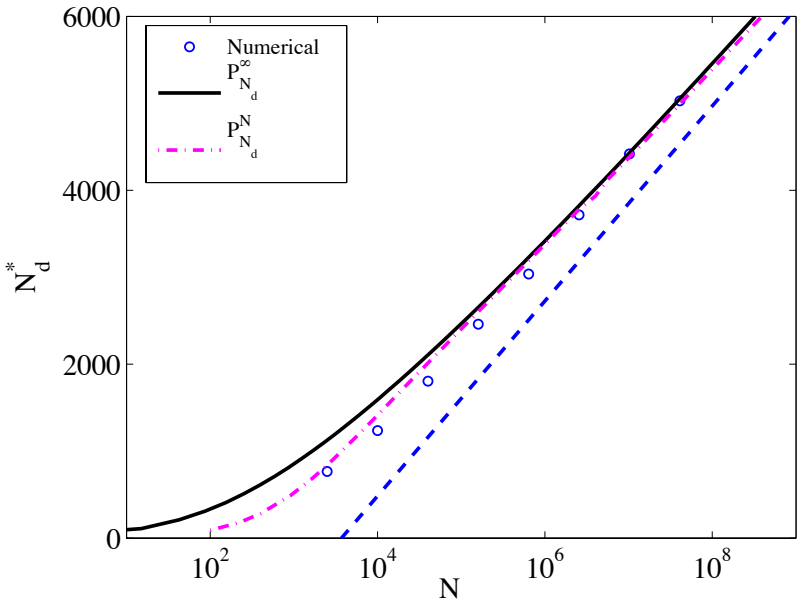

Figure 5.9: The largest coarse-graining size for which oscillations are observed in the system, N_d^*, defined as $\Pi = 1/2$, as a function of the system size N. The circles represent numerical data shown in Fig. 5.8. The dashed straight line is a guide to the eye indicating the slope $1/(\lambda f_c^l)$. The solid line and dashed-dotted line represent the solutions of Eq. (5.13) using the expressions given by Eq. (5.6) and Eq. (5.7) respectively.

by the $\log(N)$ tern in Eq. 5.14, shown by a straight line in Fig.5.9. Deviations from the $\log(N)$ scaling are observed for $N \lesssim 10^4$. They can be capture by the constant term in the R.H.S. of Eq. 5.14. It is worth noticing that the $\log(N)$ scaling appears very naturally in the general context of extreme value statistics.

5.5 Discussion

5.5.1 Influence of the mean passive cell density

In the 0-d system, the average passive cell density f plays the same role as C_r, whereas in 2-d system n_p gets averaged by diffusion. The analysis presented in the previous sections, in particular Eq.5.14 allowed us to identify a characteristic coarse-graining size, which determines the existence of pacemakers in a system of size N. Our analysis suggests that the number of pacemaker cells in a given system is determined by the ratio N_d/N_d^*. The relation $N_d = 4\pi d^2 = 4\pi TD$ allows us to relate the diffusion to the appearance of pacemaker cells in a given system. As the existence of pacemakers is related to the appearance of oscillations in the system, the averaged fraction of oscillating cells is suggested to be a function of $4\pi TD/N_d^*$.

Fig.5.10 shows the average and the standard deviation of the oscillating cell fraction at fixed values of μ, D and N_x. Remarkably, all the curves collapse within the error bars in the region where our analysis is valid. This provides a strong evidence that the properties of the system indeed are a function of $\mu^2 D/N_d^*$.

5.5.2 Influence of the law of probability of the passive cell distribution

We notice that in Fig.5.10 the scaling law is not valid at small values of N_d. This results from our particular choice of passive cell distribution. During the numerical simulation, the way we chose to distribute the passive cells coupled to the excitable cells in the system was dictated by the constraint of having a constant mean fraction $f = mean(n_p)$, the averaging being over all cells for a given replica. Using a Poisson distribution of passive cells does not fulfill this requirement, because for a Poisson distribution, the mean fraction f depends on the replica. For this reason, we used a binomial distribution in the numerical simulations. While for the reason of simplicity, we used poisson distribution in the theoretical analysis. In the limit of large system size, both the binomial and Poisson distributions give the same behavior, which is a consequence of the fact that the fluctuations of the total number of passive cells in the Poisson case are small, when N is large. However, for intermediate system sizes, using the Poisson distribution introduces biases due to the fluctuations of the number of passive cells, therefore modifying our predictions: the scaling in $\mathcal{X} \approx N_d\mu^2$ has to be corrected by terms of the order $\nu = N_d/N = 4\pi TD/N$. This effect can be seen in Fig. 5.3, where size effects are due to the choice of system size. Our values of N

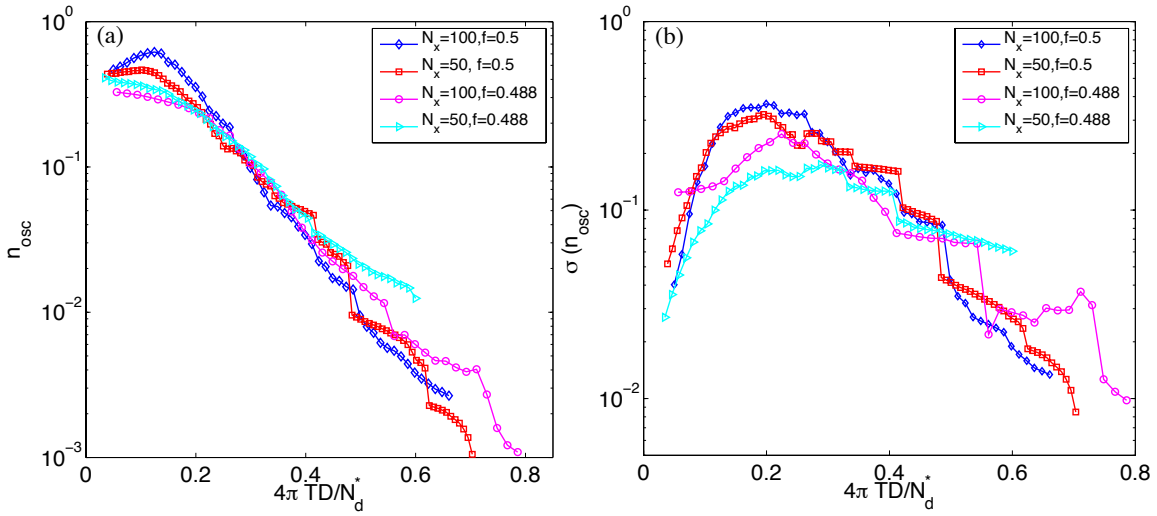

Figure 5.10: Averaged value and standard deviation of the fraction of oscillating cells in a 2D system as a function of the reduced variable $4\pi TD/N_d^*$, where N_d^* is defined in Eq.5.14. The symbols indicated in the legend correspond to different values of N_x and f, *i.e.,* N and μ. The different curves all collapse, within the error bars in the region where our analysis is valid.

are not large enough : from Fig. 5.5, we see that system size 50^2 and 100^2 are very far from the asymptotic Poisson regime, and so they are for the order parameter $n_{\rm osc}$. As already stated, this difference vanishes as the system sizes are increased.

5.6 Conclusion

We have explored the effect of diffusion on the the spatial distribution of passive cells and its effect on the observed activity of the system. This has been achieved by several steps. Based on the *zero*-D analysis introduced in Section 3.2, our first step has consisted in relating the role of coupling between excitable cells to spatial filtering of the passive cell distribution, and then, in connecting the disappearance of oscillating cells and of pacemaker-like regions. As a second step, we have applied the results of the *zero*-D analysis to ensemble averages of replicas, to estimate the fluctuations of the local density of passive cells, thus effectively measuring the size of pacemaker-like regions. By using the natural assumption that the effect of the diffusion coefficient D is to average the information over N_d cells, we estimated $D = d^2/T = N_d/T'$. We quantified the influence of the system size as facilitating the existence of oscillations and showed that this effect is logarithmic in N.

As a consequence of these properties, governing the probability to observe pacemaker-like regions in the system, we have establised the dependence of the transition towards a regime of activity as a function of the size N of the system. The $\log(N)$ scaling of

the control parameter is observed both for very large systems (Poisson distributions) and intermediate systems sizes (binomial distribution). Although when integrating Eq.(4.1) in 2-d systems, we have indeed always used moderate system sizes, for computational time issues, our results provide convincing evidence that the $\log(N)$ dependence is indeed appropriate to describe the transition to a regime of spontaneous activity.

Chapter 6

Conclusions and future work

In this chapter, we first briefly summarize the main achievements of this thesis, and present some possible extensions of our work for the future.

6.1 Conclusions

The pregnant uterus is a unique organ in many aspects. The most surprising one is the observation of a change of the organ shortly before labor, from a quiescent tissue to a state with intense rhythmic contractions, capable of expelling the newborn. The aim of this thesis was precisely to provide some understanding of the mechanisms underlying this transition. To this end, we used a modeling approach. We have focused on the electric activity, which is known to act as a precursor of the mechanical activity.

6.1.1 Uterine myocyte models

First of all, a description of the main ionic channels of the uterine myocytes, in the spirit of the Hodgkin-Huxley model, has been presented.

The first model we used has been developed by Rihana *et al.* [43]. It incorporates five classes of ionic channels (sodium, potassium, calcium, calcium activated potassium and leakage), and has been validated with respect to most known electrophysiological (voltage clamp) experiments. The differences observed between the model and the experiments are due, to a large part, to a lack of a precise measurement of the calcium channel kinetic. However, they are confined to large values of the high membrane potential, which are outside of the range of membrane potential in natural conditions.

The second model is based on the recent work of Tong *et al.* [44], which considers the influence of 14 different ionic channels. The main modification that we have introduced concerns the Na^+– Ca^{2+} exchanger. This exchanger brings one Ca^{2+} out at the cost of an influx of three Na^+, which gives rise to a net inward current. This current tends to depolarize the membrane potential (make it more positive). While in the

original model, this current tends to hyper-polarize the membrane potential, leading an unrealistic resting state and an extremely high intracellular calcium concentration at physiological conditions. After introducing the modifications, we have verified that the modified model reproduces well the experimental recorded signals under realistic physiological conditions.

The second class of model is based on a generic model of excitable cells. Namely, we took the well-known FitzHugh-Nagumo model, which is known to provide a qualitative description of most phenomena involving excitable cells. We generally found a good qualitative agreement between predictions based on the more precise models and those based on the simple FitzHugh-Nagumo model.

6.1.2 Uterine activities

We took the strong change in the expression of gap junctions, observed during the late stage pregnancy as a hint that electric coupling plays a crucial role in the transition to a regime of oscillations. We thus proposed that oscillations are induced by the increase in the coupling between myocytes, and between myocytes and passive cells. We have studied this hypothesis using our models, based on the description of myocytes introduced in Chapter 2.

We have first shown that oscillations can spontaneously occur when taking a myocyte, coupled to a passive cell, and increasing the electrical coupling. This behavior is common to all myocyte models.

We have then extended our study to a simple model of tissue, consisting of excitable cells coupled together on a lattice, each of the excitable cell being coupled to a varying number of passive cells. We observe a transition to a coherent oscillatory activity. In the case of the simple FitzHugh-Nagumo model, we fully characterize the transition numerically. Our study based on a more realistic model of myocytes confirms qualitatively the results obtained with the FitzHugh-Nagumo model. In addition, the model does reproduce the bursting activity observed in recent experiments [141]. We view these features as evidence supporting our hypothesis concerning the role of the coupling in the transition towards oscillations in the tissue.

With the simple FitzHugh-Nagumo model, we also elucidate analytically certain aspects of the transition, in particular, those concerning the large fluctuations observed when varying the distribution of passive cells attached to myocytes in the tissue. A statistical (counting) argument allows us to characterize the relevant fluctuations of the density of the passive cell when the coupling between myocytes is varied, and allows us to derive a simple scaling relation for the appearance of activity in the system.

6.2 Future work

We have shown that the modified Rihana's model, whose description of the ion channels are mainly based on experimental work done by Yoshino and Wang [33, 34], could recover most of the experimental data, but there were deviations, especially in the higher range of membrane potential. The access to more precise experimental data allowed Tong and his coworkers to build a uterine myocyte model that reproduces better the experimental signals. Due to the complexity of living systems, and sample to sample fluctuations during the experiments, more precise description of the ion channels are still needed. Although not expected to influence uterine excitable dynamics qualitatively, more channel informations would be expected to influence the threshold of the excitability. Moreover, this would allow us to investigate the influence of electro-physiological changes more precisely.

Hormonal activity is known to play a crucial role during pregnancy [150]. Hormones induce changes, which are crucial for the maintenance of the pregnancy, and for the expulsion of the new-born. *In-vitro* experiments also show that some hormones can inhibit uterine contractions [150]. Understanding at what level, in the model developed here, do hormones affect the myocytes is a very important question. It is very likely that the effect of the coupling discussed here is in fact complemented by some action of hormones before delivery. These questions are particularly relevant for potential pharmaceutical developments.

Throughout this work, we have made the assumption that the random distribution of passive cells is statistically homogeneous throughout the tissue. Our results show that electrical activity starts in regions with a high passive cell density. In reality, uterine contractions are directed from the fundus towards the cervix. A possibility would be that the density of passive cells is higher close to the fundus. On the other hand, Young *et al.* suggest that the functional units in the uterus are myocytes bundles [49]. The effect of the geometric structures in connection to the phenomena studied here remains to be elucidated.

Ultimately, labor involves a strong force to expel the new-born. Although it is well known that the contractile force of smooth muscle cells is directly related to the underlying changes of membrane potential, the question of which mechanism generates the force has not been well addressed yet. Indeed, this has attracted scientific effort. Models, such as the Cross-Bridge phosphorylation and latch-state model proposed by Hai and Murphy [151] have been applied to describe the contractile force generated by a single myocyte [44, 78], with a maximum value about 3μN. Taking the size of each uterine myocyte, an estimation of the uterine wall tension is about 0.1N/cm^2.

Bibliography

[1] A. Goldbeter, "Biological rhythms: Clocks for all times," *Current Biology*, vol. 18, no. 17, pp. R751–R753, 2008.

[2] N. Brunel and V. Hakim, "Fast global oscillations in networks of integrate-and-fire neurons with low firing rates," *Neural Comput.*, vol. 11, pp. 1621–1671, March 1999.

[3] M. U. Gillette and T. J. Sejnowski, "Biological clocks coordinately keep life on time," *Science*, vol. 309, no. 5738, pp. 1196–1198, 2005.

[4] C. I. Eastman and H. J. Burgess, "How to travel the world without jet lag," *Sleep Med Clin.*, vol. 4, no. 2, pp. 241–255, 2009.

[5] R. W. Tsien, R. S. Kass, and R. Weingart, "Cellular and subcellular mechanisms of cardiac pacemaker oscillations," *Journal of Experimental Biology*, vol. 81, no. 1, pp. 205–215, 1979.

[6] M. Golubitsky, I. Stewart, P.-L. Buono, and J. J. Collins, "Symmetry in locomotor central pattern generators and animal gaits," *Nature*, vol. 401, pp. 693–695, October 1999.

[7] S. M. Reppert and D. R. Weaver, "Coordination of circadian timing in mammals," *Nature*, vol. 418, pp. 935–941, August 2002.

[8] A. L. Hodgkin and A. F. Huxley, "The dual effect of membrane of potential on sodium conductance in the giant axon of loligo," *Journal of Physiology*, vol. 116, pp. 497–506, 1952.

[9] R. FitzHugh, "Impulses and physiological states in theoretical models of nerve membrane," *Biophysical Journal*, vol. 1, pp. 445–466, 1961.

[10] G. W. Beeler and H. Reuter, "Reconstruction of the action potential of ventricular myocardial fibres," *The Journal of Physiology*, vol. 268, no. 1, pp. 177–210, 1977.

[11] C. H. Luo and Y. Rudy, "A model of the ventricular cardiac action potential. depolarization, repolarization, and their interaction.," *Circulation Research*, vol. 68, no. 6, pp. 1501–26, 1991.

[12] C. Luo and Y. Rudy, "A dynamic model of the cardiac ventricular action potential. i. simulations of ionic currents and concentration changes," *Circulation Research*, vol. 74, no. 6, pp. 1071–1096, 1994.

[13] K. H. W. J. ten Tusscher, D. Noble, P. J. Noble, and A. V. Panfilov, "A model for human ventricular tissue," *American Journal of Physiology - Heart and Circulatory Physiology*, vol. 286, no. 4, pp. H1573–H1589, 2004.

[14] S. Luther, F. H. Fenton, B. G. Kornreich, and A. S. et al., "Low-energy control of electrical turbulence in the heart," *Nature*, vol. 475, pp. 235–239, 2011.

[15] M. F. Klemm, B. Exintaris, and R. J. Lang, "Identification of the cells underlying pacemaker activity in the guinea-pig upper urinary tract," *The Journal of Physiology*, vol. 519, no. 3, pp. 867–884, 1999.

[16] N. McHale, M. Hollywodd, G. Sergeant, and K. Thornbury, "Origin of spontaneous rhythmicity in smooth muscle," *J. Physiol.*, vol. 570.1, pp. 23–28, 2006.

[17] K. D. McCloskey, "Interstitial cells in the urinary bladder—localization and function," *Neurourology and Urodynamics*, vol. 29, no. 1, pp. 82–87, 2010.

[18] T. V. Burdyga and S. Wray, "The relationship between the action potential, intracellular calcium and force in intact phasic, guinea-pig uretic smooth muscle," *The Journal of Physiology*, vol. 520, no. 3, pp. 867–883, 1999.

[19] H. C. Parkington, M. A. Tonta, N. K. Davies, S. P. Brennecke, and H. A. Coleman, "Hyperpolarization and slowing of the rate of contraction in human uterus in pregnancy by prostaglandins e_2 and $f_{2\alpha}$: involvement of the Na^+ pump," *The Journal of Physiology*, vol. 514, no. 1, pp. 229–243, 1999.

[20] B. Bengtsson, E. M. Chow, and J. M. Marshall, "Activity of circular muscle of rat uterus at different times in pregnancy," *American Journal of Physiology - Cell Physiology*, vol. 246, no. 3, pp. C216–C223, 1984.

[21] I. A. Csapo and H. A. Kuriyama, "Effects of ions and drugs on cell membrane activity and tension in the postpartum rat myometrium," *J. Physiol.*, vol. 165, pp. 575–592, 1963.

[22] J. F. Landa, T. C. West, and J. Thiersch, "Relationships between contraction and membrane electrical activity in the isolated uterus of the pregnant rat," *Am. J. Physiol.*, vol. 196, pp. 905–09, 1959.

[23] R. E. Garfield and W. L. Maner, "Physiology and electrical activity of uterine contractions," *Seminars in Cell & Developmental Biology*, vol. 18, no. 3, pp. 289 – 295, 2007.

[24] J. A. Martin, S. Kirmeyer, M. Osterman, and R. A. Shepherd, "Born a bit too early: Recent trends in late preterm births," *Natl Vital Stat Rep*, vol. 24, November 2009.

[25] M. F. MacDorman, W. M. Callaghan, T. J. Mathews, D. L. Hoyert, and K. D. Kochanek, "Trends in preterm-related infant mortality by race and ethnicity, united states, 1999-2004," *International Journal of Health Services*, vol. 37, no. 4, pp. 635–641, 2007.

[26] http://www.cdc.gov/reproductivehealth/maternalinfanthealth/PretermBirth.htm, June 2012.

[27] R. Duquette, A. Shmygol, C. Vaillant, A. Mobasheri, M. Pope, T. Burdyga, and S. Wray2, "Vimentin-positive, c-kit-negative interstitial cells in human and rat uterus: A role in pacemaking?," *Biology of Reproduction*, vol. 72, pp. 276–283, 2005.

[28] S. Wray, S. Kupittayanant, A. Shmygol, R. D. Smith, and T. Burdyga, "The physiological basis of uterine contractility: A short review," *Experimental Physiology*, vol. 86, no. 2, pp. 239–246, 2001.

[29] G. P. Sergeant, M. A. Hollywood, K. D. McCloskey, K. D. Thornbury, and N. G. McHale, "Specialised pacemaking cells in the rabbit urethra," *The Journal of Physiology*, vol. 526, no. 2, pp. 359–366, 2000.

[30] L. M. Popescu, S. M. Ciontea, and D. Cretoiu, "Interstitial cajal-like cells in human uterus and fallopian tube," *Annals of the New York Academy of Sciences*, vol. 1101, no. 1, pp. 139–165, 2007.

[31] R. C. Young, "Myocytes, myometrium, and uterine contractions," *Annals of the New York Academy of Sciences*, vol. 1101, no. 1, pp. 72–84, 2007.

[32] R. C. Young, "A computer model of uterine contractions based on action potential propagation and intercellular calcium waves," *Obstetrics & Gynecology*, vol. 89, no. 4, pp. 604 – 608, 1997.

[33] M. Yoshino, S. Wang, and C. Kao, "Sodium and calcium inward currents in freshly dissociated smooth myocytes of rat uterus," *The Journal of General Physiology*, vol. 110, no. 5, pp. 565–577, 1997.

[34] S. Wang, M. Yoshino, J. Sui, M. Wakui, P. Kao, and C. Kao, "Potassium currents in freshly dissociated uterine myocytes from nonpregnant and late-pregnant rats," *J. Gen.Physiol*, vol. 112, pp. 737–776, 1998.

[35] H. C. Parkington, M. A. Tonta, S. P. Brennecke, and H. A. Coleman, "Contractile activity, membrane potential, and cytoplasmic calcium in human uterine

smooth muscle in the third trimester of pregnancy and during labor," *American Journal of Obstetrics and Gynecology*, vol. 181, no. 6, pp. 1445 – 1451, 1999.

[36] S. M. Miller, R. E. Garfield, and E. E. Daniel, "Improved propagation in myometrium associated with gap junctions during parturition," *American Journal of Physiology - Cell Physiology*, vol. 256, no. 1, pp. C130–C141, 1989.

[37] H. Miyoshi, M. Boyle, L. MacKay, and R. Garfield, "Voltage-clamp studies of gap junctions between uterine muscle cells during term and preterm labor," *Biophysical Journal*, vol. 71, no. 3, pp. 1324 – 1334, 1996.

[38] G. Tortora and B. Derrickson, *Principles of Anatomy and Physiology 13th Edition Volume 2 for Southern Illinois University - Edwardsville*. No. v. 2, John Wiley & Sons, 2011.

[39] M. J. Taggart, A. Blanks, S. Kharche, A. Holden, B. Wang, and H. Zhang3, "Towards understanding the myometrial physiome: approaches for the construction of a virtual physiological uterus," *BMC Pregnancy and Childbirth*, vol. 7, p. S3, 2007.

[40] N. WIENER and A. ROSENBLUETH, "The mathematical formulation of the problem of conduction of impulses in a network of connected excitable elements, specifically in cardiac muscle.," *Archivos del Instituto de Cardiologia de Mexico*, vol. 16, pp. 205 – 265, 1946.

[41] H. F. Andersen and M. L. Barclay, "A computer model of uterine contractions based on discrete contractile elements," *Obstetrics & Gynecology*, vol. 86, pp. 108–111, Jul 1996.

[42] A. V. Shmigol, D. A. Eisner, and S. Wray, "Properties of voltage-activated $[Ca^{2+}]_i$ transients in single smooth muscle cells isolated from pregnant rat uterus," *Journal of Physiology*, vol. 511, no. 3, pp. 803–811, 1998.

[43] S. Rihana, J. Terrien, G. Germain, and C. Marque, "Mathematical modeling of electrical activity of uterine muscle cells," *Medical and Biological Engineering and Computing*, vol. 47, no. 6, pp. 665–675, 2009.

[44] W.-C. Tong, C. Y. Choi, S. Karche, A. V. Holden, H. Zhang, and M. J. Taggart, "A computational model of the ionic currents, Ca^{2+} dynamics and action potentials underlying contraction of isolated uterine smooth muscle," *PLoS ONE*, vol. 6, p. e18685, 04 2011.

[45] R. R. Garfield, K. Chwalisz, L. Shi, G. Olson, and G. R. Saade, "Instrumentation for the diagnosis of term and preterm labour: review," *Journal of Perinatal Medicine*, vol. 26, pp. 413–436, 1998.

[46] H. Eswaran, H. Preissl, J. D. Wilson, P. Murphy, and C. L. Lowery, "Prediction of labor in term and preterm pregnancies using non-invasive magnetomyographic recordings of uterine contractions," *American Journal of Obstetrics and Gynecology*, vol. 190, no. 6, pp. 1598 – 1602, 2004.

[47] L. Bursztyn, O. Eutan, A. J. Jaffa, and D. Elad, "Modeling myometrial smooth muscle contraction," *Annals of the New York Academy of Sciences*, vol. 1101, no. 1, pp. 110–138, 2007.

[48] T. Chard and G. Grudzinshas, *The Uterus*. Cambridge Reviews in Human Reproduction, Cambridge University Press, 1994.

[49] R. C. Young and R. O. Hession, "Three-dimensional structure of the smooth muscle in the term-pregnant human uterus," *Obstetrics & Gynecology*, vol. 93, 1999.

[50] B. Döring, O. Shynlova, P. Tsui, D. Eckardt, U. Janssen-Bienhold, F. Hofmann, S. Feil, R. Feil, S. J. Lye, and K. Willecke, "Ablation of connexin43 in uterine smooth muscle cells of the mouse causes delayed parturition," *Journal of Cell Science*, vol. 119, no. 9, pp. 1715–1722, 2006.

[51] M.-L. Tsai, K. Cesen-Cummings, R. C. Webb, and R. Loch-Caruso, "Acute inhibition of spontaneous uterine contractions by an estrogenic polychlorinated biphenyl is associated with disruption of gap junctional communication„" *Toxicology and Applied Pharmacology*, vol. 152, no. 1, pp. 18 – 29, 1998.

[52] C.-T. Wang and R. Loch-Caruso, "Phospholipase-mediated inhibition of spontaneous oscillatory uterine contractions by lindane in vitro„" *Toxicology and Applied Pharmacology*, vol. 182, no. 2, pp. 136 – 147, 2002.

[53] R. Loch-Caruso, K. Criswell, C. Grindatti, and K. Brant, "Sustained inhibition of rat myometrial gap junctions and contractions by lindane," *Reproductive Biology and Endocrinology*, vol. 1, no. 1, p. 62, 2003.

[54] V. Jacquemet, "Pacemaker activity resulting from the coupling with nonexcitable cells," *Phys. Rev. E*, vol. 74, p. 011908, Jul 2006.

[55] A. Kryukov, V. S. Petrov, L. S. Averyanova, G. V. Osipov, W. Chen, O. Drugova, and C. K. Chan, "Synchronization phenomena in mixed media of passive, excitable, and oscillatory cells," *Chaos*, vol. 18, no. 3, pp. 037129–1–16, 2008.

[56] P. Kohl, P. Camelliti, F. L. Burton, and G. L. Smith, "Electrical coupling of fibroblasts and myocytes: relevance for cardiac propagation," *Journal of Electrocardiology*, vol. 38, no. 4, Supplement, pp. 45 – 50, 2005.

[57] R. A. Gray, A. M. Pertsov, and J. Jalife, "Spatial and temploral organization during cardiac firbrillatation," *Nature*, vol. 392, pp. 75–78, March 1998.

[58] F. X. Witkowski, L. J. Leon, P. A. Penkoske, W. R. Giles, M. L. Spano, W. L. Ditto, and A. T. Winfree, "Spatiotemporal evolution of ventricular fibrillation spatiotemporal evolution of ventricular fibrillation spatiotemporal evolution of ventricular fibrillation," *Nature*, vol. 392, pp. 78–82, March 1998.

[59] H. Fukuda, N. Nakamichi, M. Hisatsune, H. Murase, and T. Mizuno, "Synchronization of plant circadian oscillators with a phase delay effect of the vein network," *Phys. Rev. Lett.*, vol. 99, p. 098102, Aug 2007.

[60] I. Z. kiss, Y. Zhai, and J. L. Hudson, "Emerging coherence in a population of chemical oscillators," *Science*, vol. 296, pp. 1676–1678, May 2002.

[61] J. F. Hipp, A. K. Engel, and M. Siegel, "Oscillatory synchronization in large-scale cortical networks predicts perception," *Neuron*, vol. 69, pp. 387–396, January 2011.

[62] V. N. Belykh, G. V. Osipov, V. S. Petrov, J. A. K. Suykens, and J. Vandewalle, "Cluster synchronization in oscillatory networks," *Chaos*, vol. 18, p. 037106, September 2008.

[63] A. Neiman, L. Schimansky-Geier, A. Cornell-Bell, and F. Moss, "Noise-enhanced phase synchronization in excitable media," *Phys. Rev. Lett.*, vol. 83, pp. 4896–4899, Dec 1999.

[64] E. Avalos, P.-Y. Lai, and C. K. Chan, "Spiral waves in the heterogeneous excitable kuramoto model," *EPL (Europhysics Letters)*, vol. 94, no. 6, p. 60006, 2011.

[65] G. Bub, A. Shrier, and L. Glass, "Spiral wave generation in heterogeneous excitable media," *Phys. Rev. Lett.*, vol. 88, p. 058101, Jan 2002.

[66] G. Bub, A. Shrier, and L. Glass, "Global organization of dynamics in oscillatory heterogeneous excitable media," *Phys. Rev. Lett.*, vol. 94, p. 028105, Jan 2005.

[67] O. I. Kanakov and G. V. Osipov, "Cluster synchronization and spatio-temporal dynamics in networks of oscillatory and excitable luo-rudy cells," *Chaos*, vol. 17, p. 015111, 2007.

[68] W. Chen, S. Cheng, E. Avalos, O. Drugova, G. Osipov, P.-Y. Lai, and C. K. Chan, "Synchronisation in growing heterogeneous media," *EPL*, vol. 86, p. 18001, 2009.

[69] C. Ramon, H. Preissl, P. Murphy, J. D. Wilson, C. Lowery, and H. Eswaran, "Synchronization analysis of the uterine magnetic activity during contractions," *BioMdedical Engineering Online*, vol. 4, p. 55, 2005.

[70] A. L. Hodgkin, A. F. Huxley, and B. Katz, "Measurement of current-voltage relations in the membrane of the giant axon of loligo," *Journal of Physiology*, vol. 116, pp. 424–448, 1952.

[71] A. L. Hodgkin and A. F. Huxley, "Currents carried by sodium and potassium ions through the membrane of the giant axon of loligo," *Journal of Physiology*, vol. 116, pp. 449–472, 1952.

[72] A. L. Hodgkin and A. F. Huxley, "The components of membrane conductance in the giant axon of loligo," *Journal of Physiology*, vol. 116, pp. 472–496, 1952.

[73] H. AL and H. AF, "A quantitative description of membrane current and its application to conduction and excitation in nerve," *Journal Physiol*, vol. 117, no. 4, pp. 500–544, 1952.

[74] M. Nelson and J. Rinzel, "Interactions between membrane potential and intracellular calcium concentration in vascular smooth muscle," *Acta Physiologica Scandinavica*, vol. 164, pp. 559–566, December 1998.

[75] D. Junge, *Nerve and muscle excitation*. No. Third Editon in ISBN 0-87893-406-5, SINAUER Associates, Inc., 1992.

[76] A. Pumir, V. Nikolski, M. Hörning, A. Isomura, K. Agladze, K. Yoshikawa, R. Gilmour, E. Bodenschatz, and V. Krinsky, "Wave emission from heterogeneities opens a way to controlling chaos in the heart," *Phys. Rev. Lett.*, vol. 99, p. 208101, Nov 2007.

[77] T. Chay and J. Keizer, "Minimal model for membrane oscillations in the pancreatic beta-cell," *Biophysical Journal*, vol. 42, no. 2, pp. 181 – 189, 1983.

[78] L. Bursztyn, O. Eytan, A. J. Jaffa, and D. Elad, "Mathematical model of excitation-contraction in a uterine smooth muscle cell," *American Journal of Physiology - Cell Physiology*, vol. 292, no. 5, pp. C1816–C1829, 2007.

[79] S. Wray, T. Burdyga, and K. Noble, "Calcium signalling in smooth muscle," *Cell Calcium*, vol. 38, pp. 397 – 407, 2005.

[80] R. Young, L. Smith, and M. McLaren, "T-type and l-type calcium currents in freshly dispersed human uterine smooth muscle cells," *Am. J. Obstet. Gynecol.*, vol. 169, no. 4, pp. 785–792, 1993.

[81] M. H, U. T, and Fujiwara, "Electrophysiological properties of membrane currents in single myometrial cells isolated from pregnant rats," *Pflugers Arch.*, vol. 419, no. 386-393, 1991.

[82] R. Floyd and S. Wray, "Calcium transporters and signalling in smooth muscles," *Cell Calcium*, vol. 42, pp. 467 – 476, 2007.

[83] A. Goldbeter, *Biochemical oscillations and cellular rhythms*. ISBN:9780521599467, Cambridge University Press, 1996.

[84] G. Dupont1 and H. Croisier1, "Spatiotemporal organization of Ca^{2+} dynamics: A modeling based approach," *HFSP Journal*, vol. 4, pp. 42–511, 2010.

[85] A. Shmygol and S. Wray, "Functional architecture of the sr calcium store in uterine smooth muscle," *Cell Calcium*, vol. 35, no. 6, pp. 501 – 508, 2004.

[86] C. R. Weber, K. S. Ginsburg, K. D. Philipson, T. R. Shannon, and D. M. Bers, "Allosteric regulation of Na^+/Ca^{2+} exchange current by cytosolic ca in intact cardiac myocytes," *The Journal of General Physiology*, vol. 117, no. 2, pp. 119–132, 2001.

[87] J. Keener and J.Sneyd, *Mathematical Physiology*. ISBN 0-387-98381-3, Springer-Verlag, second edition ed., 1998.

[88] G. A. Knock, S. V. Smirnov, and P. I. Aaronson, "Voltage-gated k+ currents in freshly isolated myocytes of the pregnant human myometrium," *The Journal of Physiology*, vol. 518, no. 3, pp. 769–781, 1999.

[89] A. T. Stamp, G. V. Osipov, and J. J. Collins1, "Suppressing arrhythmias in cardiac models using overdrive pacing and calcium channel blockers," *Chaos*, vol. 12, pp. 931–940, 2002.

[90] O. McManus, "Calcium-activated potassium channels: Regulation by calcium," *Journal of Bioenergetics and Biomembranes*, vol. 23, pp. 537–560, 1991.

[91] I. Langmuir, "The adsorption of gases on plane surfaces of glass, mica, and platinum," *J. Am. Chem. Soc*, vol. 40, pp. 1361–1403, 1918.

[92] R. N. Khan, B. Matharoo-Ball, S. Arulkumaran, and M. L. J. Ashford, "Potassium channels in the human myometrium," *Experimental Physiology*, vol. 86, no. 2, pp. 255–264, 2001.

[93] C. Vergara, R. Latorre, N. V. Marrion, and J. P. Adelman, "Calcium-activated potassium channels," *Current Opinion in Neurobiology*, vol. 8, no. 3, pp. 321 – 329, 1998.

[94] K. Jones, A. Shmygol, S. Kupittayanant, and S. Wray, "Electrophysiological characterization and functional importance of calcium-activated chloride channel in rat uterine myocytes," *Pflügers Archiv European Journal of Physiology*, vol. 448, pp. 36–43, 2004.

[95] Y. Nakamura, Y. Ohya, I. Abe, and M. Fujishima, "Sodium-potassium pump current in smooth muscle cells from mesenteric resistance arteries of the guinea-pig," *The Journal of Physiology*, vol. 519, no. 1, pp. 203–212, 1999.

[96] H. Satoh, "Identification of a hyperpolarization-activated inward current in uterine smooth muscle cells during pregnancy," *General Pharmacology: The Vascular System*, vol. 26, no. 6, pp. 1335 – 1338, 1995.

[97] H. Miyoshi, K. Yamaoka, R. R. Garfield, and K. Ohama, "Identification of a non-selective catio channel current in myometrail cells isolated from pregnant rats," *European Journal of Physiology*, vol. 447, pp. 457–464, 2004.

[98] A. Turi, Z. Marcsek, N. Mullner, M. Kucsera, and Z. Bori, "The activity of Na^+/K^+–ATPase and abundance of its mrna are regulated in rat myometrium during pregnancy," *Biochemical and biophysical research communications*, vol. 188, no. 3, pp. 1191–1197, 1992.

[99] A. Yatani, K. Okabe, J. Codina, L. Birnbaumer, and A. Brown, "Heart rate regulation by g proteins acting on the cardiac pacemaker channel," *Science*, vol. 249, pp. 1163–1166, 1990.

[100] K. O. amd Y. Inoue, T. Kawarabayashi, and H. Kajiya, "Physiological significance of hyperpolarization-activated inward currents (i_h) in smooth muscle cells from the circular layers of pregnant rat myometrium," *Pflügers Archiv European Journal of Physiology*, vol. 439, pp. 76–85, 1999.

[101] A. M. Blanks, Z.-H. Zhao, A. Shmygol, G. Bru-Mercier, S. Astle, and S. Thornton, "Characterization of the molecular and electrophysiological properties of the t-type calcium channel in human myometrium," *The Journal of Physiology*, vol. 581, no. 3, pp. 915–926, 2007.

[102] S.-E. Lee, D.-S. Ahn, and Y.-H. Lee, "Role of T-type Ca^{2+} channels in the spontaneous phasic contraction of pregnant rat uterine smooth muscle," *Korean J Physiol Pharmacol*, vol. 13, pp. 241–249, Jun 2009.

[103] H. A. Coleman and H. C. Parkington, "Single channel cl^- and k^+ currents from cells of uterus not treated with enzymes," *Pflügers Archiv European Journal of Physiology*, vol. 410, pp. 560–562, 1987.

[104] J. Mironneau, S. Arnaudeau, N. Macrez-Lepretre, and F. Boittin, "Ca^{2+} sparks and Ca^{2+} waves activate different Ca^{2+}-dependent ion channels in single myocytes from rat portal vein," *Cell Calcium*, vol. 20, no. 2, pp. 153 – 160, 1996.

[105] M. Nakao and D. C. Gadsby, "Na and k depenence of the [na/k] pump current-voltage relationship in guinea pig ventricular myocytes," *J. Gen.Physiol*, vol. 94, pp. 539–565, 1989.

[106] S. Wray, K. Jones, S. Kupittayanant, Y. Li, A. Matthew, E. Monir-Bishty, K. Noble, S. J. Pierce, S. Quenby, and A. V. Shmigol, "Calcium signaling and uterine contractility," *J Soc Gynecol Investig*, vol. 10, no. 5, pp. 252–264, 2003.

[107] J. Lytton, M. Westlin, and M. R. Ranley, "Thapsigargin inhibits the sarcoplasmic or endoplasmic reticulum ca-atpase family of calcium pumps," *The Journal of Biological Chemistry*, vol. 266, no. 26, pp. 17067–17071, 1991.

[108] A. Shmygol, D. A. Eisner, and S. Wray, "Carboxyeosin decreases the rate of decay of the $[Ca^{2+}]_i$ transient in uterine smooth muscle cells isolated from pregnant rats," *Pflügers Archiv European Journal of Physiology*, vol. 437, pp. 158–160, 1998.

[109] K. Noble, A. Matthew, T. Burdyga, and S. Wray, "A review of recent insights into the role of the sarcoplasmic reticulum and ca entry in uterine smooth muscle," *European Journal of Obstetrics & Gynecology and Reproductive Biology*, vol. 144, Supplement 1, no. 0, pp. S11 – S19, 2009.

[110] J. Guckenheimer and P. Holmes, *Nonlinear oscillations, dynamical systems, and bifurcations of vector fields*, vol. 42 of *ISBN 0-3879-0819-6*. New York: Springer-Verlag, 1983.

[111] D. Aur, C. I. Connolly, and M. S. Jog, "Computing spike directivity with tetrodes," *Journal of Neuroscience Methods*, vol. 149, no. 1, pp. 57 – 63, 2005.

[112] T. Sasaki, N. Matsuki, and Y. Ikegaya, "Action-potential modulation during axonal conduction," *Science*, vol. 331, no. 6017, pp. 599–601, 2011.

[113] J. L. Hindmarsh and R. M. Rose, "A model of neuronal bursting using three coupled first order differential equations," *Proceedings of the Royal Society of London. Series B. Biological Sciences*, vol. 221, no. 1222, pp. 87–102, 1984.

[114] P. Gray and S. K. Scott, *Chemical Oscillations and Instabilities: Nonlinear Chemical Kinetics*. New York: Oxford University Press, 1990.

[115] M. G. E. Glatt and F. Kaiser, "Noise-assisted spike propagation in myelinated neurons," *Physical Review E*, vol. 79, no. 1, p. 011904, 2009.

[116] D. Roy, A. Ghosh, and V. K. Jirsa, "Phase description of spiking neuron networks with global electric and synaptic coupling," *Phys. Rev. E*, vol. 83, p. 051909, May 2011.

[117] Y. Gong and D. J. Christini, "Antispiral waves in reaction-diffusion systems," *Phys. Rev. Lett.*, vol. 90, p. 088302, Feb 2003.

[118] J. Rinzel, "Excitation dynamics: insights from simplified membrane models," *Federation Proceedings*, vol. 15, no. 44, pp. 2944–2946, 1985.

[119] T. Kostova, R. Ravindran, and M. Schonbek, "Fitzhugh-nagumo revisited: Types of bifurcations, periodical forcing and stability regions by lyapunov funtional," *International Journal of Bifurcation and Chaos*, vol. 14, no. 3, pp. 913–925, 2003.

[120] M. Ringkvist and Y. Zhou, "On the dynamical behaviour of fitzhugh—nagumo systems: Revisited," *Nonlinear Analysis: Theory, Methods & Applications*, vol. 71, pp. 2667 – 2687, 2009.

[121] P. Kohl, A. G. Kamkin, I. S. Kiseleva, and D. Noble, "Mechanosensitive fibroblasts in the sino-atrial node region of rat heart:interaction with cardiomyocytes and possible role," *Experimental Phyisology*, vol. 79, pp. 943–956, 1994.

[122] M. Takemura, H. Itoh, N. Sagawa, *et al.*, "Cyclic mechanical stretch augments hyaluronan production in cultured human uterine cervical fibroblast cells," *Molecular Human Reproduction*, vol. 11, pp. 659–665, September 2005.

[123] E. Malmstrom, M. Sennstrom, A. Holmberg, *et al.*, "The importance of fibroblasts in remodelling of the human uterine cervix during pregnancy and parturition," *Molecular Human Reproduction*, vol. 13, pp. 333–441, March 2007.

[124] Y. Shibukawa, E. L. Chilton, K. A. MacCannell, R. B. Clark, and W. R. Giles, "K^+ currents activated by depolarization in cardiac fibroblasts," *Biophysical Journal*, vol. 88, no. 6, pp. 3924 – 3935, 2005.

[125] K. A. MacCannell, H. Bazzazi, L. Chilton, Y. Shibukawa, R. B. Clark, and W. R. Giles, "A mathematical model of electrotonic interactions between ventricular myocytes and fibroblasts," *Biophysical Journal*, vol. 92, no. 11, pp. 4121 – 4132, 2007.

[126] I. Kiseleva, A. Kamkin, A. Pylaev, D. Kondratjev, K. Leiterer, H. Theres, K. Wagner, P. Persson, and J. Gunther, "Electrophysiological properties of mechanosensitive atrial fibroblasts from chronic infarcted rat heart," *Journal of Molecular and Cellular Cardiology*, vol. 30, no. 6, pp. 1083 – 1093, 1998.

[127] V. Jacquemet and C. S. Henriquez, "Modelling cardiac fibroblasts: interactions with myocytes and their impact on impulse propagation," *Europace*, vol. 9, no. suppl 6, pp. vi29–vi37, 2007.

[128] S. Zlochiver, V. Munoz, K. Vikstrom, S. Taffet, O. Bernenfeld, and J. Jalife, "Electronic myofibroblast-to-myocyte coupling increases propensity to reentrant arrhythmias in two-dimensional cardiac monolayers," *Biolphys .J*, vol. 95, pp. 4469–4480, 2008.

[129] L. Chilton, W. R. Giles, and G. L. Smith, "Evidence of intercellular coupling between co-cultured adult rabbit ventricular myocytes and myofibroblasts," *The Journal of Physiology*, vol. 583, no. 1, pp. 225–236, 2007.

[130] V. Valiunas, S. Doronin, L. Valiuniene, I. Potapova, J. Zuckerman, B. Walcott, R. B. Robinson, M. R. Rosen, P. R. Brink, and I. S. Cohen, "Human mesenchymal stem cells make cardiac connexins and form functional gap junctions," *The Journal of Physiology*, vol. 555, no. 3, pp. 617–626, 2004.

[131] Y. Kurata, I. Hisatome, H. Matsuda, and T. Shibamoto, "Dynamical mechanisms of pacemaker generation in ik1-downregulated human ventricular myocytes: Insights from bifurcation analyses of a mathematical model," *Biophysical Journal*, vol. 89, no. 4, pp. 2865 – 2887, 2005.

[132] A. Pumir, A. Arutunyan, V. Krinsky, and N. Sarvazyan, "Genesis of ectopic waves: Role of coupling, automaticity, and heterogeneity," *Biophysical Journal*, vol. 89, no. 4, pp. 2332 – 2349, 2005.

[133] V. Petrov, G. V. Osipov, and J. Kurths, "Fibroblasts alter spiral wave stability," *Chaos*, vol. 20, p. 045103, 2010.

[134] R. Garfield, G. Saade, C. Buhimschi, I. Buhimschi, L. Shi, S. Shi, and K. Chwalisz, "Control and assessment of the uterus and cervix during pregnancy and labour," *Human Reproduction Update*, vol. 4, no. 5, pp. 673–695, 1998.

[135] S. Blackburn, *Maternal, Fetal & Neonatal Physiology:A Clinical Perspective*. Saunders-Elsevier, 2007.

[136] D. K. Welsh, J. S. Takahashi, and S. A. Kay, "Suprachiasmatic nucleus: cell autonomy and network properties," *Annual Review of Physiology*, vol. 72, pp. 551–577, March 2010.

[137] W.-Y. Chiang, P.-Y. Lai, and C. K. Chan, "Frequency enhancement in coupled noisy excitable elements," *Phys. Rev. Lett.*, vol. 106, p. 254102, Jun 2011.

[138] W. J. Lammers and R. Hamid, "The initiation, continuation, and termination of spontaneous episodes of circus movements in the pregnant myometrium of the rat," *American Journal of Obstetrics and Gynecology*, vol. 179, no. 6, Part 1, pp. 1515 – 1526, 1998.

[139] W. J. E. P. Lammers, B. Stephen, R. Hamid, and D. W. G. Harron, "The effects of oxytocin on the pattern of electrical propagation in the isolated pregnant uterus of the rat," *Pflügers Archiv European Journal of Physiology*, vol. 437, pp. 363–370, 1999.

[140] R. Singh, J. Xu, N. Garnier, A. Pumir, and S. Sinha, "Self-organized transition to coherent activity in disordered media," *Phys. Rev. Lett.*, vol. 108, p. 068102, Feb 2012.

[141] J. E. P. Lammer and R. Hamid, "The initiation, continuation, and termination of spontaneous episodes of circus movements in the pregnant myometrium of the rat," *Am. J. Obstet. Gynecol.*, vol. 179, pp. 1515–1526, 1998.

[142] W. J. Lammers, H. Mirghani, B. Stephen, S. Dhanasekaran, A. Wahab, M. A. Al Sultan, and F. Abazer, "Patterns of electrical propagation in the intact

pregnant guinea pig uterus," *American Journal of Physiology - Regulatory, Integrative and Comparative Physiology*, vol. 294, no. 3, pp. R919–R928, March 2008.

[143] R. J. Larsen and M. L. Marx, *Introduction to Mathematical Statistics and Its Applications*. ISBN-13: 9780131867932, Pearson, 4/e ed., 2005.

[144] V. S. Petrov, G. V. Osipov, and J. A. K. Suykens, "Influence of passive elements on the dynamics of oscillatory ensembles of cardiac cells," *Phys. Rev. E*, vol. 79, p. 046219, Apr 2009.

[145] D. Engin, S. Orlov, M. Segev, G. C. Valley, and A. Yariv, "Order-disorder phase transition and critical slowing down in photorefractive self-oscillators," *Phys. Rev. Lett.*, vol. 74, pp. 1743–1746, Mar 1995.

[146] D. Alloyeau, C. Ricolleau, C. Mottet, T. Oikawa, C. Langlois, Y. L. Bouar, and N. Braidy, "Size and shape effects on the order–disorder phase transition in copt nanoparticles," *nature materials*, vol. 8, pp. 940–946, December 2009.

[147] M. Mezard, G. Parisi, and M. Virasoro, *Spin Glass Theory And Beyond*, vol. 9 of *978-9971-5-0115-0*. Singapore: World Scientific, 1986.

[148] H. Cramér, *Mathematical Methods of Statistics*. Princeton University Press, 1957.

[149] R. Beals and R. Wong, *Special Functions*. ISBN:9780521197977, Cambridge University Press, 2001.

[150] R. L. Shew, J. A. Yee, D. B. Kliewer, Y. J. Keflemariam, and D. L. McNeill, "Parathyroid hormone-related protein inhibits stimulated uterine contraction in vitro," *Journal of Bone and Mineral Research*, vol. 6, no. 9, pp. 955–959, 1991.

[151] C. M. Hai and R. A. Murphy, "Cross-bridge phosphorylation and regulation of latch state in smooth muscle," *American Journal of Physiology - Cell Physiology*, vol. 254, no. 1, pp. C99–C106, 1988.

Appendices

Appendix A

Modified Rihana's model

Variables

C($\mu F/cm^2$)	capacitance of the cell membrane
t(ms)	time
τ_i(ms)	time constants of activation and inactivation,i = Na,Ca,K
s(μm^2)	area of cell membrane surface
$[Ca^{2+}]_{i,o}(mM)$	intra and extra cellular calcium concentration
$G_i(mS/cm^2)$	Largest conductance of channel i, i = Na,Ca,K_1, K_2 and K_3
k_i	slope factor of half activation and inactivation of channel i, i = Na,Ca,K_1, K_2 and K_3 V_m (mV) membrane potential
E_i(mV)	reversal potential of each channel,i =Na, Ca, K,Leakage
V_{mi}, V_{hi}(mV)	half activating and inactivating potential, i= Na,Ca,K
I_{st} ($\mu A/cm^2$)	externally applied stimulus current
I_{Na}($\mu A/cm^2$)	Na current
I_K ($\mu A/cm^2$)	K current
I_{Ca}($\mu A/cm^2$)	Ca current
I_L ($\mu A/cm^2$)	Leakage current
I_{KCa}($\mu A/cm^2$)	calcium activated potassium current
m_{Na},h_{Na},	Na activating and inactivating variables
$m_{Na\infty}$,$h_{Na\infty}$	Na activating and inactivating steady states
m_{Ca},h_{Ca_i},	Ca activating and inactivating variables, $i = s, f$; s, slow inactivating component, f, fast inactivating component
$m_{Ca\infty}$,$h_{Ca\infty}$	Ca activating and inactivating steady states
n_{K_i},h_{K_i},	K activating and inactivating variables,i = 1,2 and 3.
$n_{K\infty_i}$,$h_{K\infty_i}$	K activating and inactivating steady states,i = 1,2 and 3.

Equations used in the model

Main equation

$$\begin{aligned} I_{cell} = &-C\frac{dV_m}{dt} - g_{\mathrm{Ca}}(V_m - E_{\mathrm{Ca}}) - g_{\mathrm{Na}}(V_m - E_{\mathrm{Na}}) \\ &- g_{\mathrm{K}}(V_m - E_{\mathrm{K}}) - g_{\mathrm{K(Ca)}}(V_m - E_{\mathrm{K}}) - g_L(V_m - E_L) \end{aligned} \tag{A.1}$$

$$C\frac{dV_m}{dt} = I_{st} - (I_{\mathrm{Na}} + I_{\mathrm{Ca}} + I_{\mathrm{K}} + I_L) \tag{A.2}$$

Sodium channel

$$I_{\mathrm{Na}} = G_{\mathrm{Na}} h_{\mathrm{Na}} m_{\mathrm{Na}}^4 (V_m - E_{\mathrm{Na}}), \qquad G_{\mathrm{Na}} = 0.31\mathrm{mS/cm}^2, E_{\mathrm{Na}} = 83\mathrm{mV} \tag{A.3}$$

$$\frac{dm_{\mathrm{Na}}}{dt} = \frac{m_{\mathrm{Na}\infty}(V_m) - m_{\mathrm{Na}}}{\tau_{m\mathrm{Na}}(V_m)} \tag{A.4a}$$

$$\frac{dh_{\mathrm{Na}}}{dt} = \frac{h_{\mathrm{Na}\infty}(V_m) - h_{\mathrm{Na}}}{\tau_{h\mathrm{Na}}(V_m)} \tag{A.4b}$$

$$\tau_{\mathrm{Na}m} = 0.2598e^{-0.021V_m} \tag{A.5a}$$

$$\tau_{\mathrm{Na}h} = 0.5034e^{-0.033V_m} + 0.09e^{0.03V_m} \tag{A.5b}$$

$$m_{\mathrm{Na}\infty} = \frac{1}{1 + \exp\frac{V_m - V_{h_{\mathrm{Na}_m}}}{k_{\mathrm{Na}_m}}}, \qquad V_{h_{\mathrm{Na}_m}} = -21, k_{\mathrm{Na}_m} = -5 \tag{A.6}$$

$$h_{\mathrm{Na}\infty} = \frac{1}{1 + \exp\frac{V_m - V_{h_{\mathrm{Na}_h}}}{k_{\mathrm{Na}_h}}}, \qquad V_{h_{\mathrm{Na}_h}} = -58.9mV, k_{\mathrm{Na}_h} = 8.7 \tag{A.7}$$

Calcium channel

$$\begin{aligned} I_{\mathrm{Ca}} &= G_{\mathrm{Ca}} m_{\mathrm{Ca}}^2 h_{\mathrm{Ca}} (V_m - E_{\mathrm{Ca}}) \\ E_{\mathrm{Ca}} &= \frac{RT}{zF} \ln \frac{[\mathrm{Ca}^{2+}]_o}{[\mathrm{Ca}^{2+}]_i}, \qquad [\mathrm{Ca}^{2+}]_o = 3.0\mathrm{mM} \\ G_{\mathrm{Ca}} &= 0.095\mathrm{mS/cm}^2 \end{aligned} \tag{A.8}$$

$$h_{\mathrm{Ca}} = 0.38h_{\mathrm{Cas}} + 0.22h_{\mathrm{Ca}f} + 0.06 \tag{A.9}$$

$$\frac{dm_{\mathrm{Ca}}}{dt} = \frac{m_{\mathrm{Ca}\infty}(V_m) - m_{\mathrm{Ca}}}{\tau_{m\mathrm{Ca}}(V_m)} \tag{A.10a}$$

$$\frac{dh_{\mathrm{Ca}f}}{dt} = \frac{h_{\mathrm{Ca}\infty}(V_m) - h_{\mathrm{Ca}f}}{\tau_{h\mathrm{Ca}f}(V_m)} \tag{A.10b}$$

$$\frac{dh_{\mathrm{Ca}s}}{dt} = \frac{h_{\mathrm{Ca}\infty}(V_m) - h_{\mathrm{Ca}s}}{\tau_{h\mathrm{Ca}s}(V_m)}, \qquad \tau_{h\mathrm{Ca}s} = 160\mathrm{ms} \tag{A.10c}$$

$$h_{\mathrm{Ca}} = 0.38h_{\mathrm{Ca}s} + 0.22h_{\mathrm{Ca}f} + 0.06 \tag{A.11}$$

$$\tau_{m\mathrm{Ca}} = 0.64e^{-0.04*Vm} + 1.188 \tag{A.12}$$

$$\tau_{\mathrm{Ca}f} = -0.00061V_m^3 + 0.074V_m^2 - 1.5V_m + 41 \tag{A.13}$$

$$m_{\mathrm{Ca}\infty} = \frac{1}{1 + \exp(\frac{V_m - V_{h_{\mathrm{Ca}m}}}{k_{\mathrm{Ca}m}})}, \qquad V_{h_{\mathrm{Ca}m}} = -25.4\mathrm{mV}, k_{\mathrm{Ca}h} = 7.6\mathrm{mV} \tag{A.14a}$$

$$h_{\mathrm{Ca}\infty} = \frac{1}{1 + \exp(\frac{V_m - V_{h_{\mathrm{Ca}h}}}{k_{\mathrm{Ca}h}})}, \qquad V_{h_{\mathrm{Ca}h}} = -34\mathrm{mV}, k_{\mathrm{Ca}h} = 5.4\mathrm{mV} \tag{A.14b}$$

[Ca]$_i^{2+}$ Dynamics

$$\begin{aligned} \frac{d[\mathrm{Ca}^{2+}]_i}{dt} =& f_c(-\alpha I_{\mathrm{Ca}} - k_{\mathrm{Ca}}[\mathrm{Ca}^{2+}]_i) \\ f_c =& 0.004 \\ \alpha =& 4 \times 10^{-5}\mathrm{mol} \cdot \mathrm{cm}^{-1}\mathrm{C}^{-1} \\ k_c =& 0.01\mathrm{ms} \end{aligned} \tag{A.15}$$

Potassium channel

$$\begin{aligned} I_{\mathrm{K}} &= (G_{\mathrm{K}_1} n_{\mathrm{K}_1} h_{\mathrm{K}_1} + G_{\mathrm{K}_2} n_{\mathrm{K}_2} + G_{\mathrm{K}_3} n_{\mathrm{K}_3\infty})(V_m - E_{\mathrm{K}}) \\ G_{\mathrm{K}_1} &= 0.254\mathrm{mS/cm}^2, G_{\mathrm{K}_2} = 0.064\mathrm{mS/cm}^2, G_{\mathrm{K}_3} = 0.033\mathrm{mS/cm}^2 \\ E_{\mathrm{K}} &= \text{-}70\mathrm{mV} \end{aligned} \tag{A.16}$$

$$\begin{aligned} \frac{dn_{\mathrm{K}_1}}{dt} &= \frac{n_{\mathrm{K}_1\infty} - n_{\mathrm{K}_1}}{\tau_{n_{\mathrm{K}_1}}} \\ \frac{dh_{\mathrm{K}_1}}{dt} &= \frac{h_{\mathrm{K}_1\infty} - h_{\mathrm{K}_1}}{\tau_{h_{\mathrm{K}_1}}} \\ \frac{dn_{\mathrm{K}_2}}{dt} &= \frac{n_{\mathrm{K}_2\infty} - n_{\mathrm{K}_2}}{\tau_{n_{\mathrm{K}_2}}} \end{aligned} \tag{A.17}$$

$$
\begin{aligned}
n_{\mathrm{K}_1\infty} &= \frac{1}{1+\exp(\frac{7.7-Vm}{23.7})} \\
h_{\mathrm{K}_1\infty} &= \frac{1}{1+\exp(\frac{-62.7-Vm}{-6.3})} \\
n_{\mathrm{K}_2\infty} &= \frac{1}{1+\exp(\frac{4.2-Vm}{22.1})} \\
n_{\mathrm{K}_3\infty} &= \frac{1}{1+\exp(\frac{63.4-Vm}{16.7})}
\end{aligned}
\tag{A.18}
$$

$$
\begin{aligned}
\tau_{n\mathrm{K}_1} &= 28.23\exp(-\frac{V_m}{-21.8}) \\
\tau_{n\mathrm{K}_2} &= 35.75\exp(-\frac{V_m}{-71.94}) \\
\tau_{h\mathrm{K}_1} &= 50
\end{aligned}
\tag{A.19}
$$

Leakage Current

$$
I_L = G_L(V_m - E_L), \qquad G_L = 0.0058\mathrm{mS/cm}^2, E_L = \text{-}40\mathrm{mV} \tag{A.20}
$$

Calcium potassium dependent current

$$
\begin{aligned}
I_{\mathrm{K(Ca)}} &= G_{\mathrm{KCa}}\frac{[\mathrm{Ca}_i^{2+}]^N}{K_{1/2}^N + [\mathrm{Ca}_i^{2+}]^N}(V_m - E_K) \\
G_{\mathrm{KCa}} &= 0.08\ \mathrm{mS/cm}^2, K_{1/2} = 0.015\mathrm{mM}, N = 2
\end{aligned}
\tag{A.21}
$$

Appendix B

Derivation of effective passive cell resting potential

Considering two different passive cells, the ICLCs and fibroblasts, are coupled to a myocyte cell, the equation governing the myocyte membrane potential dynamics is Equ.3.6a:

$$\begin{aligned} -C_m\frac{dV_m}{dt} =& I_{ion} + (n_F G_{gap}(V_m - V_F) + n_I G_{gap}(V_m - V_I)) \\ =& I_{ion} + (n_F + n_I)G_{gap}V_m - (n_F V_F + n_I V_I) \\ =& I_{ion} + n_p G_{gap}(V_m - (\frac{n_F}{n_p}V_F + \frac{n_I}{n_p}V_I)) \\ =& I_{ion} + n_p G_{gap}(V_m - V_p) \end{aligned} \tag{B.1}$$

where n_F and n_I are the number of fibroblasts and ICLCs coupled to the myocyte, and $n_p = n_F + n_I$ counts the total number of passive passive cells. Taking into account the fibroblasts' small membrane capacitance and low resistance, its membrane potential quickly relaxes to steady state defined as Eq. (3.11). Substitute Eq.(3.11) into Eq.(3.13), we get

$$V_I = \frac{1}{n_I}(n_p V_p - n_F\frac{G_F V_F^r + G V_m}{G + G_F}) \tag{B.2}$$

Using $V_p = \frac{1}{n_p}(n_F V_F + n_I V_I)$, we have

$$\begin{aligned}
\frac{dV_p}{dt} =& \frac{n_I}{n_p}\frac{dV_I}{dt} + \frac{n_F}{n_p}\frac{dV_F}{dt} \\
=& -\frac{1}{C_I}(G_I(V_p - \frac{n_F}{n_P}\frac{G_F V_F^r + G V_m}{G+G_F} - \frac{n_I}{n_p}V_I^r) + G(V_p - \frac{n_F}{n_p}\frac{G_F V_F^r + G V_m}{G+G_F} - \frac{n_I}{n_p}V_m)) \\
=& -\frac{1}{C_I}(G_I(V_p - (\frac{n_F}{n_p}\frac{G_F V_F^r}{G+G_F} + \frac{n_I}{n_p}V_I^r)) - \frac{n_F}{n_p}\frac{G G_F V_m}{G+G_F} \\
&+ G(V_p - (\frac{n_F}{n_p}\frac{G V_m}{G+G_F} + \frac{n_I}{n_p}V_m)) - \frac{n_F}{n_p}\frac{G G_F V_F^r}{G+G_F}) \\
=& -\frac{1}{C_I}(G_I(V_p - (\frac{n_F}{n_p}(\frac{G V_m}{G+G_F} + \frac{G_F G V_m}{G(G+G_F)}) + \frac{n_I}{n_p}V_m)) \\
&+ G(V_p - (\frac{n_F}{n_p}(\frac{G V_m}{G+G_F} + \frac{G_I G V_m}{G(G+G_F)}) + \frac{n_I}{n_p}V_m))) \\
=& -\frac{1}{C_I}(G_I(V_p - \frac{1}{n_p}(n_F V_F^r + n_I V_I^r)) + G(V_p - V_m)) \\
=& -\frac{1}{C_I}(G_I(V_p - V_p^r) + G(V_p - V_m))
\end{aligned} \tag{B.3}$$

where the assumption that $\frac{dV_F}{dt} = 0$ and $G_I = G_F$ are used in the derivation. We see that by defining$V_p^r = \frac{1}{n_p}(n_F V_F^r + n_I V_I^r)$, the total effect of passive cells is returned to the normal form [121].